Near threshold femtosecond laser interactions with materials: Ablation thresholds, morphologies, and dynamics

by

Joel P. McDonald

A dissertation submitted in partial fulfillment
of the requirements for the degree of
Doctor of Philosophy
(Applied Physics)
in The University of Michigan
2007

Doctoral Committee

Associate Professor Steven M. Yalisove, Chair
Professor Theodore B. Norris
Professor Bradford G. Orr
Professor Tresa M. Pollock

To my wife, Melissa S. Wolf

Acknowledgments

I would like to acknowledge my family and friends for the support they have given me throughout my academic career. Special thanks to my grandfather, Frank E. Towsley for encouraging my career in science. Thanks are due to current and former colleagues including Yoosuf N. Picard who showed me the ropes of graduate research, Jeff L. Hendricks for introducing me to the bio side of life, and many others including Jihua Chen, Sarah Richardson-Burns, Aghapi Mordovanakis, Mariano Trigo, Vanita Mistry, and Peter Diehr.

I also acknowledge my advisor, Steven M. Yalisove, for his guidance, encouragement , and coffee over the past several years. I must also thank John A. Nees for his continuous support both scientifically and professionally.

Table of Contents

List of Figures

List of Tables

List of Appendices

Abstract

Near threshold femtosecond laser interactions with materials:
Ablation thresholds, morphologies, and dynamics

by

Joel P. McDonald

Chair: Steven M. Yalisove

This dissertation reports the results of femtosecond (fs, 10^{-15} seconds) laser ablation studies performed on single crystal silicon with oxide thin films and the single crystal Ni-based superalloy, CMSX-4. Emphasis is placed on near threshold ablation (or material removal) phenomena where fs pulsed lasers show significant promise for industrial machining, characterization, materials processing, fabrication of structures, and other applications. Three specific topics are addressed: fs laser ablation thresholds, ablation morphologies, and ablation dynamics. These investigations demonstrate both fundamental aspects of the interaction of fs laser pulses with materials while also introducing novel, previously unobserved phenomena.

The fs laser ablation threshold of single crystal silicon was observed to depend on its naturally occurring oxide, the presence of which increased the ablation threshold of silicon by ~39 % at grazing laser incidence relative to atomically clean silicon. Extension of these studies to ablation threshold measurements on silicon with thermally grown oxide films of varying thickness revealed that despite the high intensities and short timescales of such interactions, the linear optical properties of a surface significantly influence near threshold fs laser ablation.

Femtosecond laser induced blistering or buckling of thin oxide films (20 – 1200 nm) from silicon substrates was observed. Thin film buckling mechanics were used to study the blister features, revealing that the fs laser induced ablation at the oxide film interface participated in the buckling by adding energy to the delaminated oxide film. Furthermore, Isolated blisters could be connected together to create linear fluidic channels. A simple device for performing electrophoresis was fabricated with these channels, the characteristic of this device were studied.

The dynamics of the ablation event were studied in-situ using the technique of pump-probe microscopy with sub-picosecond resolution. Previously developed models of near threshold fs laser ablation were verified and extended by comparing the dynamics captured from two different viewing angles. Furthermore, the dynamics within the first 10 ns of ablation were found to correlate with the final ablation morphology. Finally, an orthogonal, dual-pulse laser induced breakdown spectroscopy method was used to reduce the surface damage associated with this versatile spectroscopy technique.

Chapter 1

Introduction

The fleeting interaction between femtosecond (fs, 10^{-15} seconds) laser pulses and materials has provided fundamental insight into the nature of matter. This dissertation presents a study of near threshold fs laser ablation of crystalline silicon with oxide films and single crystal Ni-based superalloy CMSX-4. Ablation thresholds and morphologies are studied ex-situ, while the dynamics of ablation are captured with ultrafast microscopy and laser induced breakdown spectroscopy. These studies demonstrate fundamental aspects of this unique interaction, while exposing novel applications of fs laser machining previously unexplored.

Early experiments with fs pulsed lasers in the 1980's exploited the ultrashort nature of the laser pulses to probe the interaction of light with materials on previously unexplored timescales [1-6]. These experiments employed pump-probe techniques in which a fs laser pulse was used to "probe" the relaxation of a material from an excited state initiated by a "pump" fs laser pulse. Short-lived (less than a picosecond), highly unstable phases of fs laser excited silicon were observed by monitoring the time resolved reflectivity of a silicon surface following excitation with a 90 fs laser pulse [1]. New carrier relaxation processes such as electron-hole collisions were also observed in silicon [2], along with evidence of ultrafast, non-thermal disordering of the crystal lattice on the 100 fs timescale due to the abrupt excitation of electrons and corresponding loss of bonding [6]. Non-equilibrium electronic excitations of free carriers in metals were also observed, with observation of relaxation to the lattice on the 2-3 picosecond timescale [4]. Pump-probe reflectivity experiments were extended to include microscopic imaging of the thermal melting and evaporation of silicon, revealing for the first time an actual picture of phase transitions with sub-picosecond image exposure times [3]. Pump-probe spectroscopy techniques were also explored, in which the frequency (or wavelength) of the probe pulse was varied along with its delay relative to the pump [7-9], illuminating the breaking and making of bonds in chemical reactions. These studies revealed new physical phenomena not observable with any other technique, while demonstrating the use of fs laser pulses in a variety of applications.

The technique of chirped-pulse amplification invented in the late 1980’s introduced a new class of fs pulsed laser with stable pulse energies and extreme peak powers (10^{12} watts) [10, 11] capable of producing optical breakdown and material removal in dielectrics [12-14], semiconductors [15-18] and metals [14, 19-22]. Much work with fs laser ablation has involved comparisons to longer pulsed, nanosecond (ns) laser ablation of materials [13, 17, 19, 23-26]. Ablation threshold studies performed in SiO_2 as a function of the laser pulse width, τ (150 fs – 7 ns) revealed that the ablation threshold F_{Th} deviated from the empirally observed $F_{Th} \sim \sqrt{\tau}$ for pulse widths below 10 ps [13, 23]. Furthermore, fs laser ablation thresholds were observed to be far more deterministic or precise than those observed ns for pulsed lasers [12, 13, 23]. Decreasing the laser pulse width to the fs regime was also found to increase the quality of laser machined features by decreasing the presence of melt debris [24, 27] and limiting the extent of heat affected zones [28, 29] and collateral damage [30]. The combination of the deterministic nature of fs laser ablation along with the Gaussian spatial intensity profile of laser beams has provided the ability to machined submicrometer features with dimensions as small and smaller than the wavelength of the incident laser light [21, 31-33]. These results indicated the potential of fs lasers for machining applications, as decreased ablation thresholds meant that laser machining could be performed with lower laser pulse energies while producing high quality features with submicron precision.

As more studies revealed the promise of fs lasers for micro-machining, many groups became interested in identifying the physical mechanisms of fs laser ablation. Early pump-probe imaging experiments had revealed the onset of phase transformations within silicon on the subpicosecond timescale, followed by the ejection of droplets of material 10's of nm in diameter which were proposed to completely vaporize on the 100 ps timescale [3]. These initial studies were followed by pump-probe imaging experiments in the late 1990's which extended the timescales of observation to several 10's of ns following absorption of laser energy at the surface [34, 35]. These works demonstrated that near threshold fs laser ablation of semiconductors and metals was accompanied by the ejection of well defined, liquid like layer from the surface of the material [34-36].

The formation of a well-defined liquid like layer was attributed to the coalescence of vacancies into voids at a specific depth due to passing of a rarefaction wave through the molten material [37-39]. Once formed, the well defined liquid layer is ejected following an unsteady isentropic expansion into the air in front of the sample, while a molten pool of material remains on the surface [34-36]. The formation of these interfaces was inferred from the presence of Newton's rings in pump-probe images of near-threshold ablation [34, 35]. Interference of probe light between reflections from these interfaces formed the Newton's rings, the dynamics of which allowed the velocity of the ablating material to be estimated at around 1000 m/s [34, 35]. While thermal in nature, the mechanism of near threshold fs laser ablation is thought to differ substantially with material removal by longer pulses (or higher laser fluences [40-43]) where traditional heterogeneous boiling and evaporation through near-equilibrium states are thought to occur [44, 45]. These observations were paramount in understanding the nature of material removal for fs laser irradiation, and provided a foundation upon which the differences between ns and fs pulsed laser ablation could be resolved.

While advancing the understanding and practical application of fs pulsed lasers, the studies discussed above left several open questions. The role of material surface properties (such as optical reflectivity and roughness) on fs laser ablation thresholds and morphology have not been addressed, as these works focused on identifying the role of laser characteristics on the ablation process. Furthermore, very little attention has been given to the influence of interfaces between dissimilar material on fs laser ablation thresholds, morphologies, or dynamics.

Furthermore, investigations of fs laser ablation morphologies have only recently been performed with sufficient resolution at the submicron level with scanning electron microscopy (SEM) [46-49] and atomic force microscopy (AFM) [50-53], leaving questions regarding the critical structural properties associated with ablation mechanisms and machining applications. Finally, limited correlation between pump-probe imaging of fs laser ablation with other in-situ observation methods has left open questions regarding the physical mechanisms of fs laser ablation, including the properties of the material between the ejected liquid like layer and the molten substrate assumed responsible for the near threshold observation of Newton's rings [34, 35]. In this dissertation, the properties of the material are varied along with laser parameters in order to answer some of these questions left by earlier studies.

1.1 Goals and impact of this thesis

This thesis presents an exploration of the fundamental physical mechanisms underlying laser ablation of materials by investigating fs laser ablation thresholds, ablation morphologies, and ablation dynamics. We have chosen to perform these studies on materials of interest locally to researchers at the University of Michigan, and within the broader materials science community as a whole. Specifically, fs pulsed laser ablation studies were performed on the single-crystal, Ni-based superalloy CMSX-4, and on single-crystal silicon with thin surface oxide films. The unique thermal and mechanical properties of the CMSX-4 superalloy encourage its use in many high temperature applications such as turbine blades in power generation and aircraft engines [54, 55]. The studies discussed here reveal important details of fs laser ablation of the CMSX-4 superalloy with relevance to micromachining [56], in-situ characterization with laser induced breakdown spectroscopy (LIBS) [57], and the mechanisms of fs laser ablation addressed with a combination of pump-probe imaging and FLASH hydrodynamic simulations [56, 58]. Single-crystal silicon is the foundation of the microelectronics industry [59, 60], and has served as the material of choice for many studies of the effects of fs laser pulses on materials [1-3, 17, 50, 52, 61-72]. The results of the investigations presented in this dissertation reveal the role of the native oxide of silicon on fs laser ablation in ultra-high vacuum (UHV) [73], while demonstrating interesting morphologies that result from fs laser ablation of silicon with thicker oxide films [74-76], and verifying mechanisms of near threshold fs laser ablation with pump-probe imaging performed from multiple imaging angles [77].

Within the framework of understanding the physical mechanisms of fs laser ablation, the goals of this dissertation include:

A. **Identify the role of transparent oxide films on fs laser ablation of crystalline silicon.**
    1. Determine the influence of the native oxide of silicon on the ablation threshold and corresponding ablation morphology with comparisons to atomically clean silicon (Chapter 3.1 and 4.1).
    2. Explore the role of thicker, thermally grown and plasma enhanced chemical vapor deposited oxide films on the fs laser ablation threshold and ablation morphology (Chapter 3.2 and 4.2).
    3. Characterize the laser ablation dynamics of silicon with oxide films (native and thermally grown) to clarify established models of near threshold fs laser ablation (Chapter 5.1)

B. **Characterize the dynamics of fs laser ablation of the Ni-based superalloy CMSX-4 in order to further understand the resulting ablation morphology.**
    1. Determine the fs laser ablation threshold of the CMSX-4 superalloy and characterize the resulting ablation morphology both

quantitatively and qualitatively over a broad range of laser fluence (Chapter 3.3 and 4.3).

2. Establish whether the dynamics of fs laser ablation of the CMSX-4 superalloy on the ns timescale are related to the observed ablation morphology at infinity (Chapter 5.2).
3. Exploit knowledge of fs laser ablation dynamics to investigate an orthogonal, dual-pulse laser induced breakdown spectroscopy (DP-LIBS) technique to reduce the surface damage associated with the LIBS technique (Chapter 5.2).

While illuminating the fundamental physics underlying fs laser ablation, this dissertation also provides significant practical impact related to fs laser machining of materials. The roles of long ignored material properties including the native oxide of silicon and interfaces between dissimilar materials demonstrate the sensitivity of the fs laser/material interaction, while emphasizing the importance of surface conditions on ablation morphologies. The unique benefits of fs laser machining are exposed by exploring near threshold phenomena, revealing the strengths of this relatively low average power laser source. Finally, thorough, in-situ observation of the fs laser/material interaction reveals critical aspects of ablation, verifying models developed by other groups and revealing the dynamics of ablation phenomena previously not observed. The techniques and methods presented in this dissertation can be extended to a broad range of materials, and it is the hope of the author that suggestions for future research will yield equally valuable results.

Chapter 2

Background

A review of prior research related fs laser ablation thresholds, ablation morphologies, and ablation dynamics is presented in this chapter. Emphasis is placed on semiconductors and metals in order to provide sufficient background to the fs laser ablation experiments presented in this dissertation, however the characteristics of fs laser ablation of dielectric materials will be mentioned when appropriate.

2.1 Femtosecond laser ablation threshold

In this section details of the single pulse femtosecond laser ablation threshold are discussed, including techniques for measuring the ablation threshold, reported threshold values for silicon, SiO_2, the CMSX-4 superalloy, and related materials. Models and mechanisms for fs laser ablation of metals, semiconductors and dielectrics proposed in the literature will also be presented.

2.1.1 Definition of the ablation threshold

The ablation threshold of a material is defined as the incident laser fluence required to remove matter from its surface with a single laser pulse [52]. The ablation threshold should not be confused with the modification threshold or melting threshold of a material which does not necessarily involve material removal [50, 53, 78, 79]. Furthermore, the multiple-pulse ablation threshold has been found to be lower than the single pulse ablation threshold for many materials due to so called incubation effects [49, 80-84]. In this dissertation, we focus primarily on single pulse experiments.

2.1.2 Measurement of the ablation threshold

The most common method of experimentally determining the ablation threshold is to measure the diameter of single pulse fs laser ablation features as a function of incident laser fluence, and then perform a fitting routine (based on the laser beam spatial intensity profile) to determine the laser fluence at which the ablated feature diameter shrinks to zero [49, 50, 52, 80-86]. In some cases, the spatial intensity profile of the laser beam is super-imposed over an image of an ablation feature, so that the local fluence where ablation ceases can be determined from a calculated beam profile [87]. Other in-situ techniques such as light scattering and plasma emission have also been used. For transparent materials, the presence of damage has been determined by monitoring the transmission of light though regions where laser induced damage may be present [12, 23, 85, 88]. It should be mentioned, however, that modification of the material not necessarily associated with ablation may lead to a change in the transmitted light intensity, such that only “damage” or “modification” thresholds can be determined with this technique. Finally, the optical emission associated with the ablation plasma can be monitored, with the ablation threshold being the laser fluence at which the optical emission from the plasma ceases [23]. As will be discussed in detail later, material removal at laser fluences near the ablation threshold is thought to be dominated by the ejection of a thin liquid layer of material that does not emit light like an energetic plasma [35]. For silicon, for example, the plasma threshold is around 1.0 J/cm^2, and the ablation threshold is around 0.3 J/cm^2 [15]. It cannot be overstressed that ablation threshold measurements are highly dependent on the particular experimental conditions used for a particular study (such as beam focusing, environment, etc.). This is demonstrated in [50] where the range of reported values of the fs laser ablation threshold of silicon are presented, and in [89] where the variation of ablation threshold of dielectrics with the focused laser spot size is discussed.

2.1.3 Models and mechanisms for fs laser ablation of dielectrics, semiconductors, and metals

A brief review of relevant models detailing the transfer of incident laser energy to the material are presented, and the associated mechanisms of fs pulsed laser induced material removal are discussed. Although verification of models is not the focus of this dissertation, it is useful to place the observations of fs laser ablation thresholds, morphologies and dynamics within the context of the electronic, thermal, and physical phenomena proposed to underlie ultra-short pulsed laser ablation.

In general, the incident laser pulse imparts its energy to the electrons present in the conduction and valence bands within the material. These electrons transfer their energy to the ions, and ablation occurs if the resulting temperature exceeds the evaporation temperature of the material. The models for ablation presented below discuss how the energetic electrons are produced, what happens once the electrons are excited, and the timescales over which they yield their energy to the ions. A discussion of the physical mechanisms for material removal follows. The mechanisms for dielectrics, semiconductors, and metals are presented independently as the interaction fs laser/material interaction is dependent on electronic structure.

For dielectrics, a critical density of free electrons ($\sim 1 \times 10^{21}$ cm^{-3}) must be generated within the material by the action of the incident laser pulse in order for ablation to occur [23, 90]. Exactly how the critical free electron density is produced has been debated in recent years [12, 13, 33, 91-93]. The generally accepted picture includes a process known as avalanche ionization, in which the large electric field of the incident laser pulse accelerates “seed electrons” which in turn collide with bound electrons creating an “avalanche” of free electrons. The debate lies in the source for these seed electrons. Two distinct, nonlinear phenomena are often cited; multiphoton seeded avalanche ionization in which electrons are sequentially excited from the valence band to the conduction band though the absorption of several photons [13, 91, 94], and Zener-impact ionization seeded avalanche ionization, in which seed electrons are created by tunneling through an atomic field potential barrier that has been highly bent by the electric field of the fs laser pulse [12, 33, 95]. Recently developed multi-rate equations (considering both the time-dependent energy distribution and density of free electrons [96]) show that the contribution of Zener-impact ionization depends on the laser fluence, with multiphoton ionization dominating for low laser fluences, and Zener-impact ionization dominating for higher laser fluences [92].

Ablation or removal of material proceeds once the critical density of electrons is produced. A mechanism known Coulomb explosion has been proposed to explain material removal for dielectrics by ultrashort (sub picosecond) laser pulses near the threshold for ablation [97-100]. With Coulomb explosion, the incident laser pulse imparts it energy to the electrons near the surface of the material. These electrons then escape from the surface, leaving behind a region of positively charged ions. In dielectrics, where the mobility of free carriers is low, electrons from the surrounding material do not have time move into the electron depleted region before the highly charged material explodes outward due to a common Coulombic repulsion [97-100]. Evidence for the Coulomb explosion phenomenon in Al_2O_3 includes time-of-flight mass spectroscopy experiments in which singly and doubly ionized O^+ ions were observed to exhibit kinetic energies proportional to their net charge [100]. Coulomb explosion is not thought to occur in metals and semiconductors because carrier transport is fast enough to neutralize the near surface region of the material initially depleted by the escape of energetic electrons [101]. It should be emphasized however, that the Coulomb explosion mechanism is thought to occur near the ablation threshold, and that for laser fluences far exceeding the ablation threshold, traditional thermal mechanisms for ablation are thought to occur in dielectrics [100, 102]. These thermal processes result when the energetic electrons scatter phonons (lattice vibrations) resulting in heating and eventually removal of material if temperatures exceeding the vaporization temperature are produced [102, 103].

For semiconductors, the incident laser pulse is again absorbed by the electrons in the material generating a dense electron-hole plasma within the near surface of the material. Both two-photon ionization [64] and avalanche ionization [63] have been cited as the mechanisms responsible for the production of these electrons. Of note is that the generation of the dense plasma dramatically decreases the absorption depth of the laser pulse by the process inverse Bremsstrahlung absorption by the free carriers [63, 64, 98]. As a result, the laser energy is deposited within the first several 10's of nm of material, a short distance relative to the skin depth of silicon (for example) which is on the order of 3 – 7 μm for optical wavelengths [64]. Equilibrium is established within electron system through carrier-carrier collisions, typically on the time scale of several 10's of fs [5, 104].

A phase transition within the semiconducting material proceeds if an electron-hole plasma of sufficient density is established ($0.5 - 1.0 \times 10^{22}$ cm^{-3}, or about 10% of the available valence band electrons) [105]. On the picosecond timescale, the lattice temperature rises due to collisions between the energetic electrons and the lattice [66, 105], and melting and ablation of material proceeds if sufficient temperatures are reached [106]. Distinct thresholds for melting and ablation exist for semiconductors [15]. For laser fluences below the ablation threshold, but above the melting threshold, a near surface region of the sample melts and sublimation of small clusters of atoms have been observed via time of flight mass spectroscopy [69]. This phenomenon does not yield removal of material that is observed by other means, and is therefore generally not considered ablation. For higher laser fluences, a process known as *non-thermal* melting has been proposed to occur in the first few hundred fs before the thermal effects associated with melting have time to occur (> 1 ps) [38, 62, 86, 105, 107]. For non-thermal melting the atoms in the lattice drift from their equilibrium positions on the time scale of 100's of fs due to the loss in bonding from the sudden excitation of the valence band electrons. The ablation threshold for silicon is around 2 times the melting threshold [52], while ultrafast disordering of the lattice is thought to take place at laser fluence of around 1.5 times the melting threshold [38, 107], such that non-thermal melting may not be accompanied by significant material removal.

At the ablation threshold, thermal mechanisms emerge as the dominant force in material removal in semiconductors [37, 70]. Near the threshold for ablation, the transfer of energy from the electrons to the lattice produces a sudden thermal expansion, producing a rarefaction wave that proceeds into the material facilitating the nucleation of stable voids by the aggregation of vacancies [37, 38]. These voids eventually coalesce forming a very low density region some 10's of nm beneath the surface, allowing for the ejection of a liquid like layer from the surface [34, 35, 37-39]. For yet higher laser fluence (2.5 - 5 times ablation threshold [15]), time of flight mass spectroscopy experiments indicate that the ablation of material takes place in two stages; fast "suprathermal" ions initially are ejected (~ 10^5 m/s) from the surface of the material (the clusters mentioned earlier), followed by the slower thermal ion component of the ablation plume (~ 10^4 m/s) [68, 69]. The ablation plume then takes the form of a two phase fluid in which liquid drops coalesce from and are dispersed in a vapor of ions [38, 44].This regime has been associated with an increase in material removal and a change in the qualitative nature of the ablation crater [38, 44].

As metals posses an intrinsic free carrier population within the conduction band, the excitation of electrons by an incident fs laser pulse is slightly different than was discussed for insulators and dielectrics. However, it should be noted that due to rapid ionization in dielectrics and semiconductors at laser fluences appropriate for ablation, free carriers also dominate the absorption of the incident laser energy [98]. In any case, in the absence of interband transitions [20, 108] the free electrons of the metal absorb the laser pulse producing a dense plasma within a region of the surface defined by the skin depth of the material (for d-band metals) or the ballistic range of energetic electrons (for s/p band metals) [19, 108]. This distinction between d and s/p band metals is attributed to probability of electron-phonon collisions, which dictates how effectively the electrons transfer their energy to the lattice [109-111]. In d-band metals the larger density of states results in a higher collision rate (superior electron-phonon coupling) for ballistic electrons which limits their penetration to the skin depth of the material. For s/p band metals, the lesser density of states results in a decreased collision rate (inferior electron-phonon coupling) allowing for greater penetration by the ballistic electrons to a depth defined by the mean free path of an energetic electron [109].

The transfer of energy from the energetic electrons to the lattice is achieved by the electron-phonon collisions on the picosecond timescale [4]. Theoretically, the transfer of energy from the electrons to the lattice has been treated with a two-temperature model, which describes the evolution of the linked but independent temperatures of the electron and lattice subsystems [20, 101, 108, 109, 111]. The mechanisms for material removal are largely the same as those proposed for semiconductors above. For laser fluences below the ablation threshold, but above the melting threshold, some evaporation from the surface may occur which does not yield measurable removal and is therefore not considered ablation [112]. For laser fluences just exceeding the ablation threshold, the formation of defects which coalesce into in the material just below the surface results in the ejection of a liquid layer from the surface of the material [34, 35, 38]. For still higher laser fluences, thermal mechanisms such as boiling and evaporation dominate material removal [40-43]. As with semiconductors, evidence for two regimes of material removal as a function of incident laser fluence has been found in many studies of fs laser ablation of metals [19, 20, 22, 80, 113].

In summary, models and mechanisms treating the absorption of and resulting ablation by fs laser pulses has been reviewed. These mechanisms are both material and laser fluence dependent. Although not addressed above, the ablation studies as a function of laser pulse duration provide additional insight into the mechanisms underlying short pulsed laser ablation [13, 18, 19, 23, 26, 114].

2.1.4 Ablation threshold of crystalline silicon, bulk SiO_2, the Ni-based superalloy CMSX-4, and related materials

As discussed in [52], there is a spread in reported values for the single pulse ablation threshold of crystalline silicon ranging from 0.15 – 0.52 J/cm^2. The spread in values has been attributed to the variety of detection methods used to determine the ablation threshold, incident laser pulse temporal width, and the environment in which the ablation took place [52]. For comparison to the values presented in this dissertation, the single pulse ablation threshold for Si(100) with a native oxide irradiated in air determined from atomic force microscopy (AFM) was found to be 0.28 J/cm^2 [63]. The effect of the native oxide of silicon is rarely addressed and it has been suggested that a laser fluence of 0.41 J/cm^2 is required to ablate the native oxide from a Si(111) surface, while the ablation threshold of the Si(111) itself was 0.52 J/cm^2 [52]. Ablation experiments have also been performed with atomically clean Si(100) under ultra-high vacuum (UHV) conditions, however this work focused on the ablation morphology and the ablation threshold was not mentioned [17].

The reported values of the single pulse fs laser ablation threshold of bulk SiO_2 range from 3.7 J/cm^2 for amorphous SiO_2 with a 150 fs laser pulse [85] to 1.5 J/cm^2 for 5 fs laser pulse [12]. Single pulse surface *damage* thresholds were found to range from ~1.1 – ~ 8.0 J/cm^2 for laser pulse widths ranging from 5 fs – 3 ps at a laser wavelength of 780 nm [90] and from 2 – 4 J/cm^2 for laser pulse widths ranging from 400 fs – 1 ns at a laser wavelength of 1053 nm [13]. Damage thresholds within bulk fused silica (i.e. inside the surface) were found to be 3.5 J/cm^2 at a laser wavelength of 800 nm, and 3.2 J/cm^2 at a laser wavelength of 400 nm [88]. It has been observed that the focused beam radius used for ablation threshold studies has a significant influence on the measured ablation threshold, with the threshold general decreasing with increased beam radius from ~1.0 J/cm^2 at a beam radius of 20 μm down to less than 0.2 J/cm^2 at a beam radius of ~ 425 μm [89]. This dependence on the focused beam radius was attributed to presence of defects within the glass that encourage ablation by generating free carriers. It was suggested that a given glass has a certain density of these defects, and that larger beam radii allow more of these defects to be encountered by the laser light, thus decreasing the ablation threshold [89].

Single pulse ablation threshold values of 0.332 ± 0.014 J/cm^2 [115] and 0.300 ± 0.030 J/cm^2 [116] have been reported for the Ni-based superalloy CMSX-4. Additionally, two regimes of ablation have been identified marked by a change in the ablation morphology and depth of ablation craters as a function of incident laser fluence. The ablation threshold cited above (0.300 ± 0.030 J/cm^2) is the threshold fluence for the low fluence regime, while the threshold for the high fluence regime was found to be 5.3 ± 0.5 J/cm^2 [116]. As mentioned previously, low and high fluence regimes of fs laser ablation have been observed for many materials [19, 20, 22, 80, 113].

The single pulse fs laser ablation thresholds of other bulk materials are briefly cited for the sake of comparison. For semiconductors, the ablation threshold of GaAs and InP were measured to be 0.226 ± 0.02 J/cm^2 and 0.170 ± 0.014 J/cm^2 respectively at a laser wavelength of 800 nm and a pulse duration of 130 fs [47], while the ablation threshold of GaN was found to be ~0.3 J/cm^2 [117]. The ablation threshold for Ge was reported to be 1.32 J/cm^2 at a laser wavelength of 800 nm, and a pulse width of 130 fs [118]. The damage threshold for C in the diamond phase (type IIa diamond) was found to be 4.0 J/cm^2 at a laser wavelength of 800 nm and a pulse duration of 200 fs [119], and 0.6 J/cm^2 at a wavelength of 248 nm and a pulse duration of 500 fs [120].

For bulk crystalline metals, the ablation thresholds of Ni and Ni_3Al were found to be 0.384 ± 0.03 J/cm^2 and 0.364 ± 0.03 J/cm^2 at a laser wavelength of 780 nm and a pulse duration of 150 fs [116]. The ablation thresholds of stainless steel, Cu, Nb, and Ti were found to be 0.21 ± 0.02 J/cm^2, 0.58 ± 0.05 J/cm^2, 0.19 ± 0.03 J/cm^2, and 0.28 ± 0.02 J/cm^2 respectively, at a laser wavelength of 780 nm and a pulse width of 150 fs [80]. Discrepancies in threshold values obtained by different groups under nearly identical laser conditions are common, with one example being the ablation threshold of Cu determined to be 0.58 ± 0.05 J/cm^2 in [80], and ~0.14 J/cm^2 in [20].

The ablation threshold of thin films, including dielectric [121, 122], semiconductor [123, 124], and metallic thin films [110, 111, 125] on typically insulating substrates has also been investigated. In contrast to the work presented in this thesis, these investigations have focused on the ablation characteristics of the thin film materials, and have not identified the role of the thin films on ablation of the substrate. Although different than the studies presented in this dissertation, many fundamental insights into the fs laser/material interaction have resulted from these studies and the ablation threshold results are presented for reference.

Single pulse fs laser ablation was studied as a function of pulse duration (25 fs – 1.3 ps) for several oxide films (TiO_2, TaO_2, HfO_2, Al_2O_3, and SiO_2) with different band gaps on fused silica substrates [121]. For a constant pulse duration, the ablation threshold showed approximately a linear dependence on the band gap energy. Furthermore, the observed dependence on the pulse duration indicated that avalanche ionization plays the most significant role in excitation and breakdown [121]. The damage threshold of ~1 μm thick triazenepolymer film on a glass substrate was determined at a fixed laser wavelength of 800 nm as a function of the temporal pulse width, ranging from 0.495 J/cm^2 for a 130 fs laser pulse to ~0.8 J/cm^2 for a 2.6 ps laser pulse [122]. The authors interpreted the relatively weak dependence of the damage threshold on the pulse duration to suggest that the ablation of material was seeded by free carrier absorption followed by avalanche ionization [122]. Ablation threshold and time resolved reflectivity studies for 200 nm ceramic ZnO wide bandgap, semiconducting films have found a similar increase in the ablation threshold (0.39 - 0.54 J/cm^2) with an increase in pulse duration from 70 fs to 700 fs (wavelength = 800 nm) [124].

For Au, Ni, and Mo thin films (10 – 1500 nm in thickness) on fused silica substrates, the measured fs single pulse damage threshold was found to increase with increasing film thickness eventually saturating at ~0.11 J/cm^2 for Au, 0.022 J/cm^2 for Ni, and 0.048 J/cm^2 for Mo [110]. The dependence of the damage threshold on the film thickness was attributed to the strength of electron-phonon coupling in the materials [110, 111], however no mention was made of the role of the interface between the film and the substrate which may also influence the observed trend and should be considered in future work.

In summary, the fs laser ablation threshold of a wide range of material has been presented. It was observed that ablation threshold measurements on the same material under very similar conditions can yields a wide range of results [52]. In general, the ablation threshold for dielectrics is higher than that observed for dielectrics which may be expected from presence of free carriers within conductors which can easily absorb the incident laser light, in contrast to dielectrics where the free carriers are generated by multiple step processes such as avalanche ionization. The following section reviews the surface morphologies that have been observed to result from fs laser ablation.

2.2 Fs laser ablation morphology

In general, permanent modifications to the topography of a surface resulting from the deposition of laser energy is referred to as laser ablation morphology. Examination of the ablation morphology produced by fs pulsed irradiation has been performed with a wide range of techniques, including optical microscopy (OM), scanning and transmission electron microscopy (SEM and TEM), along with scanning probe microscopy techniques (SPM) such as atomic force microscopy (AFM). The following sections provide a review of investigations of fs laser ablation morphology for several materials, with emphasis on the Ni-based superalloy CMSX-4 and crystalline silicon. The focus of the review is the ablation morphology resulting from single pulse fs laser irradiation, however multiple pulse ablation morphologies are also addressed with a review of laser induced periodic surface structures (LIPSS) or ripples.

2.2.1 Single and multiple pulse Fs laser ablation morphology

Reports of the ablation morphology produced on dielectrics with single fs laser pulses are limited in the literature; however several key results will be discussed here. By using tight focusing of the fs laser beam (NA = 1.6), and by exploiting the sharp deterministic ablation threshold of SiO_2, features with diameters as small as 20 nm have been produced with single fs laser pulses at a wavelength of 527 nm near the ablation threshold [33]. The ablation morphology, observed via SEM after the glass samples had been coated with Au, was found to be highly repeatable and exhibited smooth edges with minimal debris surrounding crater features [33]. As glasses are often transparent at the wavelengths of Ti:sapphire fs pulse lasers (typically around 780-800 nm), ablation features can be produced by focusing the laser at both the front surface and back surface of samples [33, 126]. The single pulse ablation morphology was found to be significantly better when the laser was focused at the back surface of a glass sample, with less deposited debris surrounding features, sharper feature edges, and smaller attainable feature size [126]. In addition to ablation craters, “micro-voids” were created when the focus was located 2-4 μm beneath the sample surface, yielding bubble like features at the surface [126]. AFM analysis of high-fluence (5 times threshold) single pulse ablation features produced on borosilicate glass with front-side focusing revealed a smooth bottomed crater surrounded by a super-surface rim, outside of which thin strips of melted material were present extending away from the ablation feature [127]. The height of the rim above the surrounding surface was observed to increase with increasing laser fluence, and was attributed to pressure driven flow of melted material from the center to the edge of the ablation crater followed shortly by re-solidification of the material at the rim [128].

Studies of the ablation morphology from single fs laser pulses on polycrystalline MgO revealed preferential ablation near crystal grain boundaries [93]. Similar observations have been made with single pulse ablation of anodic Al oxides where preferential ablation near cracks in the films was observed [129]. Examination of single pulse fs laser ablation features on polymers including PMMA and PC were found to exhibit a bubbled surface with more material above the original surface plane than below it for laser fluences 2-3 times the ablation threshold [83]. This phenomenon was attributed to the formation of gaseous products from the breakdown to CO-O bonds, yielding local bursting of the surface and ejection of melted material [83].

The ablation morphology resulting from single pulse fs laser irradiation [50, 52, 67] and multiple pulse [16, 50, 81, 130, 131] on crystalline silicon has been studied over a range of incident laser conditions. The single pulse ablation of Si at a laser fluence of 0.64 J/cm^2 was found to exhibit both super-surface features (material extending above the original plane of the surface like the crater rims discussed previously for fs laser ablation of glass) and crater formation [52, 67].

For most laser fluences, the central ablation crater (into the surface) is surrounded by a annular rim of material extending above the sample surface (50 – 150 nm), with the rim becoming more pronounced with increasing laser fluence [67]. TEM of this rim reveals the presence of polycrystalline grains of Si (~ 20 nm in diameter [67]). For laser fluences very near the ablation threshold (0.64 J/cm^2), AFM analysis revealed that the center of the ablation feature consists of a super-surface protrusion surrounded by a crater [52]. Furthermore, localized pits of ablation ~ 1 – 5 μm in diameter, ~ 100 nm in depth have been observed within the ablation crater and attributed to normal boiling (heterogeneous nucleation from the surface) following the initial phase of material removal by spallation of a thin liquid like layer [34, 35] or vaporization [50].

The phase of the silicon remaining in the ablation crater has also been addressed [52]. Micro-Raman spectroscopy revealed the presence of re-crystallized, polycrystalline silicon (5 – 10 nm grains) within the ablated region, while a rim of amorphous silicon immediately surrounds the ablated region [52]. The ablation morphology on silicon was found to evolve with increase laser fluence, being highly repeatable up to a laser fluence of around 1.7 J/cm^2, after which large drops of re-solidified material was observed to surround the ablation crater suggesting a violent explosion [67]. The change in morphology may be attributed to a change in the mechanism for ablation [132] (perhaps the onset of heterogeneous boiling [50]). Similar ablation morphologies and associated morphology evolution with laser fluence have been reported for other semiconductors, including InP [51] and GaAs [47].

The single pulse fs laser ablation morphology of the Ni-based superalloy CMSX-4 has recently been investigated [115, 116]. Single shot studies presented in [116] discussed the presence of two distinct ablation morphologies, the presence of which were dependent on the incident laser fluence. In the low fluence regime (incident laser fluence between the ablation threshold, 0.300 ± 0.030 J/cm^2 and 5.3 ± 0.5 J/cm^2) the ablation morphology exhibits very limited melting and no micro crack formation. However, in the high fluence regime (incident laser fluence greater than 5.3 ± 0.5 J/cm^2), the ablation morphology showed clear evidence of melting with a molten layer 1 – 3 μm beneath the high fluence ablation morphology [116]. Similar single fs laser pulse ablation morphology evolution, specifically the onset of a melt like morphology at higher laser fluences, has been reported for other metals including Fe [133], Al [134], and Cu [20]. As was observed for the Ni-based superalloy CMSX-4 [116], the change in the qualitative nature of the ablation morphology was found to occur at a similar fluence as a sudden increase in the ablated crater depth as a function of increasing laser fluence [19, 20, 22, 80, 133-136]. As discussed above with respect to the ablation threshold dependence on thin metal films (see Chapter 1.2.4 and references [110, 111]), the sudden increase in crater depth with increasing laser fluence was attributed to a change in the depth of heating due to transport of ballistic electrons into the material past the depth initially defined by the skin-depth of the material. The diffusion of energetic electrons may lead to a less defined region of heating, leaving some molten material on the surface which solidifies over time following the ablation event [133, 134]. While this may partially explain the presence of re-solidified material on the surface, the variability in the qualitative nature of ablation craters in the high fluence regime may simply indicate the onset of heterogeneous boiling [40-43] which is less deterministic than the near threshold spallation mechanisms discussed earlier [37, 38].

The single pulse fs laser ablation morphology has also been studied for thin dielectric [137, 138], semiconductor [123, 124], and metallic films [139-141] on a range of substrates. As with bulk materials, a range of ablation morphologies were observed as a function of the incident laser fluence. For fluences near the ablation threshold, a swelling or buckling of the film was observed for all film types [123, 137, 142], in which the film either swelled due to a change in phase (from diamond-like carbon to graphite [123]), or buckled up from the substrate due to local delamination [137, 142]. Both of these phenomena demonstrate interesting physics of fs laser ablation. Fs laser induced phase changes due to the extreme temperatures reached during ablation and the subsequent high cooling rates have been explored by Yoosuf N. Picard in his recent dissertation

[143]. The mechanics of thin film buckling has been addressed extensively in the literature [144-151]. The delamination of and buckling of thin films via laser irradiation has been observed for ns laser irradiation of 300 nm Al films on glass substrates [152], and thermally grown oxide films on Si substrates [153]. In these case however, application of conventional thin film buckling mechanics was not pursued due to the thermal effects associated with the longer ns laser pulses [152, 153].

Returning to fs laser ablation, for appropriate laser fluences the thin films for all material types were observed to be removed from their respective substrates. For cases where the ablation threshold of the film was less than that of the substrate, laser fluences were determined which allowed for removal of the film without ablating the substrate (for single shot [139, 141] and for multiple shot [125, 154]). For the cases where the ablation threshold of the film material was greater or similar to that of the substrate, fs laser induced removal of the film typically resulted in damage to the substrate (for single shot [137], and for multiple shot [155]) although in certain cases damage to the substrate was limited through the choice of appropriate laser conditions (as in the case of PMMA on W, but not for PMMA on Ti [137]).

A common feature of multiple pulse ablation morphologies produced with linearly polarized fs laser irradiation is the presence of laser induced periodic surface structures (LIPSS) or ripples within ablation craters or along machined channels. A universal phenomenon of near threshold pulsed laser ablation [156, 157], these ripple features have been observed in dielectrics [87, 158], semiconductors (including silicon) [46, 130], and metals (including the Ni-based superalloy CMSX-4) [116, 159]. The ripple amplitude is typically on the order of 10's of nm, and run perpendicular to the laser polarization. Ripples with periodicity similar to the wavelength of the laser irradiation have been observed (low spatial frequency LIPPS or LSFL, 80 – 90 % of the laser wavelength), as well as ripples with a period much less than the wavelength of the laser (high spatial frequency LIPPS or HSFL, ~20 % of laser wavelength) [46, 158]. A variety of models have been proposed to address the formation of such periodic surface structures, including; inhomogeneous energy absorption due to interference between incident laser light and a surface scattered wave from surface roughness [160], the capture of defect upon rapid solidification from the melt [161], and self-organization of the surface from the melted state (in analog to ripples in sand under wavy, shallow water) [162]. In light of these competing models, the mechanism for the ripple formation is still very much an open question [46].

At higher laser fluences (~1.0 J/cm^2) a different microstructure was observed consisting of sharp conical spikes [16, 163] on silicon surfaces. It was observed that the sharpness of the spikes was dependent on the background gas in which samples were irradiated, with the presence of sulfur resulting in much sharper cones with homogeneous dimensions. A mechanism accounting for the morphology formation which incorporated the sulfur was not presented [163]. The presence of sulfur in the background gas was also found to greatly increase the infrared absorption of the silicon surface, producing what has been called “black silicon ” [76]. The increased absorption may result from incorporation of sulfur into the near surface silicon which would create a tail of states below the band gap allowing for greater absorption within the IR [163].

In summary, single pulse femtosecond laser ablation of dielectrics, bulk silicon, and the CMSX-4 superalloy were reviewed, along with a discussion of thin film and multiple-pulse ablation morphologies. Critical aspects of the studies include the presence of both ablation craters and super-surface morphologies including rims and protrusions. Higher laser fluences were observed to increase variability in the ablation morphology for all materials. Fs laser ablation morphologies produced on samples with thin films included both film buckling and swelling, and complete removal of the film for appropriate laser fluences. Finally, multiple-pulse ablation morphologies commonly include laser induced periodic surface structures (LIPSS) or ripples which are a common feature of pulsed laser ablation with polarized radiation. At higher laser fluences, multiple pulse fs laser ablation performed in a background gas containing sulfur was found to produce a well organized, highly absorbing spike like morphology called black silicon.

2.3 Fs laser ablation dynamics

In this work, the dynamics of fs laser ablation were characterized in-situ with pump-probe microscopy, dual-pulse fs laser induced breakdown spectroscopy (DP-LIBS), and simulated with 2D-FLASH hydrodynamic code with initial conditions provided by 1D HYADES simulation code. These efforts revealed several details of fs laser ablation phenomena, including the velocities of ablating materials, the role of increasing thermal oxide film thickness on ablation of crystalline silicon, and the connection between the morphology and dynamics of fs laser ablation. Background information on the techniques used to explore the dynamics of fs laser ablation are presented in the following sections.

2.3.1 Fs laser based pump-probe microscopy

While useful for machining applications, the ultrashort nature of fs laser pulses make them ideally suited to probe phenomena which take place on the picosecond (ps) or even sub-ps time scale. Under the general heading of pump-probe techniques, a pump laser pulse initiates some phenomenon, and a probe pulse is used to is study the evolution of the phenomenon as a function of time. Initial pump-probe experiments with ultrashort pulses were largely devoted to the dynamics of laser induced electronic excitation and plasma formation in crystalline silicon by studying the reflection of a probe pulse from the surface of an irradiated material as a function of time [1, 2, 6]. Through these works, sub-ps electronic excitation times were measured, while subsequent relaxation of energy to the lattice and the onset of ablation of material for sufficient intensities were observed on the time scale of 1-10 ps. These initial pump-probe experiments were extended to study ultrafast phenomena in other materials, including metals [108], water [164], and proteins involved with photosynthesis in plants [165].

A physical picture of ultrafast events also be obtained with pump-probe microscopy, an extension of traditional pump-probe reflectivity experiments. For pump-probe microscopy applications, a fs duration probe pulse serves as the flash of a camera, capturing an image of an event with an effective exposure time limited only by the length of the laser pulse. Pump-probe imaging of fs laser induced material breakdown was initially performed on silicon in the *front-view* imaging geometry (akin to traditional reflection mode optical microscopy), in which an image is formed with probe-pulse reflected from a region excited with a pump-pulse [3]. This technique was later extended to additional materials including other semiconductors and metals, and to a greater range of time delays following excitation [34, 35]. These studies shed light on the physical nature of ultra-short pulsed laser ablation, as well as the critical time scales for material removal. Near the ablation threshold, front-view images of ablations contained a phenomenon known as Newton's rings [34, 35]. The presence of these rings required two sharp interfaces from which reflections could be produced and subsequently interfere with each other. This suggested a mechanism for near threshold ablation in which a thin (< 10 nm) well defined liquid like layer of material was ejected from the surface at speeds of approximately 1000 m/s [34-36], which has since been supported by simulation of the ablation event [38]. However, the velocity of ablating material inferred from the front-view images lacked precision as a sufficient model for the optical properties of the materials separating the two interfaces responsible for the Newton's rings was not obtained [34, 35].

Other imaging geometries have been used to study fs laser ablation, including *side-view* imaging or shadowography, in which an image is formed with a pump pulse that has passed laterally through an ablation event [41, 65, 72, 166]. These side-view images show the presence of ablating material, and a shock wave which travels in the air in front of the sample [41, 65, 72, 166]. The shock wave is produced by the sudden thermal expansion of the surface following absorption of the laser pulse energy [167, 168]. Analysis of the shock wave dimensions as a function of time using theory developed by L. I. Sedov yields the shock front velocity and information on the energy release for the shock wave accompanying the laser ablation as well as the pressure evolution of the shock wave as a function of time [169]. This analysis was initially applied to the shock wave of the atomic bomb in 1946, where the energy release of the bomb was determined from time-resolved images of explosion [169, 170].

From time resolved side-view images of fs laser ablation of Si at a peak laser fluence of 2.0 J/cm^2 and 3.0 J/cm^2, it was found that 10 % and 17 % respectively of the incident pump pulse laser energy was converted to the energy underlying the air shock wave [65]. Furthermore, the pressure at the shock front in air ranged from ~30 MPa at 18 ns after the onset of ablation, down to ~ 5 MPa at 57 ns after the onset of ablation for a pump laser fluence of 3.0 J/cm^2 [65]. Additional studies comparing ns and fs laser ablation of Si revealed that the shock wave is largely spherical in nature for ns laser ablation, corresponding to a massless point release of energy [72]. In contrast, the shock wave associated with fs laser ablation exhibited a strong one-dimensional component, with a initial propagation largely perpendicular to the sample surface, followed by a transition to more spherical propagation at a later time [72]. If visible in side-view images, the velocity of ablating material can be measured directly [65], in contrast for front-view imaging where appropriate optical models for the Newton’s rings must be developed first with knowledge of the real time optical properties of the system [34, 35]. In [65] it was noted that at laser fluences around 2-3 J/cm^2, the removal of material begins with plasma formation at around 10 ps, followed by a slower core of ablation that emerges at around 30 ns. Finally, the velocity of the shock wave in air accompanying the ablation event was found to depend significantly on the pressure of the gas into which it propagated [166]. With a background gas of argon, the velocity of the shock wave was found to decrease from around 10,000 m/s for a background pressure of 2 Pa (0.02 mbar), to ~400 m/s at a background pressure of 9×10^4 Pa (900 mbar) [166].

2.3.2 Dual pulse laser induced breakdown spectroscopy

Laser induced breakdown spectroscopy (LIBS) is a technique that can be used to determine the elemental constituents of a material through collection and analysis of the radiation emitted by the plasma that is produced when a laser pulse ionizes and ablates a material. LIBS has been used for localized chemical analysis of a wide range of materials, including metals (in both liquid [171-173] and solid form [174-180]), semiconductors [181, 182], dielectrics [174, 183, 184], and gas phase materials [185, 186]. The ability to characterize samples in-situ and quickly obtain qualitative and quantitative [187] analysis of chemical composition without complete destruction of the sample makes LIBS a particularly useful spectroscopic tool. With the incorporation of fs and picosecond ps pulsed lasers into LIBS, signal to noise ratios have improved, as well as the reproducibility of laser induced sample damage [188-190]. Ablation of the sample surface is, however, unavoidable with LIBS as some material breakdown by the action of the incident laser pulse must occur in order to generate sufficient plasma emission for spectroscopic analysis.

The use of multiple laser pulses in LIBS was introduced in 1984, and was first demonstrated using nanosecond laser pulses [191]. Since that time, considerable effort has been devoted to studying variations on the dual-pulse theme, including using different combinations of fs and ns laser pulses [192], using a primary laser pulse to produce an air spark above the sample followed by a secondary ablative pulse [192-196], and different incident laser beam geometries including collinear (both laser pulses are incident along the same path) [197, 198] and orthogonal (pulses arrive perpendicular to each other at the sample surface, with pre-ablation spark [192-196] or post-ablation re-heating of the ablation plasma [192, 199]). The fruits of these efforts include much greater signal amplitude, better signal to noise ratios, and improved reproducibility. However, the physical mechanisms underlying observed benefits are only beginning to be understood [200-202].

The enhancement mechanisms for DP-LIBS in the orthogonal geometry will briefly be discussed as it relates to the techniques used in this dissertation. For pre-ablation spark DP-LIBS (not pursued in this dissertation), the air immediately above the sample surface is ionized by a tightly focused pre-pulse prior to the arrival of a second, ablating pulse [192-196]. The delay between the pre-pulse and ablating pulse can be varied, along with the position of the air ionization spark produced by the pre-pulse relative to the ablation event produced by the second pulse on the sample surface [196, 203]. The effect of the pre-ablation spark in the air may be to locally heat the sample surface (through absorption of light emitted by the air spark) which has been shown to increase the volume of ablation craters in metals [204] and dielectrics [183]. The increase in ablated material due to sample heating (by several hundred to several thousand degrees) would increase the temperature of the ablation plasma (by several thousand degrees [195]), thereby increasing the associated optical emission [201]. The heat produced by the pre-pulse air spark may also modify the optical properties of the surface, enhancing absorption of the ablating pulse laser energy [200]. Additionally, the air spark produced by the first pulse may locally decrease the local pressure and atomic number density [201], which has been shown to provide increases in plasma emission and ablation volumes [205, 206].

For orthogonal DP-LIBS in which the second pulse re-heats the ablation plasma produced by a primary pulse, the mechanism for signal enhancement is better understood [200]. The material ablating from the surface by the action of the first pulse (in the form of clusters and droplets submerged in a plasma of ions) is aggressively ionized by a time delayed second pulse or probe pulse arriving parallel to the sample surface [191]. In this fashion, the enhancement comes from reheating the ablation plume with the second laser pulse [200]. In the work presented in this dissertation, DP-LIBS is used to minimize the ablation or damage produced on the sample surface as a result of this spectroscopy technique using the orthogonal beam geometry, with a time delayed re-heating or probe pulse to further ionize material ablated from the surface by a near threshold pump pulse.

2.3.3 Simulations of fs laser ablation

In this thesis a simulation of the fs laser ablation event was peformed using FLASH hydrodynamic code in collaboration with Mousumi Das (post-doctoral appointee, Department of Materials Science and Engineering, University of Michigan) and Katsuyo Thornton (Assistant Professor of Materials Science and

Engineering, University of Michigan). The FLASH code was developed at the University of Chicago and is a modular, parallel, and open-source code that employs a piecewise-parabolic-method based solver [207] for Eulerian hydrodynamics equations for compressible flow problems found in many astrophysical events. A block-structured adaptive-mesh-refinement (AMR) scheme known as PARAMESH [208, 209], is used within FLASH to subdivide the computational domain into a collection of hierarchically organized blocks. The initial conditions for 2D FLASH simulation were obtained from a 1D radiation-hydrodynamics simulation performed with the HYADES code, which treats the laser-material interaction [210, 211].

Other computational methods have been used to simulate fs laser ablation of metals, including other hydrodynamic simulations [212] and molecular dynamics (MD) simulations [38, 45, 168, 213-217]. From these works a great deal has been learned about the mechanisms for material removal during fs laser ablation and the resulting shock wave launched into the bulk material from the ablation event. Hydrodynamics simulations demonstrate the significance of the laser-induced pressure gradients on the ablation process, with pressures exceeding 3×10^{11} Pa within the first 500 fs after the arrival of the laser pulse for a laser fluence of 5 J/cm^2 directed onto an Al sample [212]. Due to particularly strong axial pressure gradients (perpendicular to the sample surface) the ablating material initially expands largely vertical to the sample surface (1D expansion) [212], consistent with the observations made in side-view pump-probe imaging experiments discussed in this dissertation (see Chapter 5.2) and elsewhere [72].

MD simulations provide a physical picture of the ablation process, albeit usually for relatively modest material volumes due to the exponential increase in calculation time required for large scale simulations. Many MD simulations have focused on the fs laser ablation dynamics in metals as a function of laser fluence [168, 213, 214, 216, 217]. Three-dimensional MD simulation of fs laser ablation of Fe indicated that for laser fluence just less than the ablation threshold, desorption of single particles from the surface can occur [214]. Two-dimensional simulations presented in [168] indicated four different mechanisms for ablation at laser fluences above the ablation threshold but below the threshold for plasma formation. Spallation of material was observed to occur for laser fluences very near the ablation threshold (~ 1.0 F_{Th}), in which a tensile wave propagates into the bulk and induces fractures parallel to the surface leading to the ejection of liquid density layer of material [38, 168]. This is consistent with the model for ablation inferred from front-view imaging of near threshold fs laser ablation of metals showing the presence of the Newton's rings interference phenomenon [34, 35].

For yet higher laser fluences (~ 1.2 F_{Th}) homogeneous nucleation of voids within the superheated liquid was observed in MD simulations, which results in a sudden transition from a fluid to a mixture of vapor and liquid drops which ablate away from the material [168] in a process referred to as phase explosion [44, 218] or more accurately homogeneous boiling [37]. As the laser fluence is increased further it is suggested that an ablation process dominated by fragmentation develops in which the initially homogeneous super-critical fluid decomposes into clusters that are ejected with the ablation event [168]. Finally, for very high laser fluences the MD simulation shows complete atomization of the surface layer of the material which then expands at very high speeds [168]. In other studies, MD simulations of fs laser ablation of Al reveal that the ablation plume is comprised of fast moving, atoms and ions (ejected on the time scale of 1 – 10 ps with the ions emitted first, followed by the neutrals [213]), followed by the ejection of heavy nanoparticulates with an order of magnitude smaller velocity [216].

Simulations have also been performed to identify the role of the laser pulse duration on the ablation dynamics [45, 215]. MD simulations of fs laser ablation of thin Cu films 30 monolayers thick (5.2 nm) showed that reduction of the pulse duration from 10 ps to 100 fs produced a dramatic increase in the magnitude of the compressive and tensile components of the pressure within the material [45]. Furthermore, for a fixed laser fluence, the time required to melt the Cu film increased linearly with the laser pulse duration [45]. In studies of fs laser ablation of Al and Ni, the increase in laser pulse duration was found to increase thermal losses due to greater electron diffusion (which reduces the electron density), which in turn reduces the maximum temperature reached in the material [215]. Furthermore, ablation plumes produced with 5 ps pulses possessed larger clusters of atoms than ablation plumes accompanying sub-picosecond laser irradiation at the same laser fluence [215].

These simulation efforts expose many critical features of fs laser ablation, including mechanisms for material removal and associated effects on the remaining bulk material. The complexity of the MD simulations discussed above limit their application to small sample volumes (typically less than 1 μm^3) and to relatively brief time periods after the onset of ablation (typically 10's of picoseconds). The simulation efforts presented in this dissertation introduce the use of the FLASH simulation code [219] to fs laser ablation (it has been applied to nanosecond laser ablation [220]). With similar computation times to those used in MD simulations, the FLASH code is capable of treating larger simulation volumes, while simulating the ablation event over ns timescales. Excellent agreement between 2D FLASH simulations and side-view images of fs laser ablation of the Ni-based superalloy CMSX-4 demonstrate the value of the FLASH code (see Chapter 5.2.3). What the FLASH code may lack is the ability to predict the effect of the ablation event on the remaining bulk material, which fortunately can be treated with the 1D HYADES code.

In summary, the dynamics of fs laser ablation of a variety of materials have been observed with pump-probe imaging techniques and time-resolved DP-LIBS, and simulated with molecular dynamics and hydrodynamic codes. In-situ observations using pump-probe imaging techniques have revealed critical details of fs laser ablation, including near threshold ablation mechanisms. Time-resolved DP-LIBS techniques have increased signal amplitudes and sensitivity of LIBS. Finally, simulation efforts have improved understanding of dynamics of ablation on the picosecond timescale and atomic length scale, revealing phenomena correlated with observations of evolving fs laser ablation morphology with increasing laser fluence. For the first time, results from different observation techniques have been combined to provide a detailed picture of fs laser ablation.

Chapter 3

Experimental Details

3.0 Experimental Details

In this section, the details of experimental setups and procedures are provided for investigations of fs laser ablation thresholds, ablation morphologies, and ablation dynamics. Additionally, there is a section devoted to the commercially available fs pulsed laser used for all experiments (Chapter 3.1). Details on the samples used for these experiments; Si(100) with native oxide (SiO_2), as well as thermally grown oxide (SiO_2) films and plasma enhanced chemical vapor deposited (PECVD) oxide (SiO_2) films, and the Ni-based superalloy CMSX-4, are provided at the start of sections detailing the ablation threshold experiments (Chapters 3.4.1, 3.4.2, and 3.4.3). The techniques for ablation threshold measurement, pump-probe imaging, and the dual-pulse laser induced breakdown spectroscopy were applied to both silicon with oxide films and the Ni-based superalloy CMSX-4, however separate sections are presented which address the specifics of each investigation.

3.1 The femtosecond laser

All laser ablation experiments discussed in this dissertation were performed with a commercially available, chirped-pulse amplified (CPA), Ti:sapphire femtosecond (fs) laser from Clark-MXR (model CPA-2001). Information on the technique of chirped pulse amplification is available from multiple sources [10, 11]. The laser produces a beam with a Gaussian spatial intensity profile, and with a $sech^2$ temporal profile with full width half maximum (FWHM) of 150 fs, at a central wavelength of 780 nm. The laser pulses are produced at a repetition rate

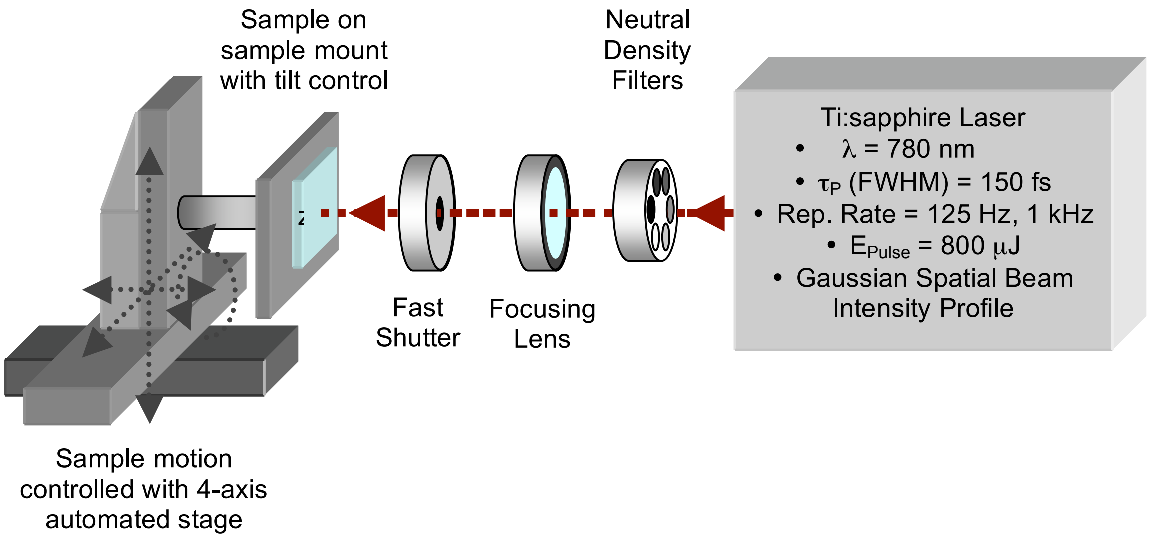

Figure 3.3.1 General experimental setup for fs pulsed laser ablation threshold measurement. Laser pulses are incident from right. Neutral density filters are used to control the intensity of the incident beam. The laser beam is focused onto the sample surface with a focusing lens. The type of lens (focal length, and plano-convex, bi-convex, or achromatic) used for particular experiment are indicated for each experiment. For certain experiments, a fast acting shutter was used to select single pulses from train of pulses in the laser beam. The sample is placed on a mount with tilt control, while an automated 4-axis (3 translation, 1 rotation) motorized stage translated the sample in the focal plane.

of 125 Hz or 1 kHz depending on the requirements of particular experiments. The laser produced pulses with a maximum energy of around 800 μJ, corresponding to a peak power (peak power = peak pulse energy divided by FWHM temporal pulse width) in excess of 5 GW. The reported RMS variation on energy pulse-to-pulse is 1%, however the average power output from the laser was observed to fluctuate (greater than 1 %) on particularly humid days (> 60 % relative humidity). To avoid additional experimental error the laser was not used on humid days (> 50 % relative humidity).

3.2 Definition of fs pulsed laser ablation and ablation threshold

In this dissertation, ablation is defined as fs laser induced removal of material from the surface of sample that is observed using optical microscopy (OM), scanning electron microscopy (SEM), or atomic force microscopy (AFM). The ablation threshold is defined as the minimum laser fluence (fluence = laser pulse energy per unit area defined by the $1/e^2$ beam radius) that is required to remove material from the surface of a particular sample.

3.3 Measurement of the fs pulsed laser single shot ablation threshold

In general, the ablation threshold is measured by generating ablation features (typically circular or elliptical craters) on a sample surface over a range of decreasing laser pulse energies until ablation to the sample surface is no longer produced. A typical experimental setup for ablation threshold experiments is shown in Figure 2.3.1. The radius of the ablation features as a function of the pulse energy are then measured ex-situ, and a fitting routine based on the Gaussian spatial intensity profile of the fs laser beam is used to determine the ablation threshold and Gaussian beam radius. The ablation threshold values are given here in terms of peak laser fluence (laser pulse energy per unit area). In some works the average fluence (1/2 of the peak fluence) of a pulse required to cause ablation is cited as the ablation threshold.

In practice, multiple ablation features were produced at the same incident laser pulse energy (with all other laser conditions constant) to average out shot-to-shot fluctuations of the laser (< 1% rms). Identical conditions imply the same laser pulse energy, and consistent beam delivery to the sample surface. The laser pulse energy is the average power of the laser beam measured immediately prior to the focusing lens with an Ophir Optics power meter (detector head model 3A-P), divided by the repetition rate of the laser (either 125 Hz or 1 kHz). With all other experimental conditions constant, multiple sets of ablation features were produced with decreasing pulses energies. The pulse energy was controlled with neutral density filters. Ideally ablation features produced with at least 10 different pulse energies were generated in order to provide more accurate results. It was difficult to obtain ablation features with several different pulse energies for ablation threshold experiments performed in ultra high vacuum (Chapter 4.1) due to limited sample area and difficulties in sample positioning. Measurements of ablation threshold made in UHV exhibit greater error due to the limited acquisition of data.

Naturally, features produced with laser fluences the ablation threshold are of particular interest when making an ablation threshold measurement. In order to

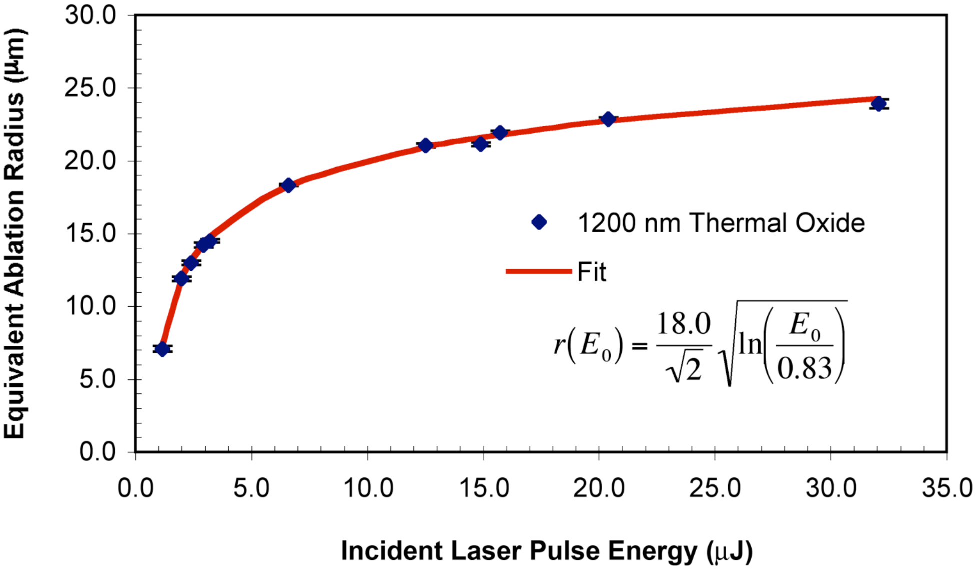

Figure 3.3.2 Measured equivalent ablation radius determined from area of ablation features as a function of fs laser pulse energy produced on Si(100) with 1200 nm thermal oxide (SiO_2) at normal incidence. Each data point represents the average equivalent ablation radius of 8 features, while the error is the standard deviation of these 8 measurements. The fit to the measured data yields a Gaussian beam waist, w_0 = 18.0 ± 0.2 μm, with an energy threshold E_{th} = 0.83 ± 0.2 μJ, yielding an ablation threshold of F_{th} = 0.17 ± 0.01 J/cm^2.

assure that features were produced in this important regime, the ablation plasma or visible spark at the sample surface accompanying the laser ablation event was monitored by eye during the experiment (with safety glasses on). Once the pulse energy was decreased to where the ablation plasma was no longer visible, features were produced with 4 or 5 more pulse energies below the threshold for plasma formation [15] to assure that features were produced in the important near threshold regime.

Following production of the ablation features, images of the ablation features produced for each laser energy were collected ex-situ via OM or SEM (details of which are provided in Chapter 3.5). The radius of the fs laser ablation features r_{abl} as a function of the laser pulse energy E_{pulse} was then measured from these images using Adobe Photoshop software. In some case the area of the ablated surface area was measured using an image threshold routine within ImageJ software from the National Institute of Health. If the area of the ablation feature was measured, an equivalent ablation radius $r_{abl,eq}$ was determined via $r_{abl,eq} = (\text{Area}/\pi)^{1/2}$.

The ablation threshold was then obtained by performing a least-squares fitting routine on the measured ablation radius (or equivalent ablation radius) as a function of the incident pulse energy. Figure 3.3.2 provides an example plot of the equivalent ablation radius (determined from area of ablation feature) as a function of the incident laser pulse energy. The equation used to fit the data is based on the Gaussian spatial intensity of the beam. The laser fluence of a Gaussian beam as a function of *r*, the radius outward from the center of the focused beam is given by:

$$F(r) = F_0 e^{-2\left(r/w_0 \right)^2} \tag{3.3.1}$$

Where w_0 is the focused beam waist, and F_0 is the peak laser fluence given by:

$$F_0 = \frac{2E_{pulse}}{\pi w_0^2} \tag{3.3.2}$$

where E_{pulse} is the energy of the laser pulse. Considering a particular feature, the ablation local laser fluence at the edge of the ablation feature (i.e. at the location r_{abl} (or $r_{abl,eq}$)) is given by:

$$F_{Th} = F(r_d) = F_0 e^{-2\left(r_d/w_0 \right)^2} \tag{3.3.3}$$

Equation (3.3.3) can be rearranged to yield the ablation radius as a function of the incident laser fluence, the ablation threshold laser fluence, and the focused beam waist:

$$r_{abl} = \frac{w_0}{\sqrt{2}} \sqrt{\ln\left(\frac{F_0}{F_{Th}} \right)} = \frac{w_0}{\sqrt{2}} \sqrt{\ln\left(\frac{E_{pulse}}{E_{Th}} \right)} \tag{3.3.4}$$

where we have replaced F_0 with Equation (3.3.2) above, and we have used:

$$F_{Th} = \frac{2E_{Th}}{\pi w_0^2} \tag{3.3.5}$$

Using E_{Th} and w_0 as fitting parameters, Equation (3.3.4) was used to fit (with Origin version 6.0 software) the measured ablation radius as a function of the incident laser pulse energy (see Figure 3.3.2). With E_{Th} and w_0 from the fitting routine [221], the ablation threshold was calculated from Equation (3.3.5). For non-normal laser incidence, Equation (3.3.5) for the ablation threshold is modified to include the incident laser angle θ_s with respect to the sample surface:

$$F_{Th} = \frac{2E_{Th}}{\pi w_0^2}\sin(\theta_s) \qquad (3.3.6)$$

Furthermore, at normal incidence the focused beam shape was often elliptical (as opposed to circular) at the sample surface resulting in elliptical ablation features. In this case, the minor axis *b* of ablation features was measured to determine the ablation threshold, and the fitting routine returns the Gaussian beam minor axis b_0 (so that $w_0 = b_0$ in Equation 3.3.4). A correction factor *c* was then introduced into Equation 3.3.5 by taking the average ratio of the lengths of the major to minor axis (b_i/a_i) of the ellipse for several ablation features produced over the range laser pulse energies used in the experiment. Noting that the area of an ellipse with major axis a_1 and minor axis b_1 is given $\pi a_1 b_1$, and that $c = \langle a_i/b_i \rangle$, This yields the following expression for an ablation threshold corrected for an elliptical spot:

$$F_{Th} = \frac{2E_{Th}}{\pi c_1 c b_0^2} \qquad (3.3.7)$$

If the area of the ablation features was measured (using the image threshold routine), the elliptical nature of the ablation features was neglected and the fitting routine returned the geometric average of the major and minor axial Gaussian beam waists of the focused laser beam.

Finally, if the area of the ablation features are measured for ablation threshold determination for non-normal incidence laser irradiation, the equivalent ablation radius is obtained from the measured ablation area by $r_{abl,eq} = (\text{Area}*\sin(\theta_s)/\pi)^{1/2}$, where θ_s is the angle of incidence of the laser beam with respect to the sample surface.

3.4 Femtosecond laser ablation studies in ultra high vacuum

To determine the influence of the native oxide of silicon on fs laser ablation, experiments were carried out in an ultra high vacuum (UHV) chamber where the

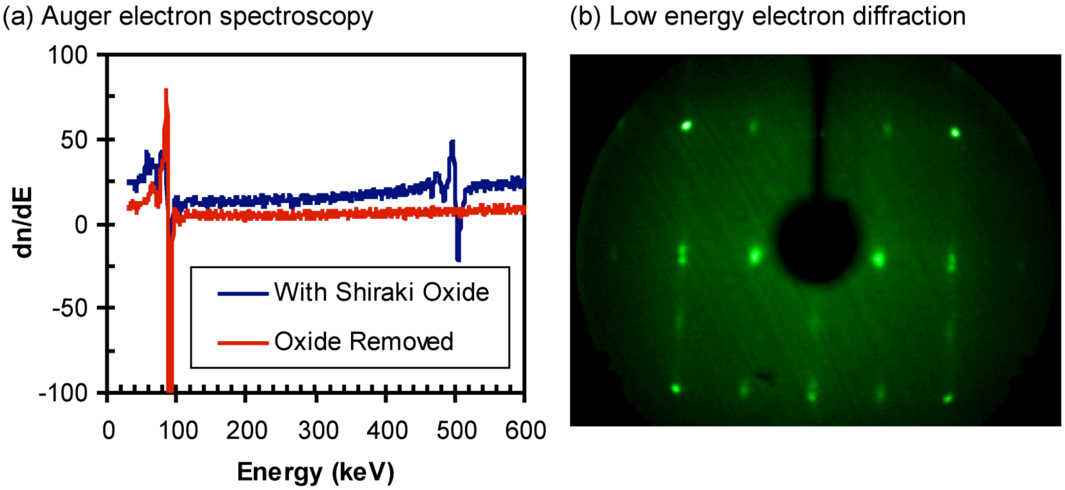
(a) Auger electron spectroscopy

(b) Low energy electron diffraction

Figure 3.4.1 a) Auger electron spectroscopy of Si(100) with and without Shiraki oxide showing peaks from silicon (LMM at 86 keV)) and oxygen (KLL at 513 keV). No peak is present for oxygen once the Shiraki oxide was removed with outgassing. Also notice the absence of carbon contamination (KLL 272 kEV). b) Low energy electron diffraction (at electron energy of 60 eV) of atomically clean silicon surface showing the (2×1)+(1×2) surface reconstruction. The double spot in the LEED diffraction pattern may be due to the extreme temperatures reached during removal of the Shiraki oxide.

presence or absence of the native oxide could be controlled with conventional wet-chemistry techniques. For multiple and single shot fs laser ablation studies, samples with native oxide were prepared with an initial degreasing scrub (Triton ™ solution), followed by acetone, methanol and deionized water baths. For multiple shot ablation morphology studies, the native oxide was etched from atomically clean samples with a buffered HF acid solution prior to insertion into the UHV chamber. The resulting surface hydride was removed by heating samples to 900 °C [222, 223].

For single shot ablation threshold studies, sample preparation of atomically clean Si (100) included a full Shiraki cleaning procedure [224]. This technique yields a pristine Si (100) surface with a protective silicon dioxide film free of carbon contamination. Once samples were transferred to the UHV chamber they were outgassed with the following procedure: 50 mA for 15 min., 100 mA for 15 min., 200 mA for 30 min. and 400 mA for at least 2 hours. The protective oxide layer placed at the surface during the Shiraki cleaning procedure was finally removed by heating the sample surface to ~ 950 ºC for 20 sec. immediately prior

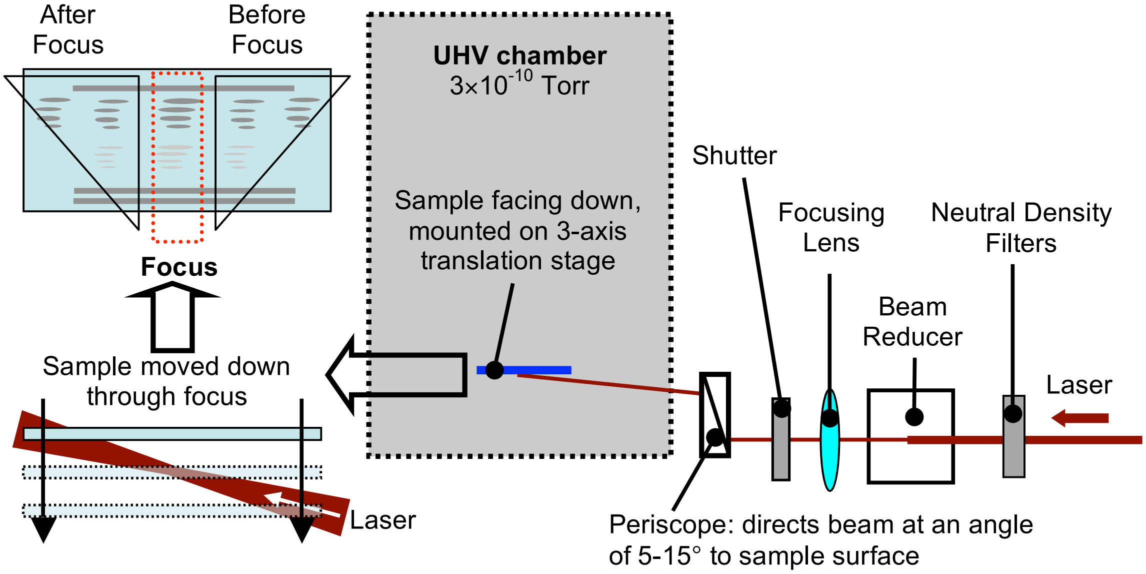

Figure 3.4.2 Experimental setup for beam delivery into ultra high vacuum chamber for ablation threshold and morphology studies. Schematic at left shows the effect of the grazing incidence geometry. The sample is scanning vertically through the focused beam, producing ablation features before focus, at focus, and after focus. Only features produced at focus were analyzed.

to laser machining. Surface sensitive Auger electron spectroscopy (AES) was used verify the absence of oxygen at the silicon surface. Furthermore, low energy electron diffraction (LEED) patterns revealed that the Si surface was crystalline with the familiar (2 × 1) + (1 × 2) surface reconstruction (see Figure 3.4.1). When the native oxide was present on the silicon surface, no LEED pattern was produced.

A schematic illustrating laser beam delivery into the UHV chamber is presented in Figure 3.4.2. For all experiments performed in UHV, the laser beam was *p*-polarized with respect to the sample surface, and directed onto the samples at grazing incidence (75-85° with respect to the sample normal), yielding elliptical ablation features. The focused beam had a waist of ~ 60 ± 5 μm ($1/e^2$) (determined from Equation (A1.2) and verified with the fitting routine for ablation threshold) yielding a typical elliptical ablation features with area at focus of around 10^{-4} cm^2. The error in the calculated beam waist reflects the error in the measured beam diameter (± 500 μm) prior to focusing. The laser intensity was controlled with neutral density filters, while the number of laser pulses used to produce a particular feature was controlled with a fast acting shutter (Uniblitz) with appropriate delays generated with a digital delay generator (Model DG535, from Stanford Research Systems).

For single shot fs laser ablation threshold studies, samples with and without the native oxide were laser machined during the same session to minimize changes due to slight variations in day-to-day laser output power and beam alignment relative to the sample in the UHV chamber. Ablation threshold data were collected for two beam incident angles relative to the sample normal, 83.2º and 80.5º. The ablation threshold was calculated following the steps detailed in Chapter 3.3. The diameter of a single-shot ablation feature was defined to be the width of the ablation feature apparent in a 1000X SEM image. SEM images of ablation on Si(100) with native oxide were found to exhibit greater contrast than images collected with OM. The radius of the ablation feature was measured along the short axis of the elliptical features.

3.5 Femtosecond laser ablation threshold studies in air

The experimental setup used for fs laser ablation threshold studies in air is presented in Figure 3.3.1. For normal incidence, samples were positioned at the focus of the laser beam following the technique presented in Appendix 1. Single shot features were obtained for normal incidence ablation threshold studies by translating the sample through the focused laser beam at a constant velocity (typically 12.5 mm/s). For non-normal incidence studies the sample surface was tilted with respect to the incident laser beam and single and multiple shot features were obtained by controlling the laser exposure with a fast acting shutter (Uniblitz). Furthermore, samples were translated through the focused beam such that features were produced before, after, and at the location of focus with respect to the focusing lens (in the same fashion presented in Figure 3.4.2). Only features produced at the laser focus were measured to determine the ablation threshold. The incident laser beam was polarized parallel to the plane of the optics table. To effectively change the polarization of the incident laser beam with respect to the sample surface, the sample was rotated by 90° about the axis of the incident beam. Other more elegant means of rotating the laser polarization are available (such as use of a half-wave plate [225]), but were not used in this study.

3.5.1 Ablation threshold of silicon with native oxide in air

Si (100) samples with native oxide were prepared by cleaning the surface with a detergent (Triton ™ solution), then rinsed sequentially in DI water, acetone, methanol, and an additional deionized water bath. The ablation threshold was studied as a function of the laser beam polarization with respect to the sample surface. The laser was incident on the sample at approximately 75° relative to the sample normal to take advantage of the greatest difference in intensity reflection of the silicon substrate between the two polarizations (see Figure A2.4). A discussion of the reflectivity of a crystalline silicon surface with a surface oxide thin film, including the effect of multiple reflections for thicker films is presented in Appendix 2. The laser was focused onto the sample with a 35 cm focal length plano-convex lens, producing a nearly circular spot at focus with a diameter of ~ 70 ± 5 μm (spot size at focus determined by fitting data with Equation 3.3.4).

3.5.2 Ablation threshold of silicon with thermally grown oxide films

The ablation threshold of Si(100) wafers was studied as a function of the thickness of thermally grown oxide films on the surface of the wafers. The Si(100) wafers with thermal oxide films were obtained from the Michigan Nanofabrication Facility (MNF). A Si(100) wafer with native oxide was also used for ablation threshold experiments at normal laser incidence. The thickness' of the thermal oxide films were found via ellipsometry to be 19.5 nm, 54 nm, 147 nm, 300 nm, and 1200 nm, while the thickness of the native oxide was determined (also by ellipsometry) to be 2.3 ± 0.3 nm. Prior to exposure to the laser, samples were prepared by an initial Triton degreasing scrub, followed by acetone, methanol, and deionized water baths.

The ablation threshold was determined for both normal laser incidence, and non-normal laser incidence with the beam incident at 48.7 ± 1.0° with respect to the sample surface. The laser was focused onto the sample with a 20 cm focal length plano-covex lens, producing a nearly circular spot at focus with a diameter of ~ 36 ± 2 μm (spot size focus determined by fitting routine, see Chapter 3.3)

3.5.3 Ablation threshold of CMSX-4 Ni-based superalloy

The CMSX-4 superalloy samples used for fs laser ablation studies were 15 × 15 × 4 mm blocks cut from the single crystal bar. The CMSX-4 superalloy composition in weight percent is: 61.42% Ni, 9.6% Co, 6.6% Ta, 6.4% Cr, 6.4% W, 5.64% Al, 2.9% Re, 1.03% Ti, and 0.1% Hf. Further details of sample heat treatment and microscructure provided elsewhere [116]. In general, sample surfaces were prepared for laser experiments by conventional metallographic procedures with a final polish of 0.05 μm Al_2O_3 suspension. Immediately prior to experimentation, the sample surface was cleaned with methanol. The fs laser ablation threshold was determined at normal incidence with the laser focused with a 5 cm achromatic lens yielding a focused beam diameter of 8.9 ± 0.2 μm (determined from fitting routine, see Chapter 3.3). The ablation features were characterized with OM to determine the ablation threshold, and the depth of ablation features was characterized with AFM to determine the depth of ablation craters as a function of the incident laser pulse energy as described below. Due to the elliptical nature of the ablation features, the major and minor axes of the features were measured and the geometric average of these was used as the equivalent ablation radius determining the ablation threshold.

The depth of single pulse fs laser ablation craters as a function incident laser fluence was determined for the Ni-based superalloy CMSX-4. With the laser operating at a repetition rate of 1 kHz, ablation features were produced at normal incidence, with the laser focused with a 5 cm focal length achromatic lens (as described above for the ablation threshold measurement). The sample was moved at a velocity of 40 mm/s yielding a separation of 40 μm between features. Two rows of ablation features were made for each laser fluence, with the rows separated by 100 μm for high laser fluence, and 50 μm for lower laser fluence to facilitate measurement of multiple features with one AFM scan. A range of incident laser fluence was used to produce the ablation features (0.5 – 26.2 J/cm^2). For each laser fluence the ablation depth of 6 features were measured and averaged.

3.6 Characterization of femtosecond laser induced ablation morphology

The surface morphology accompanying fs laser induced material breakdown was studied with scanning electron microscopy (SEM), atomic force microscopy (AFM), and optical microscopy (OM). Occasionally OM with the addition of a Nomarski prism was used for enhanced contrast. In many cases, images collected for ablation threshold measurements were also used for qualitative characterization of ablation morphology. Quantitative analysis of ablation morphology, including the ablation depth as a function of laser pulse energy (Chapter 4.3), the dimensions of fs laser induced blisters in thermal oxide thin films (Chapter 5.2, Chapter 6.1), and the ablated surface roughness (Chapter 5.2) was performed with AFM.

3.6.1 Scanning electron microscopy

SEM images were collected of fs laser induced ablation using instruments in both the L. H. Van Vlack undergraduate laboratory (Phillips model XL30) and in the Electron Microbeam Analysis Laboratory (EMAL) (Phillips model XL30 FEG, FEI model Quanta 3D FIB, and FEI model Nova 200 Nanolab FIB). For chemical characterization within the SEM, X-ray Energy Dispersive spectroscopy (XEDS) was also performed (EDAX/Gatan). Samples which required conductive coatings to facilitate imaging were sputter coated with Au/Pd at EMAL (SPI-Module sputter coater). To assure that appropriate comparisons could be made between samples, care was taken to use consistent electron beam conditions such as beam spot size and accelerating voltage during SEM image collection. Where appropriate, such as with XEDS analysis, the accelerating voltage and beam spot size are indicated.

3.6.2 Optical Microscopy

Two particular optical microscopes were used for collecting images of fs laser induced ablation for both ablation threshold and ablation morphology studies. Optical microscope images were collected at the L. H. Van Vlack Undergraduate Laboratory using Nikon Optiphot microscopes with Nikon Digital Sight cameras (camera models DS-L, DS-5m) and also within the laboratory of Dr. David Martin using a Nikon Optiphot2 microscope with an attached Diagnostic Instruments color digital camera (camera model Spot 2.2.1). The microscopes at the L. H. Van Vlack Undergraduate Laboratory had additional Nomarski prisms which could be inserted to provide greater image contrast. The Nomarski prism is one technique for obtaining differential interference contrast [226, 227], and was found to be very useful for imaging subtle ablation morphologies. Throughout the dissertation images collected with the addition of the Nomarski prism will be indicated with Nomarski-OM.

3.6.3 Atomic force microscopy

Atomic force microscopy (AFM) was performed on select samples to obtain a topographic representation of the fs laser induced ablation morphology. Quantitative characterization of ablation morphology, including the ablation depth as a function of laser pulse energy (Chapter 5.1, and 5.2), the dimensions of fs laser induced blisters in thermal oxide thin films (Chapter 5.2, Chapter 6.1), and the ablated surface roughness (Chapter 5.2) was performed with AFM.

A Digital Instruments model Nanoscope IIIa AFM located in EMAL was used in both contact mode and tapping mode, however tapping mode was found to provide the greatest ease in obtaining quality images. The tips used for tapping mode AFM were UltraSharp Silicon Cantilevers type NSC15/AlBS/15obtained from online from www.spmtips.com. It should be noted that the maximum height variation measurable by Nanoscope IIIa AFM was 6.26 μm, so that ablation morphologies with variations in height exceeding this limit were not be measured via AFM. For optimal AFM imaging, scan rates less than 1 Hz were used (as low as 0.2 Hz for rough surfaces with μm height features on a μm lateral scale) with corresponding scan velocities less than or equal to 50 μm/s. Feedback

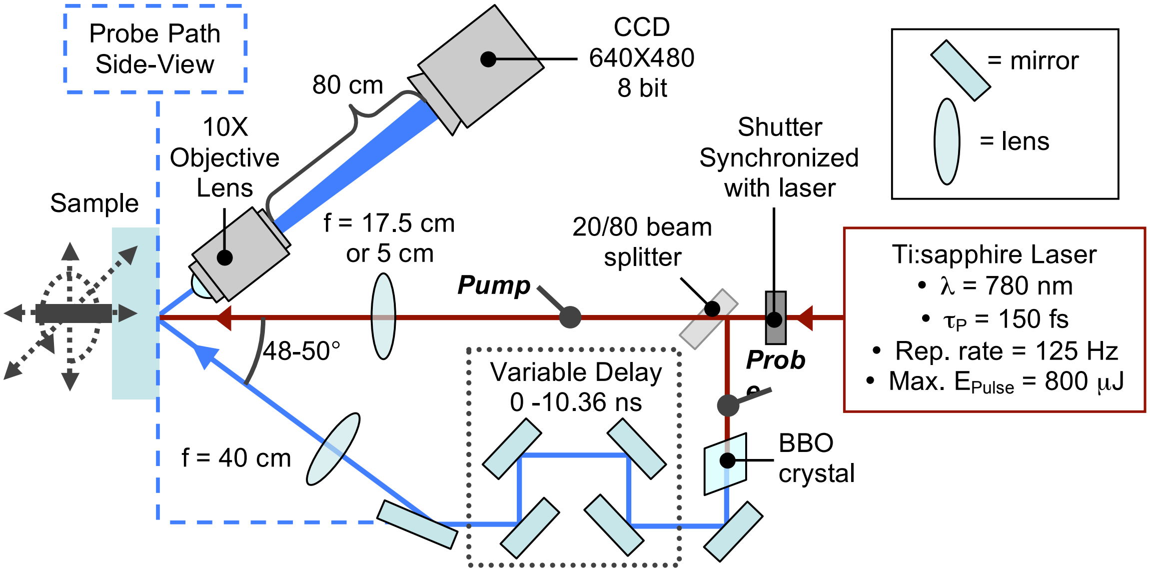

Figure 3.7.1 Experimental setup for pump-probe imaging of fs laser ablation. Laser pulses were incident from the Ti:sapphire laser at the right. A 20/80 beam splitter directs 20% of the incident beam to the pump beam with the remaining 80% directed to the probe beam. A β-BBO crystal was used to frequency double the probe (so that λ = 390 nm), and the relative delay between the arrival of the pump and the probe at the sample was controlled with a four-pass variable delay (mirrors mounted on manual translation rail). The probe path for side-view imaging is represented by the dashed line. Sample is mounted on a tilt adjustable mount which is connected to a 4 axis automated, motorized stage.

parameters found to produce images with minimal scan lines (where the AFM tip temporarily looses contact with the surface) included integral gains of around 0.3 and proportional gains of around 0.6, set point voltages of less than 1.0 V, and amplitude set point voltages of around 600 mV.

3.7 Pump-probe techniques for studying the dynamics of single pulse fs laser ablation

The dynamics of single pulse fs laser ablation of silicon with oxide films and the Ni-based superalloy CMSX-4 were studied in-situ with pump-probe imaging techniques [56, 77]. Additional insight into the dynamics of material removal was obtained with orthogonal dual-pulse laser induced breakdown spectroscopy (LIBS) [57]. The experimental details of these techniques are described in the following sections.

3.7.1 Pump-probe imaging of single pulse fs laser ablation

In-situ pump-probe images of fs laser ablation were obtained from two different viewing angles; front-view images were produced with probe light reflected off surface region of a sample undergoing fs laser ablation [34, 35], while side-view images (or shadowgraphs) were formed with probe light that had passed laterally through the fs laser ablation event [41, 65, 72, 166]. Front and side-view images were obtained of the fs laser ablation of Si(100) with native oxide and thermally grown oxide films, while only side-view imaging was pursued to study the fs laser ablation dynamics of the CMSX-4 superalloy. Several experimental details were common to both materials, however details specific to each will be indicated throughout.

The experimental setup for both front and side view imaging is presented in Figure 3.7.1. A fast acting shutter was used to isolate single laser pulses. A “single shot” circuit prepared by Pascal Rousseau, (Research Engineer, Center for Ultrafast Optical Science, the University of Michigan) was used to synchronize the shutter with the output of the laser, assuring that the laser pulses would not be clipped during the ~ 1 ms opening/closing time of the shutter. Not indicated in Figure 3.7.1 is a beam reducing telescope which served to reduce the incident laser beam diameter by a factor two, allowing the beam to fit through the small aperture of the fast acting shutter (5 mm diameter). This telescope was comprised of a 20 cm focal length, plano-convex lens which was placed 10 cm in front of (relative to the incident beam) of a -10 cm focal length, plano-concave lens. Immediately after the laser shutter, the incident beam was split into two beams with an 80/20 beam splitter. The pump path (λ = 780 nm) received 20% of the available laser power, and was directed onto the sample surface at normal incidence, generating the ablation event that was subsequently probed with the probe pulse.

For silicon with oxide films, the pump beam was focused onto the sample surface with a 17.5 cm focal length plano-convex lens, yielding a focused beam diameter of 70 ± 5 μm (determined from ablation threshold fitting routine, see Chapter 3.3). Given these focusing conditions, the fs laser ablation dynamics resulting from pump laser fluences of 4.6 J/cm^2, 2.6 J/cm^2, and 1.3 J/cm^2 were studied.

For the CMSX-4 superalloy, the pump beam was focused onto the sample surface with a 5 cm focal length plano-convex lens, yielding a focused beam diameter of 19 ± 2 μm. Ablation resulting from pump laser fluences of 62.8 J/cm^2, 30.4 J/cm^2, 20.4 J/cm^2, 10.1 J/cm^2, 4.9 J/cm^2, 3.92 J/cm^2, 2.7 J/cm^2 and 1.23 J/cm^2 were studied.

For both the silicon and CMSX-4 superalloy studies, the probe path (λ = 390 nm) received the remaining 80% of the available laser power and was subsequently frequency doubled (using a 0.5 mm thick β-barium borate crystal) to enable probe light to be distinguished from that of the pump. The time delay between the pump and probe pulses was controlled with a four-pass manual delay line, allowing for images to be collected with the probe pulse up to 10.36 ns (± 0.05 ns) after the ablation was initiated by the pump pulse. The image exposure time in each case was dictated by the 150 fs temporal pulse width produced by the laser. The probe beam was weakly focused with a 40 cm focal length, plano-convex lens. The probe fluence was continually adjusted for optimal imaging, and did not exceed 0.1 J/cm^2 at the sample surface. For *front* view imaging (Si(100) with oxide films only), the probe was directed onto the sample surface at 50°± 2° relative to the sample normal, and an image was formed with the probe pulse reflected from the sample surface irradiated with the pump pulse (similar to traditional reflection mode OM). It should be noted that for each collected image at a new time delay, the sample position was changed so that the pump-pulse encountered a virgin surface. As many as 50 images were collected at various time delays For a particular experimental run. In order to reduce jitter from image to image, the tilt of the sample surface with respect to the incident pump beam was carefully adjust by retro-reflecting the un-focused pump beam back along the pump-beam path.

For *side* view imaging (both Si(100) with oxide films and CMSX-4 superalloy), the probe was directed parallel to the sample surface (90°± 0.2° to sample normal) and a shadowgraph of the ablation event was produced (see Chapter

2.4.1 for background information). In both the front and side view cases, the probe light was collected with a 10x microscope objective and directed onto a CCD camera (640×480, 8 bit) positioned ~80 cm from the back of the objective. The four-pass optical delay line was again used to delay the arrival of probe pulse with respect to the pump. As for front-view images, the sample was translated for each image so that the pump-pulse encountered a virgin sample surface for each image and time delay. The tilt from the sample was also carefully adjusted so that the position of the sample edge was consistent from image to image.

3.7.2 Single and dual-pulse laser induced breakdown spectroscopy

Laser induced breakdown spectroscopy (LIBS) is a surface chemistry characterization technique which utilizes the optical emission produced by the plasma (or spark) accompanying laser induced material breakdown to perform spectroscopy (see Chapter 2.4.2 for background information). Some amount of material removal or surface damage is inherent to the LIBS technique. As discussed in the introduction and background section, the primary goal of this study was to determining the minimum amount of laser induced surface ablation required to perform the LIBS technique. To this end a time-resolved, dual-pulse, pump-probe LIBS technique [192-196] was employed which greatly reduced surface damage while also providing insight into the dynamics of the fs laser ablation.

The fundamental principle of DP-LIBS technique is to use a time-delayed probe-pulse to aggressively ionized material ablated from a sample surface with a low energy pump-pulse. The technique was initially applied to Si(100) with native oxide in preparation for later application to the Ni-based superalloy CMSX-4. The experimental details of the DP-LIBS technique are presented in the following, with details specific to the study of each material indicated where appropriate.

The experimental setup for DP-LIBS is very similar to that used for side-view imaging of fs laser ablation discussed in Chapter 3.7.1 above, as shown in Figure

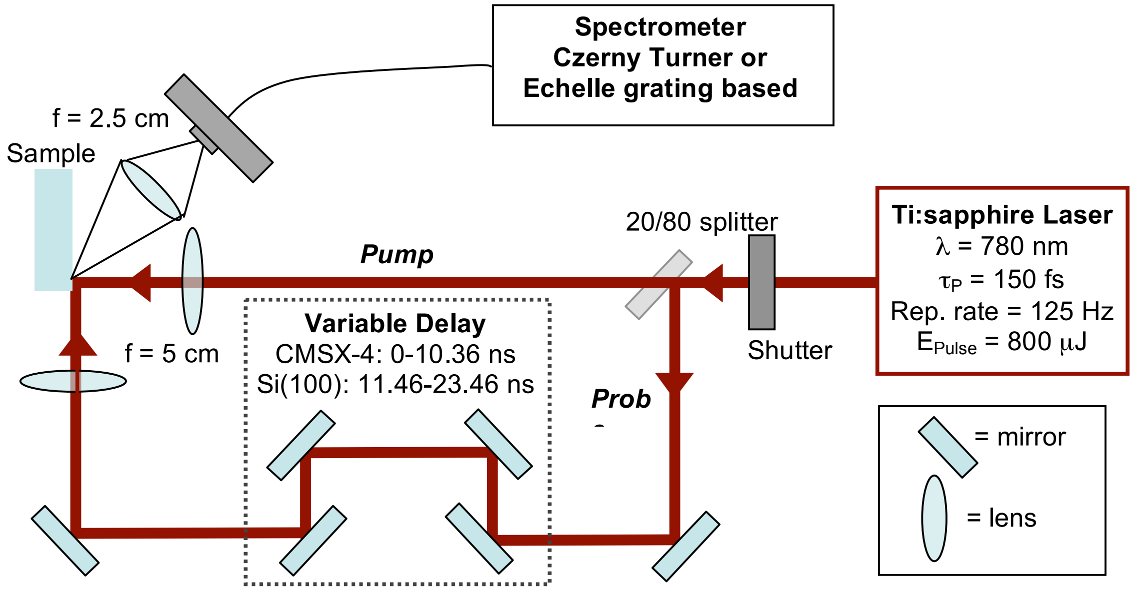

Figure 3.7.2 Experimental setup for single and DP-LIBS experiments. Laser pulses were incident from the right. A 20/80 beam splitter directs 20% of the incident beam to the pump beam with the remaining 80% directed to the probe beam. The relative delay between the arrival of the pump and the probe at the sample was controlled with a four-pass variable delay (mirrors mounted on manual translation rail). Sample is mounted on a tilt adjustable mount which is connected to a 4 axis automated, motorized stage. Optical emission from laser ablation plasma collected with 2.5 cm achromatic lens and focused onto a fiber optic cable which carried the light to the spectrometer. The fiber head and collection lens were mounted on a 3 axis manual translation stage. Details on the fiber cable and spectrometer/CCD used for each experiment are provided in Chapter 3.7.2.

3.7.2. Briefly, a beam reducing telescope was used to reduce the incident beam diameter by a factor of 2, which was followed by a fast acting shutter synchronized with the output of the laser to isolate single shots from the laser pulse train delivered at 125 Hz from the Ti:sapphire, fs pulsed laser described in Chapter 3.1. An 80/20 beam splitter followed the shutter and was used separate the laser beam into the pump (20%) and probe (80%) beams. For both samples, the pump beam was focused onto the sample surface at normal incidence with a 5 cm focal length, plano-convex lens yielding a focal spot diameter ($1/e^2$) of approximately 20 μm. The energy of the pump pulse was controlled with neutral density filters. The sample position was controlled with a 3 axis motorized stage, and samples were mounted on an adjustable-tilt mount which was adjusted for flatness with respect to the probe beam which arrived parallel to the sample surface. This flatness was typically 5 μm over 20 mm.

The probe beam traversed a four-pass adjustable delay that allowed for the probe to be delayed with respect to the arrival of pump pulse at the sample surface. Note that the probe-pulse was not frequency doubled for DP-LIBS as it was for pump-probe imaging experiments. For experiments with Si(100) with native oxide, a static delay line totaling 11.5 ns was inserted into the probe beam path, such that the pump-probe delay range used during DP-LIBS collection ranged from 11.5 – 23.5 ns (± 0.05 ns). The necessity of the additional delay leg is related to the velocity of material ablating from the Si(100) surface. For experiments with the Ni-based CMSX-4 superalloy, the additional static delay leg was not used, and the four-pass delay provided adjustable delays ranging from -0.31 – 10.36 ns (± 0.05 ns) between the arrival of the pump and probe pulses at the sample surface.

The probe beam was carefully focused parallel to the sample surface with a 5 cm focal length achromatic lens, yielding a focused probe beam diameter ($1/e^2$) of approximately 20 µm. It must be emphasized that the probe laser fluence was fixed for all experiments (46 J/cm^2 for experiments with Si(100), 270 J/cm^2 for experiments with the Ni-based superalloy). On the other hand, the fluence of the pump-pulse was adjusted to provide the minimal damage to the sample surface. The probe pulse arrived parallel to the sample surface (orthogonal to the pump-pulse), and was placed at a desired height above the sample such that it did not damage the sample surface when it was exposed without the pump pulse. To accurately determine the height of the probe pulse above the sample, single shots from the probe beam were directed toward the sample, and a height was determined at which the probe pulse just skimmed the sample surface. This height, termed z_{skim} was determined by finding the sample position at which a very small ablation spark was produced by the probe pulse on the edge of the sample (viewed with a CCD camera). The sample was then translated the specified distance or height away from the probe beam, typically 30 μm, with an accuracy of around ± 5 μm.

For LIBS experiments performed on Si(100) with native oxide, the emission of light from the plasma resulting from the ablation of sample material was collected by producing an image of the ablation event on the tip of a 500 μm fiber with a 2.5 cm achromatic doublet lens. The fiber then carried the collected light to a Czerny-Turner type spectrometer (EG&G Instruments, Applied Research), with a grating groove density of 600 groves per mm, and with a liquid cooled CCD detector. Collection of spectra was optically triggered by scattered light from the laser pulse upon passing through the shutter, and the emission collection was gated to 100 μs beginning immediately upon triggering. For the Si(100) samples the spectral feature monitored for all experiments was located at a characteristic wavelength of 390.874 nm (corresponding to singly ionized silicon), with the total spectral range collected between 351.112 – 428.888 nm. The characteristic wavelength for the Si (I) feature is located 390.5523 nm [228], which suggests that the spectrometer grating was slightly misaligned. For each pump-probe setting (pump fluence and pump-probe time delay), 19 individual spectra were collected and averaged to obtain an overall signal amplitude and standard deviation of the signal at 390.874 nm.

For Si(100) with native oxide, samples were diced from a single Si(100) wafer. Both single and DP-LIBS experiments were performed on Si(100). For single pulse LIBS, pump laser fluences ranging from 1.7 J/cm^2, 2.6 J/cm^2, 3.4 J/cm^2, 4.4 J/cm^2, 5.4 J/cm^2, 7.4 J/cm^2, 8.9 J/cm^2, and 9.3 J/cm^2 were used with the aim of determining the lowest single pulse laser fluence for which signal could be observed at a specific characteristic wavelength of Si (390.874 nm) in the LIBS spectrum.. DP-LIBS spectra were collected at a probe height of 30 μm (± 5 μm) with pump laser fluences of 0.7 J/cm^2, 1.3 J/cm^2, and 1.7 J/cm^2 while the pump-probe delay was scanned over the delay range from 11.46 – 23.46 ns (± 0.05 ns).

For LIBS experiments on the Ni-based superalloy CMSX-4, the emission of light from the plasma resulting from the ablation of sample material was collected with a 2.5 cm achromatic doublet lens, producing an image of the luminous ablation plasma on the tip of a 100 μm diameter fiber optic cable. The fiber then carried the collected light to an Echelle-type spectrometer with a liquid cooled, gated CCD camera (Mechelle 5000 Spectrograph with iStar CCD camera from

Andor Technology). Collection of spectra was synchronized with the output of the laser (with the single shot circuit from Pascal Rousseau), with collection beginning approximately 40 ns after the arrival of the pump pulse at the sample surface. The 40 ns delay was used to avoid bleaching the CCD camera with scattered laser light. The gate width for spectra collection was 800 ns (2 ns resolution), and the emission for 10 laser shots each incident on virgin, new sample surface regions were integrated to yield the raw LIBS signal for each data point. No background subtraction was performed, and the data were not otherwise manipulated.

Both single pulse LIBS and DP-LIBS experiments were performed on the CMSX-4 superalloy. The composition of the Ni-based CMSX-4 superalloy is provided above in Chapter 3.4.3. The characteristic wavelengths for the major constituents in the LIBS spectra examined were located at: 352.454 nm for Ni, 425.435 nm for Cr, 394.4006 nm and 396.152 nm for Al [228]. Signal was observed in the LIBS spectra for the minor constituents as well, with the exception of Hf which was not identified. This may have been because the characteristic wavelengths for Hf were located near significant peaks from other elements. For single-pulse experiments, the probe beam was simply blocked and LIBS spectra were collected at pump laser fluences of 59.4 J/cm^2, 37.5 J/cm^2, 28.8 J/cm^2, 23.1 J/cm^2, 20.0 J/cm^2, 12.7 J/cm^2, 7.9 J/cm^2, and 6.1 J/cm^2 with the aim of determining the lowest single pulse laser fluence for which signal could be observed at the characteristic wavelengths of Ni, Al, and Cr in the LIBS spectrum.

Two specific DP-LIBS experiments were performed for the Ni-based superalloy CMSX-4. First, while maintaining a constant pump-probe delay (10.36 ns), probe beam height above the sample surface (30 ± 5 μm), and probe beam laser fluence (270 J/cm^2), the laser fluence of the pump pulse was gradually reduced to determine the minimum pump laser fluence for which the addition of the orthogonal arriving probe pulse produced measurable signal at the characteristic wavelengths of Ni, Al, and Cr. In this fashion, the DP-LIBS threshold was determined. The probe pulse was s-polarized with respect to the sample surface for all DP-LIBS experiments performed on the Ni-based superalloy CMSX-4.

Time-resolved DP-LIBS experiments were also performed for pump laser fluences of 10.1 J/cm^2, 5.2 J/cm^2, and 3.1 J/cm^2. This was done by maintaining a probe height (30 ± 5 μm) and probe fluence (270 J/cm^2), while scanning the relative delay between the pump and probe pulses in 0.67 ns increments from 0 to 10.36 ns following arrival of the pump pulse at the sample surface. In this fashion, the time delay at which the LIBS signal emerged at the characteristic wavelength of Al (394.42425 nm) in the measured LIBS spectrum was considered to be time required for the ablated material to traverse the distance between the sample and the probe pulse (located at a height of 30 ± 5 μm above the sample surface). This allowed for an additional measure of the ablated material velocity, as the probe height was known and the pump-probe delay at which the signal emerged for DP-LIBS was determined. The results of these experiments are discussed in Chapter 6.2.2.

3.7.3 Details of FLASH and HYADES simulation codes

A multidimensional hydrodynamics code, FLASH was used to simulate single pulse fs laser ablation of the Ni-based superalloy CMSX-4. These simulations were compared with side-view shadowgraphic images of the single pulse fs laser ablation event. As discussed in the introduction (see Chapter 1.4.3), the FLASH code is modular, parallel and open-source code that has a piecewise-parabolic-method based solver [207] for Eulerian hydrodynamics equations for the compressible flow problems found in many astrophysical events. The code employs a PARAMESH [208, 209] a block-structured adaptive-mesh-refinement (AMR) scheme for subdividing the computational domain into a collection of hierarchically organized blocks.

The ideal gas equation of state (EOS) module within FLASH was used for material evolution, which has a specific heat ratio, $\gamma = 5/3$. However, the material fluid is typically described as a polytropic gas, such that the value of γ should be reduced compared to its value under ideal-gas conditions [229]. FLASH simulations with γ values smaller ranging from $1.4 \leq \gamma \leq 5/3$ were performed, and it was observed for $\gamma \leq 1.4$ the evolution of the ablated material became unstable and less comparable to side-view shadowgraphic images. The simulated images in 2D FLASH simulation were comprised of 56×56 unrefined zones with maximum refinement level of 7 for the AMR scheme.

The initial conditions for the 2D FLASH simulations were obtained from a series of 1D HYADES simulation performed across a strip of material (3.5 μm by 20 μm slab). HYADES is a radiation-hydrodynamics code, that incorporates laser-material interaction [211] to obtain the initial temperature and density distributions within the material following absorption of the laser energy. Only the area of the sample that showed significant temperature variations from the HYADES simulation after 1ps was used as input to 2D FLASH simulation (thus the 3.5μm-thick by 20μm-wide slab). The selection of this sample geometry (as opposed to a semi-infinite plane of material) reduced the effects of unphysical material expansion within the FLASH simulations that was observed for material far outside of the volume initially energized by the laser pulse. This unphysical expansion was attributed to the lack of a material strength model within the FLASH code. Due to the one-dimensional nature of the HYADES code, the slab of material was taken in 0.5 μm slices in width, extending the full depth of the sample (3.5 μm) such that 40 such slices were taken across the 20 μm slab. The HYADES simulations were allowed to run for 1 ps, and the temperature and density of the 1D lines (separated by 0.5 μm) were combined yielding the initial conditions input into the 2D FLASH simulations. The results of these simulations are presented in Chapter 6.2.3.

Chapter 4

Femtosecond laser ablation thresholds

4.1 Ablation threshold of Si(100) with and without native oxide

The single pulse fs laser induced ablation threshold of Si(100) was studied to determine if the naturally occurring native oxide (1.5 – 3 nm thick) of silicon had any measurable effect on the ablation threshold. A review of previous ablation threshold measurements performed on silicon is provided in Chapter 2.2.4. Rarely is the presence of the native oxide mentioned with respect to ablation threshold measurement [52, 118]. Furthermore, other studies have not explored non-normal laser incidence or the dependence of the ablation threshold on the linear polarization of the laser beam, where the influence of the native oxide can be clearly demonstrated.

The experimental details of this investigation are presented Chapter 3.4 (for experiments in ultra high vacuum) and Chapter 3.5 (for experiments in air), while general details of the ablation threshold measurement are provided in Chapter 3.3. Briefly, single-pulse fs laser ablation threshold experiments were performed with samples in ultra high vacuum (UHV) where the presence or absence of the native oxide was controlled with the Shiraki cleaning method and sample outgassing. Second, single pulse fs laser ablation threshold experiments were performed in air, where the threshold dependence on the incident laser pulse polarization was considered in order to further identify the significance of the native oxide of silicon on the ablation threshold. The results of these demonstrate the significance of the native oxide of silicon, demonstrating that to first order the variations in the measured ablation threshold can be attributed to the change in the optical properties of a silicon surface in the presence of a thin oxide film.

4.1.1 Ablation threshold of Si(100) with and without native oxide in UHV.

To first order, we expect the fs laser ablation threshold of a material will increase if the reflectivity of the surface increases. This assumption is based on the rationale that when the surface reflectivity is high, less light from the laser pulse is transmitted into the bulk material to participate in carrier excitation and eventually the ablation of material. As such, presence or absence of the native oxide layer on a crystalline silicon substrate will affect the measured ablation threshold of the crystalline silicon by changing the reflective properties of the substrate. With this in mind, the ablation threshold will be discussed in the context of the Fresnel intensity reflection coefficient [230, 231].

Discussion and calculation of the intensity reflection from and transmission into a Si(100) surface with an oxide film are presented in Appendix 2. The Fresnel reflection coefficient as a function of incident angle relative to the sample normal for *s*- and *p*-polarized light (λ_0 = 780 nm) arriving at the Si(100) surface with and without the oxide is shown in Figure A2.4. The plot in Figure A2.4 neglects the effect of multiple reflections within the oxide film (which is included for thicker films, Figure A2.2), and the extinction of light within the silicon. For laser beam incidence exceeding ~55º, the presence of the oxide film increases the reflectivity of the Si(100) for p-polarized radiation relative to a surface without the oxide. Specifically, at an angle of incidence of 80.5º, the reflectivity of Si(100) with the oxide for p-polarized light is ~33%, such that 67% of the light is transmitted into the silicon substrate and can participate in the ablation process. If the oxide is absent, the reflectivity of the Si(100) surface drops to 5%, such that ~95% of the incident light is transmitted into the material can participate in the ablation process. Thus we would expect that removing the native oxide film from the silicon will result lead to a decrease in the measured ablation threshold.

Following the above argument, a first order estimate of the relative ablation threshold for silicon with and with the native oxide can be obtained by the relative Fresnel intensity transmission coefficients, $T_{\text{AtomicallyClean}}$, and $T_{\text{Native Oxide}}$:

$$\text{Relative Damage Threshold} = \frac{F_{Th,NativeOxide}}{F_{Th,AtomicallyClean}} = \frac{T_{AtomicallyClean}}{T_{NativeOxide}} \qquad (4.1.1)$$

For p-polarized radiation delivered at an angle of incidence of 80.5° with respect to the sample normal, Equation (3.1.1) indicates that the measured single-shot ablation threshold may be 0.95/0.67 = 1.42 times greater for samples with a native oxide. This is of course dependent on whether the thin oxide behaves optically as assumed when generating the Fresnel coefficients (i.e. the thin native oxide film has a refractive index of 1.4537 at a wavelength of 780 nm, see Appendix 2). Note that for the Fresnel intensity reflection and transmission coefficients are related by $T = 1 - R$, where we assume that no absorption occurs within the oxide film.

The measured ablation threshold at an angle of incidence of 80.5º of the Si (100) with native oxide was 0.75 ± 0.05 J/cm^2, while the ablation threshold of the atomically clean Si(100) was 0.54 ± 0.07 Jcm^2, yielding a ratio of 1.39 ± 0.31. This ratio compares favorably with the first order approximation from the Fresnel intensity transmission coefficients made in the paragraph above (from Equation 4.1.1, the calculated relative threshold is ~1.42). The measured ablation radius vs. incident laser pulse energy for both samples is provided in Figure 4.1.1. It should be noted that due to the complicated beam delivery and limited control over sample position within into the UHV chamber, averaging of ablated feature radii produced at the same laser energy was not performed. However, the focused beam minor axis b_0 predicted by the fit was very comparable between samples (60.2 ± 2.1 μm for atomically clean Si(100), 61.9 ± 1.3 μm) providing a degree of confidence in the calculated ablation thresholds.

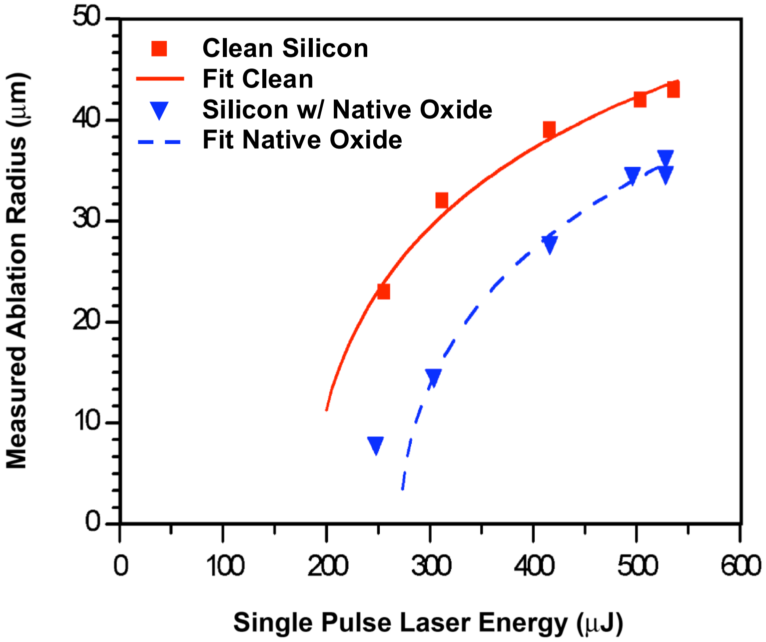

Figure 4.1.1 Results from fs laser ablation threshold experiments in UHV with p-polarized fs laser pulses incident at 80.5° with respect to the sample normal. Measured ablation radius vs. laser pulse energy for atomically clean Si(100) (red squares) with curve fitting (solid red line) yielding an ablation threshold of 0.54 ± 0.07 J/cm^2 and for Si(100) with a native oxide (blue triangles) with curve fitting (dotted blue line) yielding an ablation threshold of 0.75 ± 0.05 J/cm^2.

The results demonstrate that at grazing (80.5°), p-polarized laser incidence the native oxide increases the ablation threshold of Si(100) relative to atomically clean samples by increasing the optical reflectivity of the Si(100) surface. From Figure A2.4, it can be seen that at angles of laser incidence less than 55º, the presence of the native oxide *decreases* the reflectivity into the Si(100) surface for p-polarized light. This would suggest that the ablation threshold at normal incidence (0º), for example, would be greater for atomically clean Si(100) samples when compared with Si(100) with the native oxide. Due to difficulties in sample position manipulation within the UHV chamber, ablation threshold experiments at non-grazing angles of incidence were not performed, but should be considered for future work.

4.1.2 Ablation threshold of Si(100) with native oxide in air

In order to further address the role of native oxide on the ablation threshold of Si (100), the single-shot fs laser ablation thresholds of Si(100) with native oxide

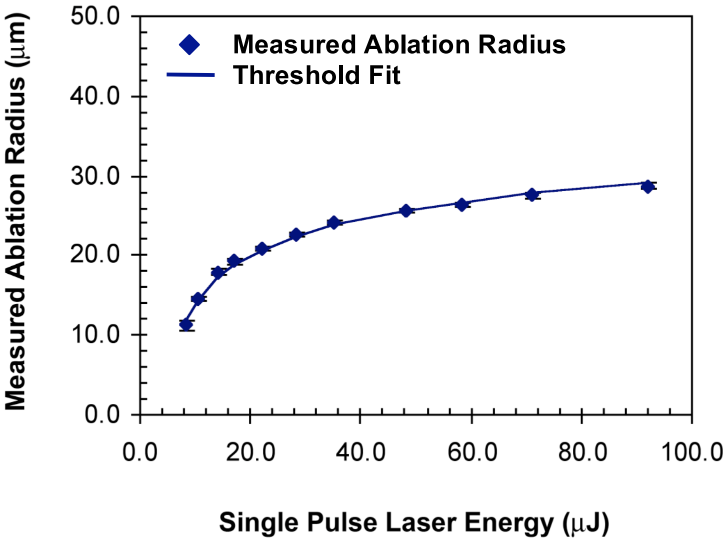

Figure 4.1.2 Results from fs laser ablation threshold experiment on Si(100) with native oxide in air at normal incidence. Measured ablation radius vs. laser pulse energy with curve fitting (solid blue line) yielding an ablation threshold of 0.38 ± 0.02 J/cm^2.

were next measured at grazing laser incidence as a function of the incident laser pulse polarization. The ablation threshold was also determined at normal laser incidence for comparison. These experiments were performed in air with Si (100) with the experimental setup shown in Figure 4.3.1. At grazing laser incidence, the laser polarization was controlled by simply rotating the samples by 90° about the axis of the incident laser beam.

The results of the normal incidence ablation threshold measurement are provided in Figure 4.1.2. Performing the fitting routine described in Chapter 3.3 to the measured ablated feature radius as a function of the incident laser pulse energy yielded an ablation threshold for Si(100) with native oxide at normal incidence of 0.38 ± 0.02 J/cm^2. Furthermore, the fitting routine returned a focused Gaussian beam spot size of 24.2 ± 0.3 μm (an elliptical beam correction ratio of c = 1.47 was used in the threshold calculation (see Equation 3.3.7)). This ablation threshold value compares well with other works, where the ablation threshold of Si(100) with native oxide at normal incidence is cited as 0.26-0.50 J/cm^2 [52].

Moving on to the grazing incidence ablation threshold measurements, more attention is given to the Fresnel intensity transmission and reflection coefficients.

Figure A2.4 demonstrates that regardless of the presence or absence of the oxide, more light is reflected from a crystalline silicon surface for s-polarized light than for p-polarized light for all angles of laser incidence. Thus we expect the ablation threshold to be greater for s-polarized light for all angles of laser incidence. However, Figure A2.4 also shows that the difference in the Fresnel intensity reflection coefficient between laser polarizations is much more significant if the Si(100) surface is atomically clean than if an oxide film is present. Given this discrepancy, we assessed the role of the native oxide by determining the ratio of the measured ablation thresholds for *s* and *p* polarized pulses and comparing the measured threshold ratio with what might be expected from the Fresnel intensity transmission coefficients in the presence or absence of the oxide film (using Equation 4.1.1).

Following the Fresnel intensity transmission coefficients at 75° laser incidence, if the surface behaves like atomically clean Si(100) (i.e. the oxide does not play a role) we expect a ratio of ~ 4.00 for the single-shot ablation threshold of *s*-polarized radiation relative to the single shot ablation threshold of *p*-polarized radiation (from Equation 4.1.1 above: $F_{s,\text{ at. clean}}/F_{p,\text{ at. clean}} = T_{p,\text{ at. clean}}/T_{s,\text{ at. clean}} = 1.00/0.25 = 4.00$). On the other hand, if the presence of the native oxide at the Si (100) surface does play a role in the ablation threshold, we expect a ratio of ~ 1.80 at an angle of incidence of 75° ($F_{s,\text{ oxide}}/F_{p,\text{ oxide}} = T_{p,\text{ oxide}}/T_{s,\text{ oxide}} = 0.79/0.44 = 1.80$).

At an angle of incidence of 75.3°, the fs laser ablation threshold for *p*-polarized radiation was determined to be 0.23 ± 0.01 J/cm^2, and at 74.3° the fs laser ablation threshold for *s*-polarized radiation was found to be 0.48 ± 0.04 J/cm^2. Furthermore, the ablation threshold fitting routine yielded a Gaussian beam radius of 34.5 ± 2.6 μm for the p-polarized beam, and 45.0 ± 1.2 μm for the s-polarized beam. The plots of the measured ablation radius as a function of the incident laser pulse energy along with the results of the ablation threshold fitting routine are shown in Figure 4.1.3. In this case, the spot sizes were different due to the elliptical nature of the laser beam. Note that the ratio of the spot sizes yields a correction factor c (in Equation 3.3.7) of ~ 1.3 ($c_s = 45.0/34.5$) for the s-

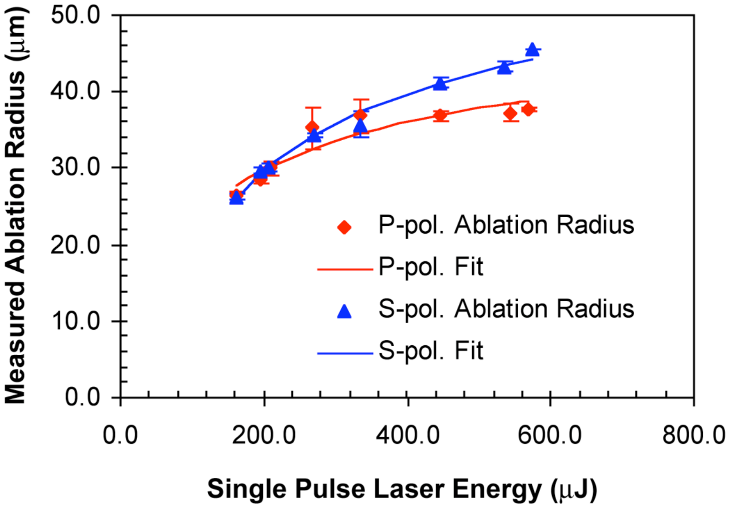

Figure 4.1.3 Fs laser single pulse ablation threshold of Si(100) with native oxide as a function of laser polarization in air with laser incident at ~75° with respect to the sample normal. a) Measured ablation radius vs. laser pulse energy for Si(100) with native oxide, where curve fitting yields an ablation threshold of 0.48 ± 0.04 J/cm^2. b) Measured ablation radius vs. laser pulse energy for atomically clean Si(100) with curve fitting yielding an ablation threshold of 0.23 ± 0.01 J/cm^2.

polarized beam, and ~ 0.77 (c_p = 34.5/45.0) for the p-polarized beam. The measured ablation threshold values yield an ablation threshold ratio of $F_{s,\ oxide}/F_{p,\ oxide}$ = 2.15 ± 0.28, which compares well with the first order approximation of 1.80 provided by the intensity transmission coefficient obtained with the presence of an oxide film on the surface of the Si(100) substrate.

The measured ablation threshold ratio may not precisely match those predicted the Fresnel intensity transmission coefficients due to the relatively simple manner in which the polarization of the incident laser beam was determined and controlled at the sample surface. More careful manipulation of the laser polarization with appropriate wave-plates may yield a more precise comparison. All the same, the observed polarization dependence of the ablation threshold further demonstrates that the thin native oxide of silicon influences the interaction of the fs laser pulse with the Si(100) surface.

In summary, fs laser ablation threshold measurements performed in air and in UHV reveal that the native oxide of Si(100) influences the optical interaction of fs laser pulses with the Si(100) surface. Fresnel's theory of reflection and transmission of polarized radiation at an interface was found to provide a good first order approximation of the relative ablation thresholds between Si(100) with and without the native oxide, and between incident linear laser polarizations at ~75° laser incidence. These results indicate that it is necessary to consider the influence of optical properties of naturally occurring surface oxides for ablation threshold experiments [52, 118]. The role of the native oxide on the resulting fs laser induced damage morphology is discussed later (see Chapter 5.1).

4.2 Ablation threshold of Si(100) with thermally grown oxide films

Following studies examining the role of the native oxide of silicon on the single pulse fs laser ablation threshold, similar threshold experiments were performed on silicon with thermally grown oxide (SiO_2) films. The details of these experiments are provided in Chapter 3.5.2. The single pulse, fs laser ablation threshold of the underlying silicon substrate was determined for oxide thicknesses including 20 nm, 54 nm, 147 nm, 300 nm, and 1200 nm thermally grown oxide films on Si(100) substrates. It must be emphasized the ablation threshold of the Si(100) substrate material was determined, and not the ablation threshold of the thin oxide films at the surface. Threshold studies were performed in air for both normal laser incidence and at ~45° laser incidence with respect to the surface normal using both s- and p-polarized laser pulses. The results of these studies are presented in the following section.

4.2.1 Ablation threshold of Si(100) with thermally grown oxide films at normal incidence

The equivalent single pulse, fs laser ablated feature radius as a function of the incident laser pulse energy for all thermal oxide thicknesses is provided in Figure 4.2.1(see Chapter 3.3 for details on the use of an equivalent ablation radius determined from the area of ablation features). The fs laser ablation threshold as a function of thermal oxide film thickness at normal laser incidence is presented in Figure 4.2.2. The ablation threshold was observed to oscillate with increasing film thickness, ranging from a minimum of 0.16 ± 0.01 J/cm^2 for a

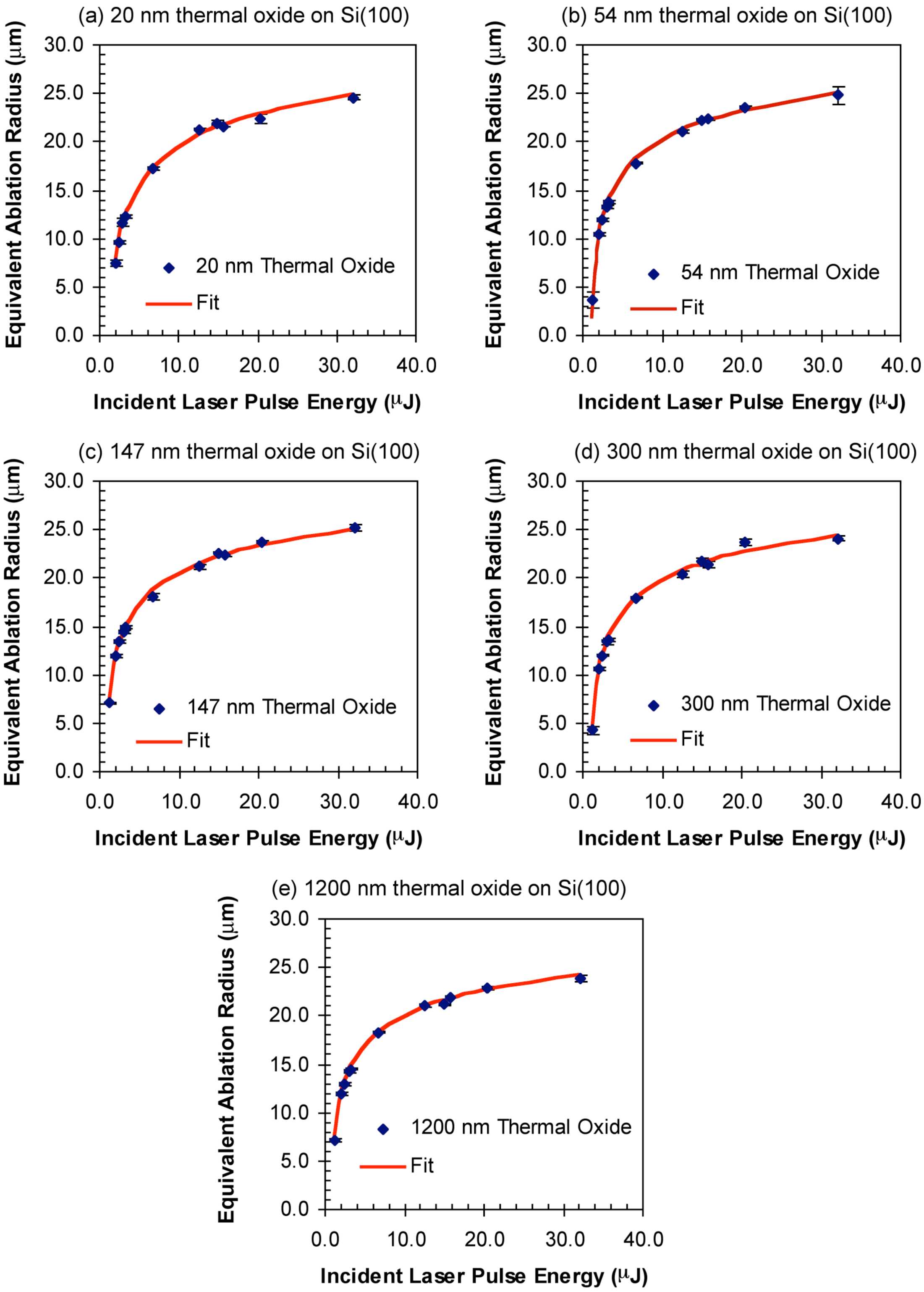

Figure 4.2.1 Results from single pulse fs laser ablation threshold experiments at normal laser incidence for Si(100) with thermally grown oxide films. Plots shows the measured ablation feature radius as a function of the incident laser pulse energy, along with fits to the data which yield the ablation threshold and Gaussian beam radius for Si(100) with thermal oxide films of thickness: a) 20 nm b) 54 nm c) 147 nm d) 300 nm e) 1200 nm

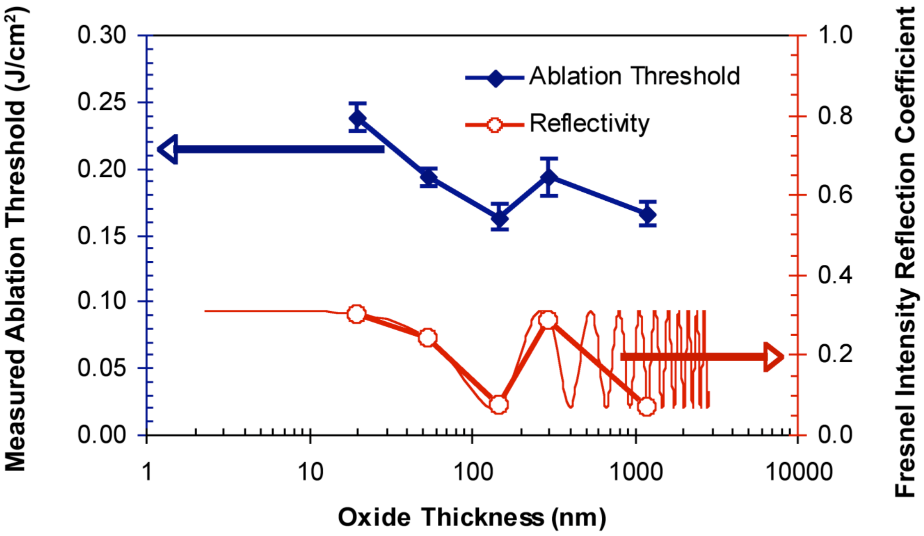

Figure 4.2.2 Measured single pulse fs laser ablation threshold and reflectivity of Si(100) as a function of thermal oxide film thickness.

sample with 147 nm of thermal oxide to a maximum of 0.24 ± 0.01 J/cm^2 for a sample with 20 nm of thermal oxide at the surface.

The variation of ablation threshold with oxide thickness was attributed to changes in the reflectivity of the Si(100) substrate as a function of oxide film thickness due to multiple reflections of the incident laser light within the oxide film. Depending on the thickness of the oxide film, these multiple reflections result in increasing or decreasing the net laser energy deposited into the underlying substrate through constructive or destructive interference of the reflected rays. The theory of multiple reflections is developed in Appendix 1.

The plot in Figure 4.2.2 shows the variation in the Fresnel intensity reflection coefficient of the Si(100) substrate as a function of the oxide film thickness.

Recall our assumption that to first order, when the reflectivity of a surface increases (with other conditions constant), the ablation threshold in terms of incident laser fluence increases as well. The trend in the measured ablation threshold follows the trend in the Fresnel intensity reflection coefficient with increasing oxide thickness (as shown in Figure 4.2.2). We conclude that the optical properties of the thermal oxide on silicon structure are largely responsible for the measured variation in ablation threshold as a function of oxide film thickness. This conclusion extends the results of the previous section (Chapter 4.1), where it was shown that the optical properties of the native oxide of silicon were sufficient to modify the ablation threshold. Subtle differences between the reflectivity and the ablation threshold may result from other phenomena, including quantum mechanical [232] or thermal effects [61]. These topics are not addressed here and should be considered for future work.

4.2.2 Ablation threshold of Si(100) with thermally grown oxide as a function of laser polarization and oxide film thickness films at ~ 42° laser incidence.

The ablation threshold was determined for Si(100) substrates with 20 nm, 54 nm, 147 nm, 300 nm, and 1200 nm thermally grown oxide films with the laser incidence at 41.8 ± 1° with respect to the sample normal for both s- and p-polarized laser pulses. The equivalent single pulse fs laser ablation radius as a function of the incident pulse energy is shown in Figure 4.2.3 for s-polarized radiation, and Figure 4.2.4 for p-polarized radiation. The single pulse fs laser ablation threshold for Si(100) as a function of thermally grown oxide film thickness and laser polarization is presented in Figure 4.2.5, where it is shown that the ablation threshold varies with oxide thickness for both s- and p-polarized laser pulses. As with the normal incidence ablation threshold, the measured ablation threshold largely followed the trend in reflectivity of the silicon substrate when multiple reflections in the oxide film were considered. It was noted however, that the ablation threshold of the 300 nm film did not increase as sharply relative to the 147 nm as expected from the Fresnel reflectivity coefficient for either laser polarization. This inconsistency is not understood, and additional characterization of the 300 nm thermal oxide film may clarify this discrepancy.

The relative ablation threshold as a function of the incident laser polarization ($F_{Th,\ s\text{-}pol}/F_{Th,\ p\text{-}pol}$) is presented in Figure 4.2.6, and compared with the relative Fresnel intensity transmission coefficient as a function of polarization (T_p/T_s following Equation 4.1.1). The results presented in Figure 4.2.6 support the argument presented in Chapter 4.1.1, where we propose that the relative ablation

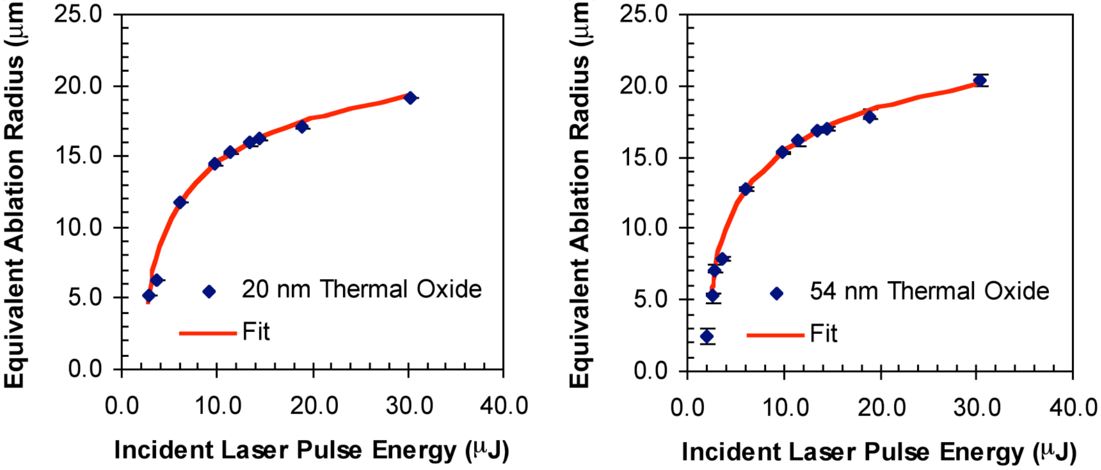

(a) 20 nm thermal oxide on Si(100)

(b) 54 nm thermal oxide on Si(100)

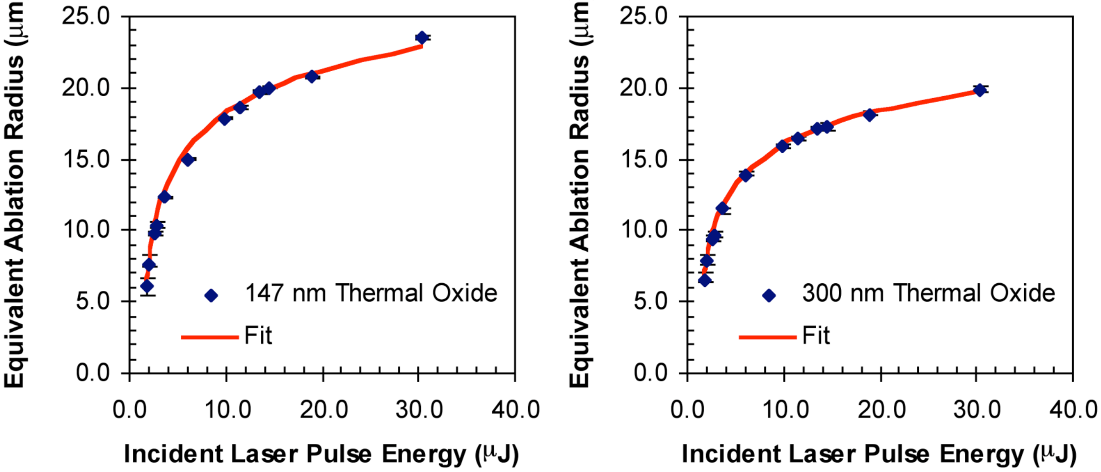

(c) 147 nm thermal oxide on Si(100)

(d) 300 nm thermal oxide on Si(100)

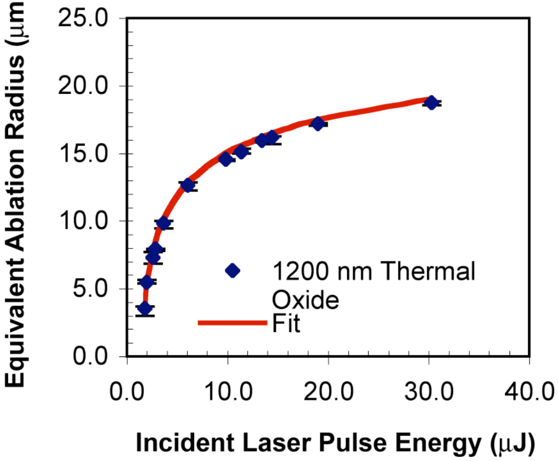

(e) 1200 nm thermal oxide on Si(100)

Figure 4.2.3 Results from single pulse fs laser ablation threshold experiments at 42.1° laser incidence with s-polarized laser pulses for Si(100) with thermally grown oxide films. Plots shows the measured ablation feature radius as a function of the incident laser pulse energy, along with fits to the data which yield the ablation threshold and Gaussian beam radius for Si(100) with thermal oxide films of thickness: a) 20 nm b) 54 nm c) 147 nm d) 300 nm e) 1200 nm.

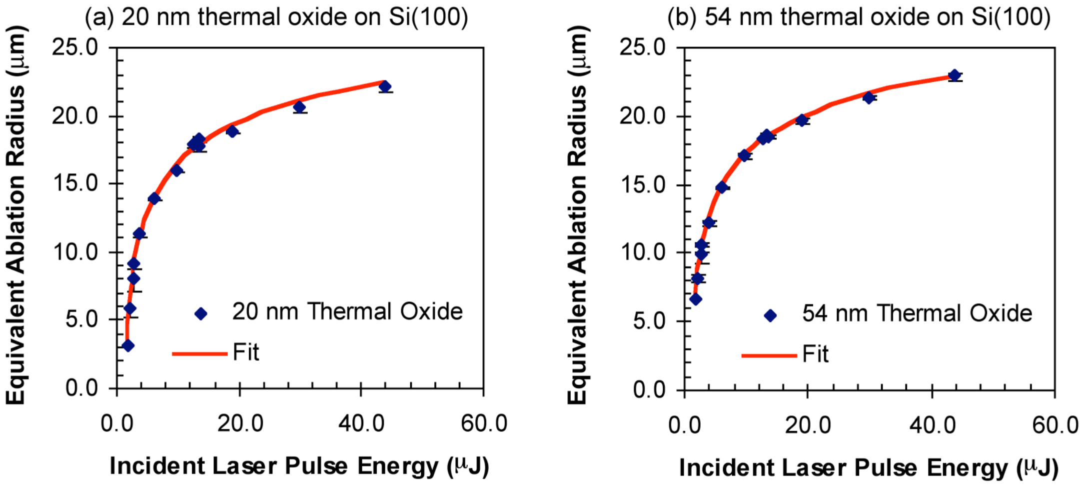
(a) 20 nm thermal oxide on Si(100)

(b) 54 nm thermal oxide on Si(100)

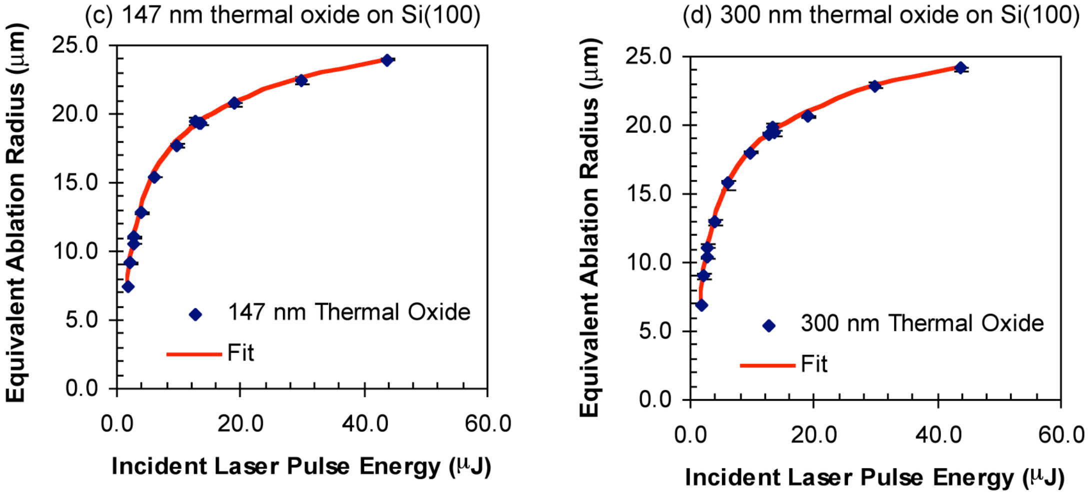
(c) 147 nm thermal oxide on Si(100)

(d) 300 nm thermal oxide on Si(100)

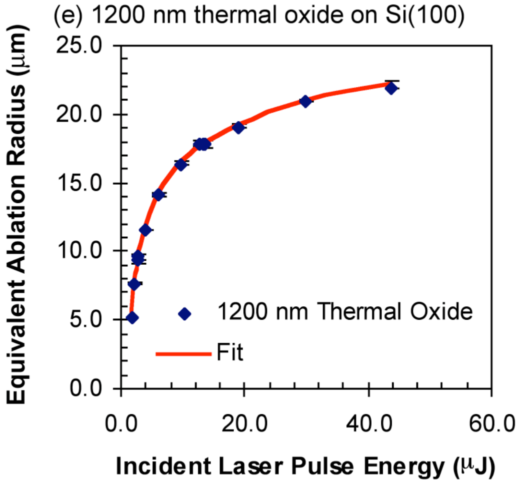
(e) 1200 nm thermal oxide on Si(100)

Figure 4.2.4 Results from single pulse fs laser ablation threshold experiments at 41.7° laser incidence with p-polarized laser pulses for Si(100) with thermally grown oxide films. Plots shows the measured ablation feature radius as a function of the incident laser pulse energy, along with fits to the data which yield the ablation threshold and Gaussian beam radius for Si(100) with thermal oxide films of thickness: a) 20 nm b) 54 nm c) 147 nm d) 300 nm e) 1200 nm.

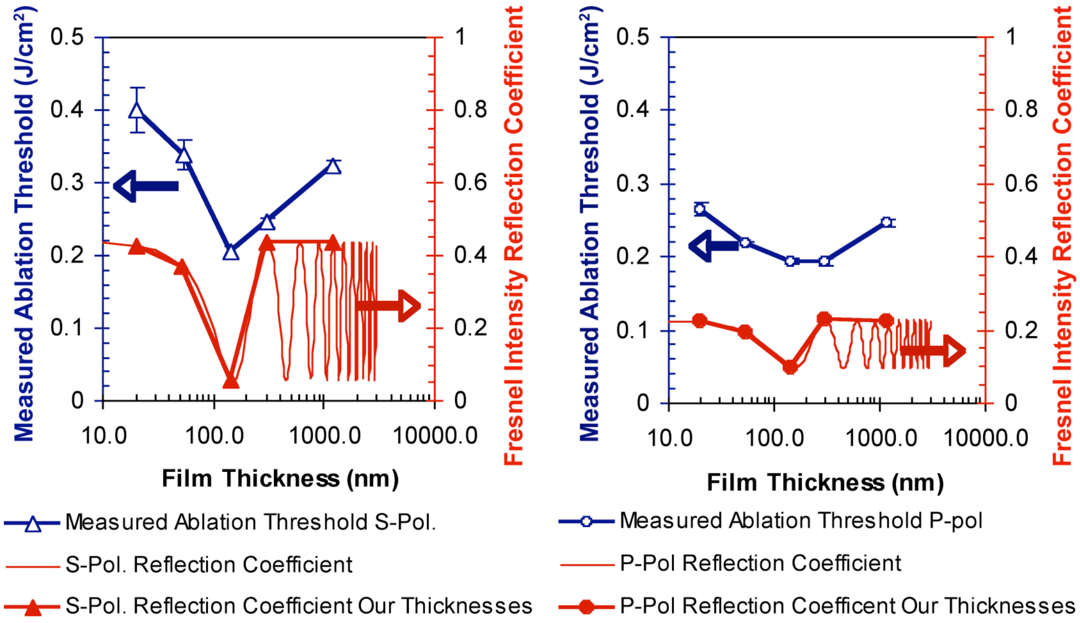

Figure 4.2.5 Measured single pulse fs laser ablation threshold and reflectivity of Si(100) as a function of thermal oxide film thickness and laser polarization.

threshold between two otherwise identical samples can be determined to first order from the relative Fresnel transmission coefficient of the surface of the ablating media (in this case the Si(100) substrate). The fact that the two curves presented in Figure 4.2.6 do not perfectly match may be the result of imperfect control of laser polarization at the sample surface. Other mechanisms may participate in fs laser ablation, including quantum mechanical effects of electrons excited by the incident laser pulse interacting with the oxide film [232], or thermal effects associated with the presence of the thermal oxide films [61], and these topics should be carefully considered in future work.

In summary, the single pulse fs laser ablation threshold of Si(100) with thermally grown oxide films was determined as a as a function of oxide film thickness, angle of laser incidence, and laser polarization. The measured ablation threshold was found to depend on the optical properties of the thermal oxide on silicon structure. Subtle variations that did not follow the calculated Fresnel reflection and transmission coefficients may be attributed to inconsistencies in the method of changing laser polarization, or due to other thermal or quantum mechanical effects associated with the oxide film that were

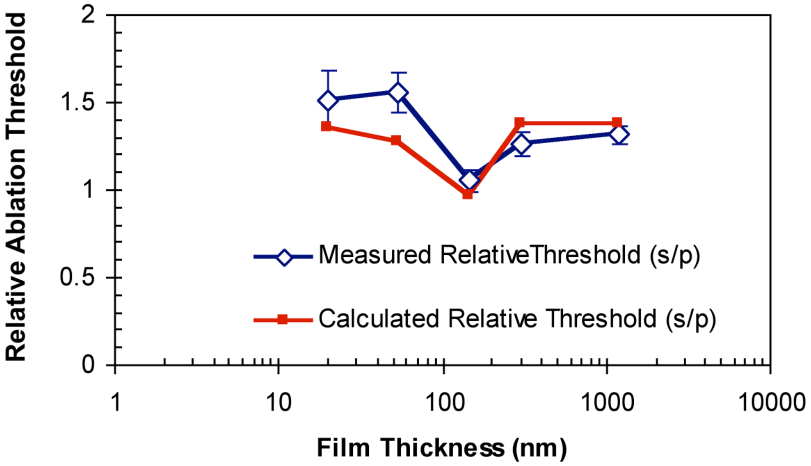

Figure 4.2.6 Relative measured and calculated fs laser single pulse ablation threshold ($F_{s\text{-pol, threshold}}/F_{p\text{-pol, threshold}}$). Calculated relative threshold from Fresnel intensity transmission coefficient neglecting absorption in the oxide film (see Equation 4.1.1).

not considered here. Future work incorporating thermal and quantum mechanical modeling should address these issues.

4.3 Fs laser ablation threshold and ablated crater depths of the Ni-based superalloy CMSX-4

In this section, the single pulse fs laser ablation threshold is of the Ni-based superalloy CMSX-4 is presented. The single pulse ablation depth as a function of incident laser fluence was also determined. Two regimes of ablation were observed as a function of laser fluence (the morphology with laser fluence will be discussed in Chapter 5.3), and the fluence threshold for each regime is presented here. A sudden increase in the ablation depth as a function of laser fluence suggested a transition from a low fluence to high fluence regime accompanied by a fundamental change in the mechanism for ablation [116]. Similar regimes of ablation have been observed in other metals [19, 20, 22, 80, 133-136], where the transition to the high fluence regime was attributed to the onset of thermal effects associated with the diffusion of energetic electrons outside of the skin depth of the material which defines the initial volume of excitation [20, 116]. A transition in the character of the ablation morphology was

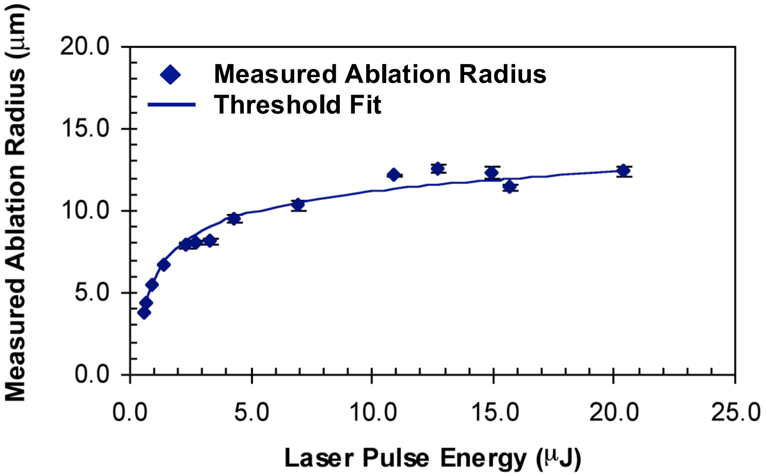

Figure 4.3.1 Results from fs laser ablation threshold experiment on the Ni-based superalloy CMSX-4 in air at normal incidence. Measured ablation radius vs. laser pulse energy with curve fitting (solid line) yielding an ablation threshold of 0.38 ± 0.02 J/cm^2.

also observed as a function of laser fluence (see Chapter 5.3). This transition showed the increasing presence of a molten morphology, along with increased surface roughness on the micrometer length scale. Much of the work presented here was performed in collaboration with Shuwei Ma, and Tresa M. Pollock, and references to their contributions will be made throughout.

4.3.1 Single pulse fs laser ablation threshold of the Ni-based superalloy CMSX-4.

The single pulse ablation threshold of the Ni-based superalloy CMSX-4 was determined in air at normal incidence (for experimental details see Chapter 3.5.3). The results of this experiment are provided in Figure 4.3.1, where the measured equivalent ablation radius as a function of the incident laser pulse energy is presented (for discussion of equivalent ablation radius for determining the ablation threshold, see Chapter 3.3). The measurements presented in Figure 4.3.1 were made of the greatest lateral extent of ablation exhibited by a particular feature, and thus are representative of ablation threshold of the low fluence regime. The fitting routine yields an ablation threshold of 0.38 ± 0.02 J/cm^2 and a Gaussian beam radius of 8.9 ± 0.2 μm. This compares well with independent measurements of the low fluence ablation threshold made by Shuwei Ma (0.3 ±

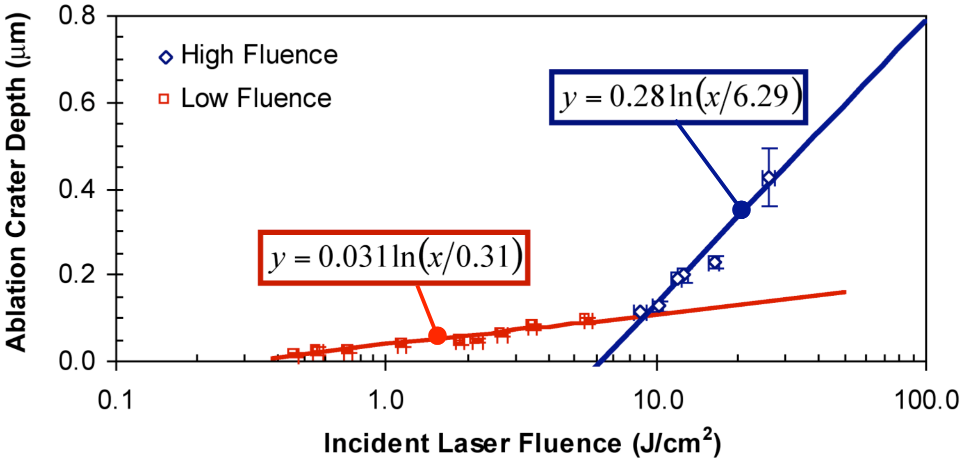

Figure 4.3.2 Fs laser single pulse ablated crater depth as a function of incident laser pulse fluence for Si(100) with native oxide at normal laser incidence in air. Two regimes of fs laser ablation are observed, characterized by a change in the rate of material removal.

0.03 J/cm^2 [116]) and others (0.332 ± 0.014 J/cm^2 [115]). The dimensions of the ablation area corresponding to the high fluence ablation regime were not measured, however the re-solidified molten morphology associated with the high fluence regime (see Chapter 5.3) was observed to disappear at laser fluences between 2.50 ± 0.1 J/cm^2 and 2.2 ± 0.1 J/cm^2, such that the ablation threshold for the high fluence regime can be estimated to be 2.35 ± 0.3 J/cm^2.

4.3.2 Single pulse fs laser ablation depth as a function of laser fluence of the Ni-based superalloy CMSX-4

The maximum crater depth for single pulse fs laser ablation as a function of the incident laser fluence was determined from the same features used to make the ablation threshold measurements in Chapter 4.3.1 above. The experimental details of the ablation rate measurement are provided in Chapter 3.5.3. Briefly, the maximum ablated crater depth was measured via AFM over a range of laser fluences ranging from 0.45 ± 0.02 – 26.2 ± 1.2 J/cm^2 (for images of ablation craters see Figures 5.3.1 and 5.3.2). A semi-log plot of the maximum crater depth as a function of the incident laser fluence is presented in Figure 4.3.2. For each data point, the maximum depth of 6 ablation features was averaged. The plot shows a sudden increase in the measured ablation depth as a function of the laser fluence once the incident laser fluence exceeds ~ 6.3 J/cm^2 (similar to the value of 5.6 J/cm^2 obtained in [116]). Natural logarithm fits to the measured ablation depth as a function of the incident laser fluence are provided in Figure 4.3.2, where different fits are provided for fluences less than and greater than 6.3 J/cm^2. Due to this transition as function of laser fluence, we define the low fluence and high fluence ablation regime for laser fluences less than and greater than 6.0 J/cm^2 respectively. As the threshold fluence for the high fluence regime 6.0 J/cm^2 is significantly greater than the laser fluence at which the molten morphology emerges (2.35 ± 0.3 J/cm^2), we conclude that the melt like morphology may not be directly associated with the change in the ablation mechanism associated with the sudden increase in ablation crater depth as a function of laser fluence.

Similar regimes of ablation as a function of fluence (defined with respect to the ablation depth as a function of laser fluence) have been observed for other materials included Au, Cu, and Ag [19, 20, 22, 80, 133-136]. A model explaining the presence of two ablation regimes was developed based on the two temperature model [20]. The two-temperature model treats the relative temperatures of the electrons and ions in the first several ps following absorption of the laser energy with two coupled, ordinary differential equations [108, 109]. In the low fluence regime, it was proposed that the ablated crater depth as a function of incident laser fluence was largely determined by the skin depth of the material, the depth to which the energy is initially deposited by the laser pulse [110]. In the high fluence regime, it has been suggested that before the energetic electrons (which initially absorb the laser radiation) and ions of system come into equilibrium (i.e. the first few 10's of picoseconds [108]), thermal diffusion of energetic electrons beyond the region of material defined by the skin depth results in a sudden increase in the depth of ablation craters [20]. In this fashion, the low fluence regime can be thought of as the skin depth regime, and the high fluence regime can be thought of as the electron thermal diffusion regime. The range of electron diffusion is dictated the density of energetic electrons initially produced by the incident laser pulse [20]. To a point, this electron diffusion is limited to depths less than or equal to the skin depth in the material, however once a critical electron density is reached (as the laser fluence is increased), thermal diffusion outside of the skin depth occurs accompanied by an increase in the ablation depth. Estimates of the skin depth and electron thermal diffusion length can be determined from logarithmic fits to measured ablation crater depth as a function of laser fluence within the two regimes [20].

It was proposed that in the low fluence regime, the measured ablation depth L, as a function of laser fluence will follow a logarithmic dependence given by [20]:

$$L = \delta \ln\left(F_0 / F_{Th,1}\right) \tag{4.3.1}$$

where δ is the skin depth of the material at the wavelength of the incident laser pulse (in this case, the wavelength was 780 nm), F_0 is the incident laser fluence, and $F_{Th,1}$ is the threshold for material removal in the low fluence regime. In the high fluence regime, the measured ablation depth as a function of laser fluence was proposed to follow a logarithmic dependence given by [20]:

$$L = l \ln\left(F_0 / F_{Th,2}\right) \tag{4.3.2}$$

where l is the heat penetration depth, F_0 is the incident laser fluence, and $F_{Th,2}$ is the threshold for the high fluence regime. Applying this analysis to the measured ablation depth as a function of the incident laser fluence for the Ni-based superalloy CMSX-4 yields: $\delta = 31 \pm 3$ nm, $F_{Th,1} = 0.31 \pm 0.05$ J/cm^2 and $l = 280 \pm 30$ nm, and $F_{Th,2} = 6.3 \pm 0.6$ J/cm^2. These values compare favorably with those reported for CMSX-4 in [116] where $\delta = 18$ nm, $F_{Th,1} = 0.298$ J/cm^2 and $l = 165$ nm, and $F_{Th,l} = 5.6$ J/cm^2.

The calculated skin depth of Ni (the primary constituent of the CMSX-4 superalloy) is 11.8 nm at a wavelength of 780 nm [233], approximately 1/3 of value of $\delta = 31 \pm 3$ nm determined from the fitting routine. Furthermore, calculation of the heat diffusion length for Ni following [20] yields approximately 68 nm, a value approximately 1/4 the value of $l = 284 \pm 31$ nm determined from the fitting routine. As concluded for similar studies of single pulse fs laser ablation of the Ni-based superalloy CMSX-4 [116] (and other metals including Al [135]), the theory does not appear to fully described fs laser ablation of the CMSX-4 superalloy.

In summary, the single pulse fs laser ablation threshold of the Ni-based superalloy CMSX-4 was determined to be 0.38 ± 0.2 J/cm^2 from OM images of ablation features. This value compares favorably with the ablation threshold found in other studies [115, 116]; however discrepancies emphasize the significance of experimental conditions on threshold measurements. In contrast to the experiments performed here, the author suggests that ablation threshold experiments should be performed with relatively weak focusing conditions (i.e. focused beam waists on the order of 20 μm or greater). Such conditions will result in greater depth of focus, reducing the difficulty of placing the sample at the precise location of the laser focus (see Appendix 1). Furthermore, larger ablation features will be produced which are easier to accurately measure from OM images than smaller features produced with stronger focusing conditions. These suggestions are appropriate for ablation threshold measurements for all materials, including silicon.

Analysis of the depth of ablation features over the range of laser fluences from 0.45 ± 0.02 – 26.2 ± 1.2 J/cm^2 revealed the presence of two regimes, with the transition between the regimes occurring at around 6.3 ± 0.6 J/cm^2. Models developed by other works [20] were applied to the measured ablation depth as a function of laser fluence, yielding approximations for the skin depth (δ = 31 ± 3 nm) and electron thermal diffusion length (l = 284 ± 31 nm) of the CMSX-4 superalloy. These values exceed independently calculated values for the skin depth of Ni (δ_{calc} = 11.8 nm) and electron thermal diffusion length (l_{calc} = 68 nm [116]), indicating that application of this model may not be appropriate in this case [135]. A greater understanding of the mechanisms for fs laser ablation including the dynamics of energetic electrons and associated thermal effects is necessary particularly for more complicated metallic alloys.

Chapter 5

Femtosecond laser induced ablation morphology

5.1 Femtosecond laser induced ablation morphology on Si(100) with and without the native oxide.

The role of the native oxide of crystalline silicon on the surface morphology accompanying multiple pulse femtosecond laser ablation was characterized using scanning electron (SEM) and optical microscopy (OM)[73]. A direct comparison of the ablation morphology produced on atomically clean Si(100) (no native oxide) and Si(100) with the native oxide was obtained by machining samples at grazing laser incidence in an ultra high vacuum (UHV) environment (10^{-11} Torr) where the presence or absence of the native oxide could be controlled with conventional semiconductor processing techniques (for experimental details, see Chapter 3.4). The ablation morphology on samples with the native oxide was observed to exhibit a pitted ring of ablation feature, which was not observed on atomically clean Si(100) samples. Following this observation, a series of experiments was also performed in air to further understand the pitted ring of ablation morphology observed on samples with the native oxide. From these investigations, a model was proposed to explain the presence of this morphology feature, suggesting specifically that ablation and modification thresholds of the native oxide film are responsible for the pitted ablation ring. Other groups have observed the pitted ring of ablation as well (on Si and Ge), attributing its presence to the relative melting and evaporation temperatures of the substrate material and its native oxide [52, 118]. The results

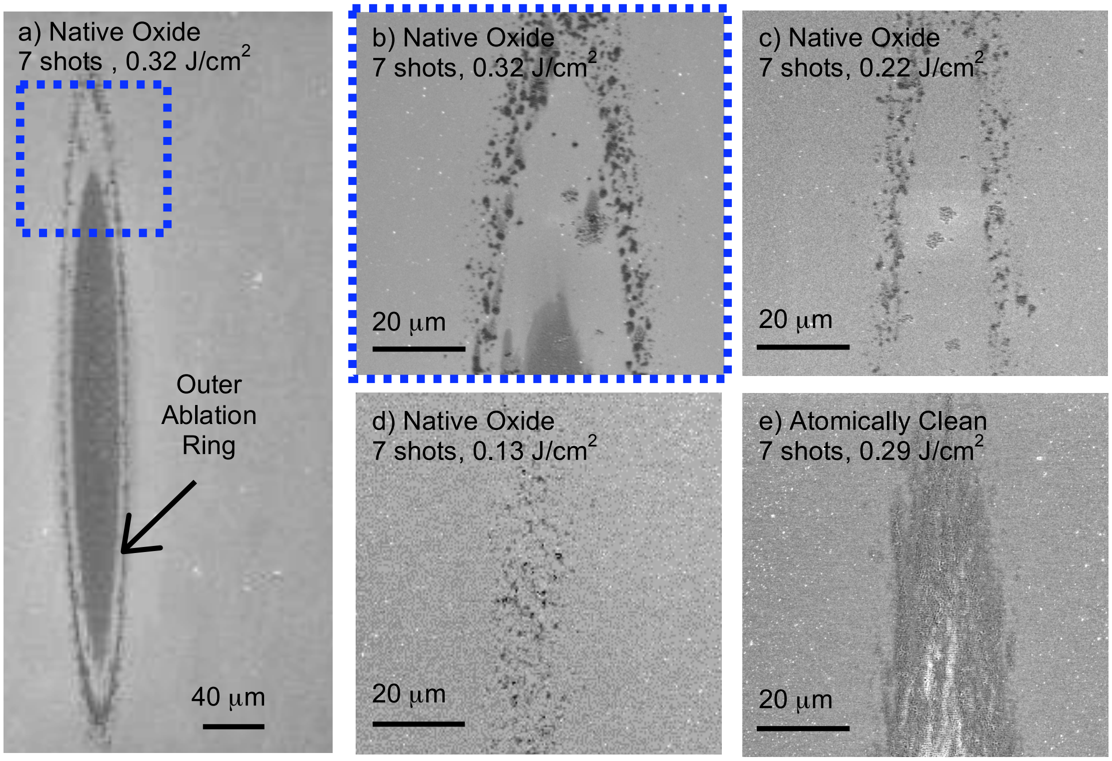

Figure 5.1.1 SEM images of elliptical laser ablation features produced on Si (100) with seven laser pulses at peak fluences shown. a) Feature produced with peak fluence of 0.32 J /cm^2 showing pitted damage ring surrounding undamaged Si and a central damage crater. Arrow indicates outer ablation ring. b) Image of inset from a) showing detail of pitted ablation ring, central damage region and intermediate undamaged region. c) Feature produced with peak fluence of 0.22 J /cm^2 showing only ring of ablation surrounding a relatively undamaged region. d) Feature produced with peak fluence of 0.130 J /cm^2 showing pitted ablation region. e) Feature produced on atomically clean Si (100) with 7 laser pulses of peak fluence of 0.290 J /cm^2. Notice the absence of any ablation ring feature.

of an investigation of the influence of the native oxide of silicon on multiple pulse fs laser ablation is provided in the following section.

5.1.1 Pitted ring of ablation morphology on silicon with native oxide

The experimental details for these studies are presented in Chapter 3.4. Briefly, in an UHV chamber, the ablation morphology resulting from irradiation with 7 fs laser pulses was studied as a function of incident laser fluence (0.13 – 0.32 J/cm^2) for Si(100) with and without the native oxide. In air, the ablation morphology was characterized as a function incident number of laser pulses (1 – 20 pulses) at a fixed laser fluence (0.280 J/cm^2) on Si(100) samples with native oxide. For ablation studies performed in UHV, observation of the fs laser ablation

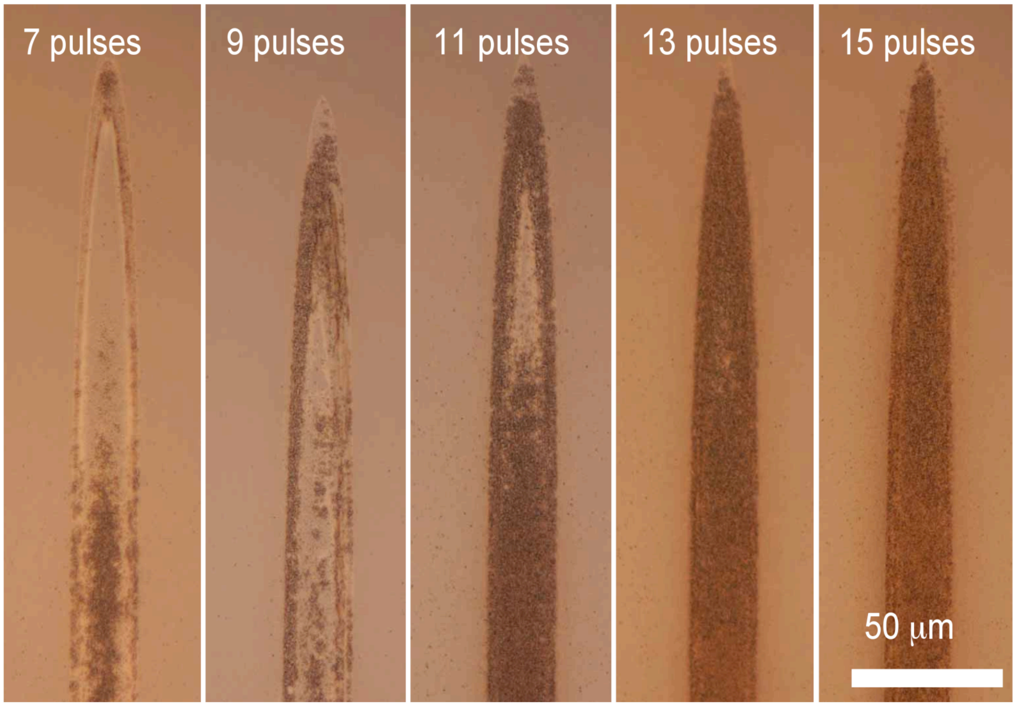

Figure 5.1.2 OM images (in Nomarski mode) of grazing incidence feature fs laser ablation morphology of Si(100) with native oxide as a function of number of laser pulses. Features were produced with laser fluence of 0.28 J/cm^2 in air, with number of pulses shown. Scale presented at lower right applies to all images. The un-ablated region between the pitted ring of ablation and the central ablation region fills as the number of pulses increases, eventually filling in completely after 15 pulses yielding a homogeneously ablated region.

morphology ex-situ with SEM revealed the presence of a pitted ring of ablation on samples with the native oxide that was never found on samples that were atomically clean at the time of laser exposure.

Figure 5.1.1a)-d) shows the evolution of the pitted ring of ablation with decreasing laser fluence produced with 7 laser with p-polarized laser pulses at ~ 80° laser incidence (with respect to the sample normal). Figure 5.1.1e) shows the ablation morphology produced on an atomically clean Si(100) sample with 7 laser pulses at a laser fluence of 0.29 J/cm^2 where no such pitted features observed. Recall that due to the grazing incidence laser geometry, the ablation features take the form of elongated ellipses on the sample surface. At a laser fluence of 0.32 J/cm^2 (Figure 5.1.1a) and b)), the ablation morphology exhibits a central ablation region, which is surrounded by a region of apparently undamaged silicon, which is in turn surrounded by an ellipse or ring of pitted features. As the laser fluence is reduced, (Figure 5.1.1c)) the central ablation region disappears, and the pitted features are found to surround a region of un-ablated silicon. Finally, when the laser fluence is reduced to 0.13 J/cm^2 (Figure 5.1.1d)), the ablation morphology consists of only a region of pitted features. These observations demonstrate that the location of the pitted features relative to the center of the ablation feature was dependent on the incident laser fluence, with the pits moving closer to the center of the irradiated region as the incident laser fluence was decreased.

Figure 5.1.2 presents Normarki mode OM of fs laser induced ablation morphology on Si(100) samples with the native oxide as a function of the number of incident laser pulses used to produce the ablation feature. All features in Figure 5.1.2 were produced with a laser fluence of 0.28 J/cm^2 at a laser incidence of 84.4° with respect to the sample normal. The ablation morphology evolved with increasing laser pulse exposure. Initially the pitted ring of ablation feature was well defined, surrounding an un-ablated region of silicon which in turn surrounds a region of homogeneous ablation (Figure 5.1.2, 7 pulses). As the number of laser pulses used to make a particular feature was increased, the central homogeneous ablation region expanded outward. Once the laser exposure exceeded ~15 laser pulses, an isolated, defined pitted ring of ablation was no longer apparent, and the ablation morphology was a well defined region of homogeneous roughness. The ablation ring emerged after 2 or more laser pulses were incident on the same location, but was not observed for single pulse irradiation. This may be because the density of the pits in the pitted ablation ring resulting from a single pulse was not sufficient for observation. A similar ablation ring phenomenon emerged for single pulse irradiation of Si(100) with 1200 nm thermal oxide films, which will be discussed in Chapter 5.2.2.

A model was developed to explain the presence of the ablation ring feature and the un-ablated region of silicon based on the evolution of the fs laser ablation morphology of Si(100) with native oxide with laser fluence, and with laser pulse exposure. The details of this model are presented in the following section.

5.1.2 Discussion and models for pitted ring of ablation

A model for the pitted ring of ablation was developed following the observed evolution of the fs laser ablation morphology produced on Si(100) samples with the native oxide as a function of incident laser fluence, and incident laser pulse exposure. The critical feature of this model is a proposed fs laser modification threshold for the native oxide of silicon, which may be related the modification induced in bulk glasses used to produce optical waveguides [234-236]. In terms of physical processes, this modification of the native oxide may take the form of a permanent fs laser induced physical changes (such as densification [78, 79, 237]) or chemical changes (such as the production of color centers [238, 239]) which are not accompanied by material removal. The modification threshold for the native oxide is proposed to occur at a laser fluence which slightly exceeds the ablation threshold of crystalline silicon, but is less than the laser fluence required to directly ablate the native oxide. The mechanism of the modification locally removes energy from the incident laser pulse, such that a reduced energy is locally delivered to the underlying crystalline silicon substrate. Thus, in regions where this modification occurs, ablation of the underlying silicon is inhibited by the reduction in laser fluence due to the modification within the native oxide.

It is useful to discuss this modification mechanism with respect to particular ablation features. A schematic showing the relevant thresholds with respect to the Gaussian spatial fluence profile of the incident laser pulse is presented in Figure 5.1.3. A peak laser fluence corresponding to pulse **A** in Figure 5.1.3 will produce an ablation morphology such as that shown in Figure 5.1.1a) and b). In the center of the focused Gaussian beam the modification mechanism locally removes energy from the laser pulse, however the local fluence is not reduced below the ablation threshold of the underlying Si(100) and ablation from the underlying Si(100) substrate proceeds producing the central ablated region. In this region the modification mechanism within the native oxide is not sufficient to prevent ablation of the substrate, so the laser fluence exceeds the *native oxide ablation threshold*. As the laser fluence decreases away from the center of the Gaussian beam, the modification mechanism within the native oxide eventually reduces the local laser fluence such that it is not sufficient to produce ablation of

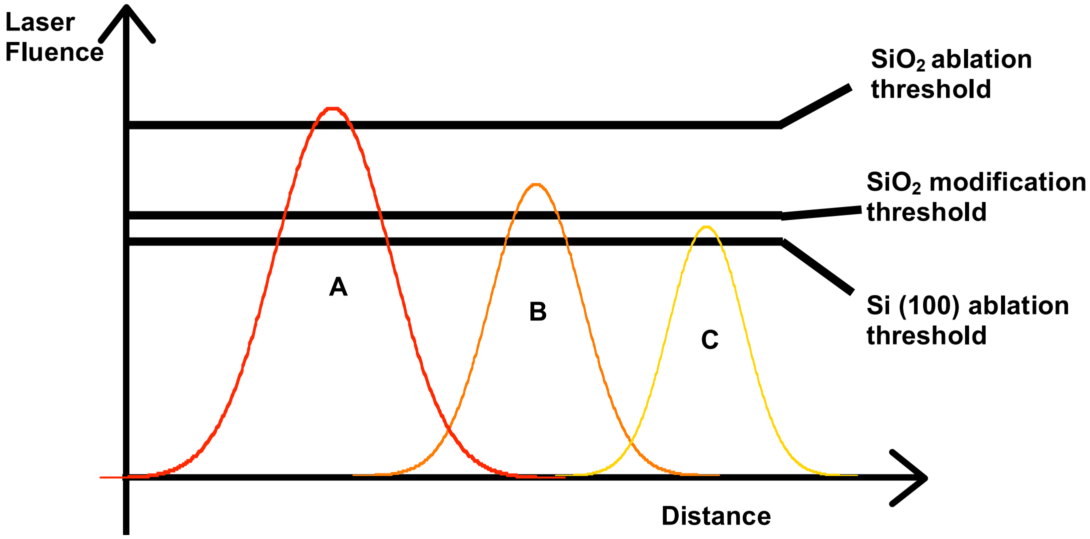

Figure 5.1.3 Schematic showing relevant thresholds underlying the proposed model explaining the production of fs laser ablation morphology observed on Si(100) with native oxide. A laser pulse with a Gaussian fluence profile A will produce an ablation morphology like that shown in Figure 5.1.1a) and b). A laser pulse with a Gaussian fluence profile B will produce an ablation morphology like that shown in Figure 5.1.1c). A laser pulse with a Gaussian fluence profile C will produce an ablation morphology like that shown in Figure 5.1.1d).

the underlying Si(100) substrate material. For these laser fluences below the native oxide ablation threshold, but above the *native oxide modification threshold*, a local region of relatively undamaged silicon is produced. As the laser fluence continues to decrease away from the center of the beam, the local laser fluence is eventually below the modification threshold of the native oxide, such that the modification mechanism does not occur. Because the modification to the native oxide does not occur, the local laser fluence arriving at the silicon substrate exceeds the ablation threshold of the silicon, and a pitted ablation morphology results where the underlying silicon ablates upward through the intact native oxide.

As the peak laser fluence is reduced, such as pulse **B** in Figure 5.1.3, the local laser fluence in the center of the focused Gaussian beam drops below the ablation threshold of the native oxide. However, the peak fluence is still above the modification threshold of the native oxide, so that the laser energy locally arriving at the silicon surface is not sufficient to produce ablation of the Si(100) substrate. This results in ablation features such as that presented in Figure 5.1.1

c), where the pitted ring of ablation surrounds a relatively undamaged region of Si(100). Finally, as the peak laser fluence is decreased below the modification threshold of the native oxide (pulse C in Figure 5.1.3) the local laser energy is fully delivered to the underlying substrate producing an ablation feature that consists of a region of pitted ablation.

The observed evolution of the ablation morphology as a function of the number of laser pulses used to produce a particular feature is consistent with a model that includes a laser induced modification of the native oxide film. It is proposed that the mechanism responsible for the modification saturates with increased laser exposure, eventually allowing the native oxide to under go traditional ablation once this saturation occurs. This saturation is also consistent with observations made by groups writing waveguides in glasses where the laser induced refractive index change is dependent on the total laser dose [235]. Furthermore, observation of fs laser induced color centers, or local defects in fused silica have been found to be dependent on the net dose of radiation [240, 241].

Other models have recently been proposed to explain the presence of the pitted ablation ring morphology pointing to the relative melting and evaporation temperatures of the native oxide and the underlying substrate material [52, 118]. The native oxide of silicon (SiO_2) melts at a higher temperature than the underlying silicon, but evaporates at a lower temperature. The pitted ring of ablation may then result where the local temperature exceeds the evaporation temperature of the oxide but not the evaporation of the underlying silicon substrate. The undamaged region of silicon would be produced because the temperature of the silicon was not sufficient for evaporation or removal of material. Once exposed to air, the native oxide re-grows in a non-uniform fashion covering the undamaged silicon but leaving a rough pitted appearance where the re-growing native oxide encounters the un-evaporated native oxide [52, 118]. This model is also consistent with the observed ablation morphology, and may provide an additional explanation for the observations presented here.

In summary, the presence or absence of the native oxide of Si(100) was observed to influence both the fs laser ablation threshold (Chapter 4.1) and ablation morphology, particularly under multiple pulse exposures. With respect to the ablation morphology, a pitted ring of ablation feature was observed in the presence of the native oxide that was not found on atomically clean Si(100) samples laser machined under UHV conditions. The location of the pitted ring of ablation relative to the center of the laser induced damage feature was found to depend on the peak laser fluence of the focused Gaussian beam. Furthermore, the ring of ablation feature was observed to saturate after increased laser pulse exposure.

Three relevant thresholds with respect to laser fluence were proposed to underlie the observed phenomenon. In order of decreasing laser fluence these thresholds include the ablation threshold of the native oxide, the modification threshold of the native oxide, and the ablation threshold of the underlying crystalline silicon. For a laser pulse with a peak fluence exceeding the ablation threshold of the native oxide, an ablation morphology was produced with a central damage region, surrounded by a region of relatively undamaged silicon, which in turn was surrounded by a pitted region of ablation. At this laser fluence, increased laser pulse exposure resulted in an increase in the area of the central damage, such that the central damage region eventually met up with the pitted ring of ablation producing a homogeneous ablation morphology. The proposed modification of the native oxide may result from a physical mechanism similar to that exploited to produce optical waveguides in bulk glasses with fs lasers [78, 79, 234-237], or the production of defects or color centers in glasses observed under fs laser irradiation [238-241].

5.2 Fs laser ablation morphology of Si(100) with thermally grown oxide and plasma enhanced chemical vapor deposited oxide films.

Femtosecond laser ablation surface morphology was investigated for ablation features produced on Si(100) substrates with thin thermally grown oxide (SiO_2) films (20 nm, 54 nm, 147 nm, 300 nm, and 1200 nm in thickness) and a single

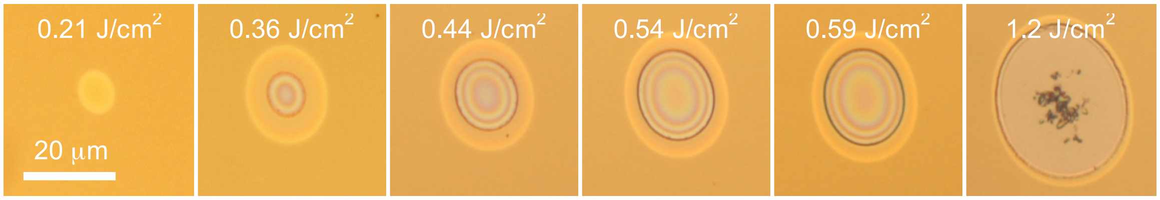

Figure 5.2.1 OM images showing progression of ablation morphology on Si(100) with a 300 nm thermally grown oxide film as a function of single pulse fs laser fluence. The laser fluence for each feature is shown at the top, and the scale bar at the low left applies to all features. For the image at a laser fluence of 0.21 J/cm^2, some modification is apparent however it is confined to the substrate film interface, and no measurable (via AFM) change to the oxide surface is observed. For laser fluence ranging from 0.36 – 0.59 J/cm^2, the images show a blistering phenomenon in which the oxide film is delaminated from the substrate but remains intact with the rest of the film. This blistering is indicated by the concentric rainbow pattern within the features. Finally, for a laser fluence of 1.2 J/cm^2, the oxide film is removed, exposing the substrate. Some debris from the oxide film are present in the center of the crater.

Si(100) substrate with a 1200 nm plasma enhanced chemical vapor deposited (PECVD) oxide (SiO_2) film [74, 75]. Two primary ablation morphologies were observed; one in which the thermal oxide film remained intact over the irradiated area, and the other in which the thermal oxide film was completely removed. Figure 5.2.1 shows OM images of the progression of the ablation morphology as a function of the incident laser fluence for Si(100) with a 1200 nm thermal oxide.

For laser fluence exceeding ~0.5-0.7 J/cm^2 (depending on film thickness), the oxide films were cleanly removed from the silicon substrate, producing a crater with depth approximately equal to the thickness of the film. For laser fluence less than ~0.5-0.7 J/cm^2, but greater than about 0.3 J/cm^2, a buckling or blistering event was observed in which the oxide film was delaminated from the underlying substrate but remained intact with the rest of the film. The mechanics of fs laser induced thin film buckling where studied by characterizing the dimensions (height and width) of circular blisters produced on samples with 300 nm and 1200 nm oxide, allowing the intrinsic stress and fracture energy of the film/substrate system to be calculated.

Single, isolated blisters were connected together to produce linear blister channels in 1200 nm thermally grown and PECVD grown oxide films on Si(100) [75]. The dimensions of linear blister channels were also analyzed with the theory of thin film buckling mechanics [144, 145, 149, 150], yielding values for the

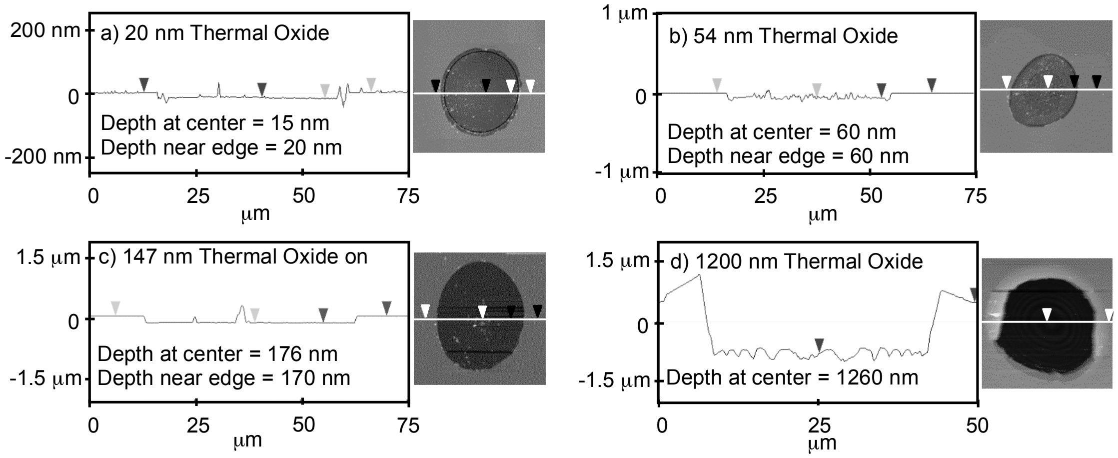

Figure 5.2.2 AFM section analysis showing single shot fs laser removal of thermal oxide layer from Si(100) for four different film thicknesses. Oxide thickness and peak laser fluence are shown. On left, line scans showing feature depth are presented for the AFM image at right. Note the varying vertical and horizontal scales. a) Si(100) with 20 nm of thermal oxide at a peak fluence of $F_0 = 0.77$ J/cm^2. b) Si(100) with 54 nm of thermal oxide at a peak fluence of $F_0 = 0.99$ J/cm^2. c) Si(100) with 147 nm of thermal oxide at a peak fluence of $F_0 = 0.83$ J/cm^2. d) Si(100) with 1200 nm thermal oxide at a peak fluence of $F_0 = 0.99$ J/cm^2. Ripples or concentric rings at the bottom of the crater are absent when the laser is incident off normal (see Figure. 4).

intrinsic film stress which were similar to the measured film stress and those provided in the literature for similar films [242-244]. Simple fluidic devices were created with the linear blisters produced in 1200 nm PECVD oxide on Si(100), in which the flow of water by capillary action, and the flow of charged nano-spheres by DC electrophoresis were demonstrated. The results of these investigations are presented and discussed in the following section.

5.2.1 Femtosecond laser induced removal of thin oxide films from silicon substrates.

As shown in the AFM images presented in Figure 5.2.2, fs laser induced removal of the thin oxide films was observed for all film thicknesses. For laser fluences just exceeding the threshold for oxide film removal, the ablation morphology consisted of a crater with a smooth bottom surface and depth approximately equal to the thickness of the film. The depth and roughness of the bottom surface of the crater increased with increasing laser fluence in excess of the threshold for film removal. The critical laser fluence required to remove the oxide film was found to be dependent on the film thickness, generally increasing

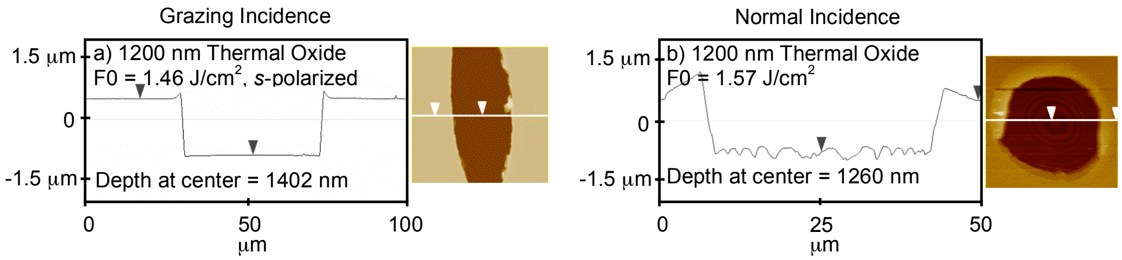

Figure 5.2.3 AFM section analysis showing single shot fs laser removal of 1200 nm thermal oxide film from Si(100) for similar laser fluences at a) grazing laser incidence (71.4° to sample normal) and b) normal laser incidence. The substrate surface (bottom of the crater) is much smoother for grazing laser incidence than for normal laser incidence, where concentric ripples with amplitude as great as 200 nm are present. The concentric ripples were a common feature of normal incidence ablation of Si(100) with thermal oxide films (see Figure 5.2.4)

with increased film thickness. As shown in Figure 5.2.3, grazing laser incidence was observed to produce the cleanest oxide removal, yielding a crater with minimal laser induced roughness at the substrate surface.

For normal laser incidence at fluences above the threshold for oxide film removal, the morphology at the bottom surface of the crater showed distinct concentric rings for samples with 54nm, 147 nm and 1200 nm of thermal oxide and PECVD oxide. As shown in Figure 5.2.4 for a sample with 1200 nm of PECVD oxide, the rings structure evolves with increasing laser fluence, obscuring at higher laser fluence when the center of the damage crater develops significant roughness. As demonstrated in Figure 5.2.5, the rings present at the bottom of the craters on samples with 147 nm of oxide were of higher frequency (shorter wavelength) and lower amplitude relative to the rings observed at the bottom of craters produced on samples with 1200 nm of oxide.

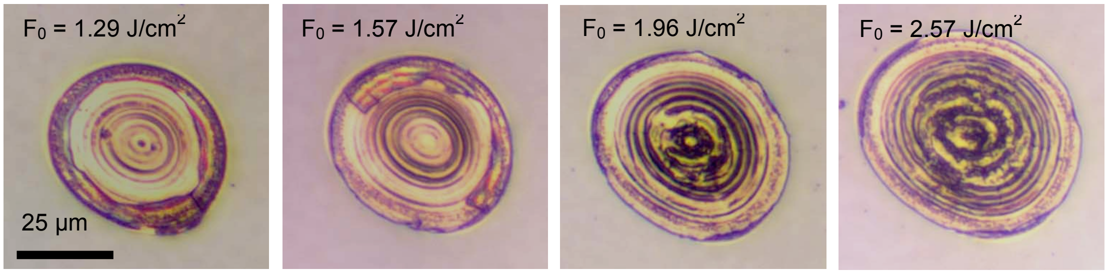

Figure 5.2.4 OM images showing progression of concentric ring pattern at the bottom of craters produced on Si(100) with a 1200 nm thermally grown oxide film as a function of single pulse fs laser fluence. The laser fluence for each feature is shown at the top, and the scale bar at the low left applies to all features.

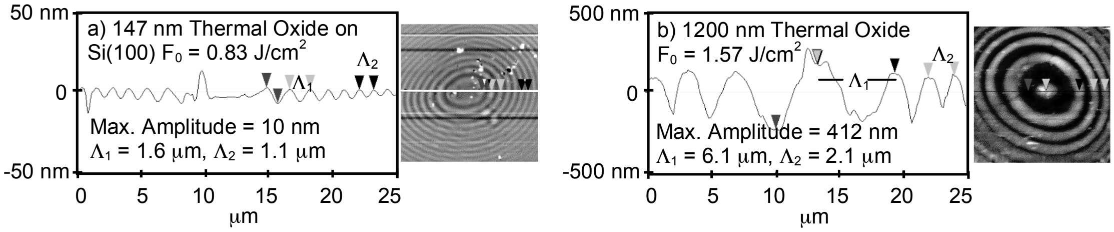

Figure 5.2.5 AFM section analysis showing concentric rings present at the bottom of damage crater produced on Si(100) with 147 nm and 1200 nm of thermal oxide. On left, line scans showing maximum bubble height are presented. On right, the AFM image showing location of line scan. The ripple spacing is a decreasing function of the radius, while the amplitude is dependent on film thickness and incident laser fluence. a) Bottom of damage crater produced on Si(100) with 147 nm thermal oxide. b) Bottom of damage crater produced on Si(100) with 1200 nm thermal oxide.

Although the source of the rings is not completely understood, diffraction of the incident laser beam can be ruled out due to the radial dependence of the spacing of the rings. Fraunhofer diffraction from a circular aperture produces rings which are evenly spaced [231], while Figure 5.2.5 demonstrates that the spacing between consecutive rings decreases as the distance from the center of the feature is increased. The rings may form when the glass film is forced upward from the molten substrate during the ablation event. This abrupt separation of the film from the substrate would likely be accompanied by the formation of physical waves in the molten substrate. Standing waves may then form upon reflection of the primary waves from the interface of the substrate and the surrounding film that was not ablated.

5.2.2 Fs laser induced buckling of oxide thin films

At lower laser fluences than was required to remove the oxide film (~0.3 J/cm^2 < F_0 < ~0.7 J/cm^2), buckling or blister formation was observed to result from fs laser irradiation of Si(100) substrates with oxide films. Figure 5.2.6 presents OM of blisters produced at normal laser incidence in 54 nm, 147 nm, 300 nm, and 1200 nm of thermally grown oxide on Si(100). The mechanism responsible for fs laser induced film buckling is thought to be a combination of relaxation of intrinsic compressive stress in the film released when the film is separated from the substrate, and momentum transferred to the expanding film from the ablation event at the substrate/film interface [74, 76]. Similar buckling

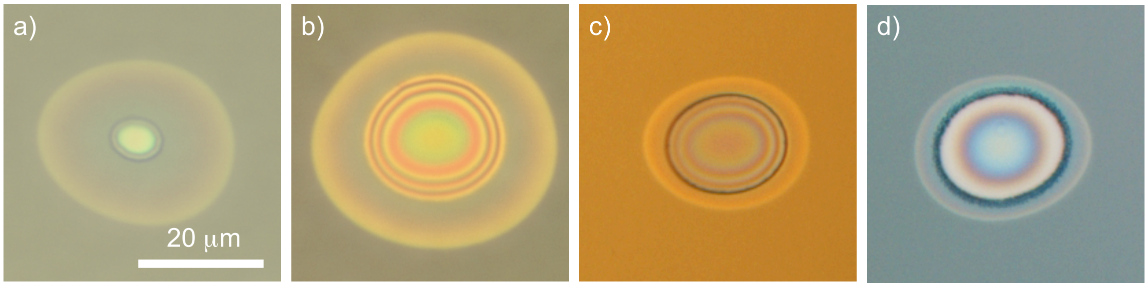

Figure 5.2.6 OM images of Blister features produced in thermally grown oxide films with single femtosecond laser pulses. a) 54 nm thermal oxide, laser fluence = 0.33 J/cm^2 b) 147 nm thermal oxide, laser fluence = 0.33 J/cm^2 c) 300 nm thermal oxide, laser fluence = 0.59 J/cm^2 d) 1200 nm thermal oxide, laser fluence = 0.64 J/cm^2 Scale bar in a) applies to all images. Rainbow interference pattern is indicative of the buckling event.

has been observed for thin aluminum films on quartz substrates and thin thermal oxide films (< 100 nm thick) on silicon following ns irradiation [152, 153]. Figure 5.2.7 presents AFM of fs laser induced blisters in 1200 nm and 147 nm thermally grown oxide films, demonstrating that blister height can be increased by increasing the incident laser fluence or by increasing the number of laser used to produce a particular feature.

Blister features were also produced at grazing laser incidence. Blisters produced in 54 nm and 147 nm at grazing incidence exhibited the so called telephone cord instability, a phenomenon often accompanying buckling of compressively stressed thin films [149, 150, 152, 245, 246]. Examples of blisters produced in the 147 nm thermal oxide film exhibiting the telephone cord instability are presented in Figure 5.2.8. As shown in Figure 5.2.9, blisters produced at grazing laser incidence on samples with 1200 nm thermal oxide did not exhibit the telephone cord instability, presumably because the magnitude of the intrinsic compressive stress is known to decrease with increasing film thickness [243].

To summarize to this point, two primary surface morphologies were found to accompany fs pulsed laser ablation of Si(100) with thermally grown oxide films and PECVD oxide films. For laser fluence exceeding ~ 0.6-0.7 J/cm^2 (depending on film thickness), the oxide film was removed from the substrate and fractured from the surrounding film, leaving a damage crater of depth approximately equal

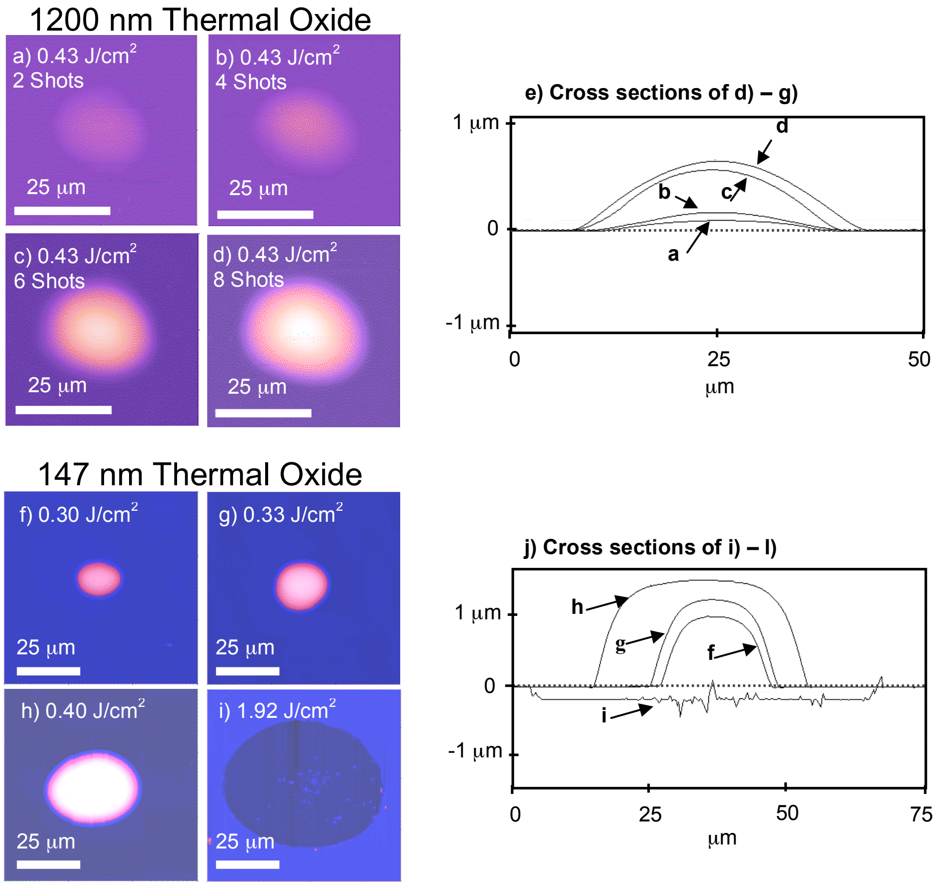

Figure 5.2.7 AFM of fs laser induced damage features produced on thermally oxidized Si(100) with 1200 nm a) - e) and 147 nm f) - j) oxide thickness. In images d) – g) blister features produced in 1200 nm thermal oxide on Si(100) with laser fluence = 0.43 J/cm^2 produced using a number of laser pulses as follows: a) 2 laser pulses b) 4 laser pulses c) 6 laser pulses d) 8 laser pulses. h) AFM section analysis showing maximum height of of features in a) – d). In images f) – h), blister features produced on thermally oxidized Si(100) with a 147 nm thick oxide with laser fluences: f) 0.3 J/cm^2 g) 0.33 J/cm^2 h) 0.40 J/cm^2. i) Ablation crater (thermal oxide film removed) produced at laser fluence = 1.92 J/cm^2. j) AFM section analysis of features in f) – i) demonstrating the heights of the blister features and depth of the ablation crater.

to the thickness of the film. For laser fluence between ~0.3 – ~0.6 J/cm^2, a thin film buckling phenomenon was observed in which the oxide film was delaminated from the underlying substrate but remained intact with the rest of the film producing blister features. Blister features were observed for 54 nm, 147 nm, 300 nm, and 1200 nm thermally grown and 1200 nm PECVD oxide films on Si(100). The mechanism underlying fs laser induced film buckling is thought to be a combination of relaxation of intrinsic compressive film stress, and momentum transfer from the material ablating from the silicon substrate. Under this proposed mechanism, it is suggested that the incident laser pulse energy is largely

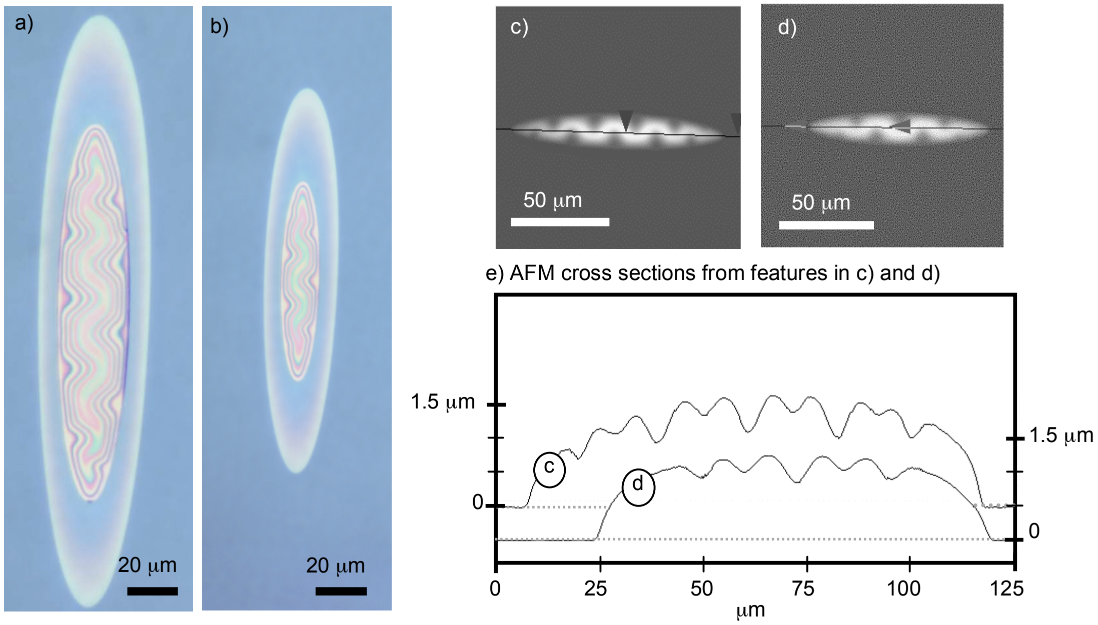

Figure 5.2.8 OM images and AFM of blister features produced on Si (100) with 147 nm of thermal oxide with single fs laser pulses at grazing incidence ≅ 77.4° to sample normal. The laser was p-polarized with respect to the sample surface. The features exhibit the telephone instability, a common feature associated with buckling delamination of compressively stressed films. a) OM image of feature produced with $F_0 = 0.58$ J /cm^2. b) OM image of feature produced with $F_0 = 0.58$ J /cm^2. c) and d) present AFM images and section analysis of features produced at same laser fluence as a) and b) respectively. e) AFM cross sections of features in c) and d). Cross sections have been offset for clarity. c) $F_0 = 0.58$ J /cm^2, max height = 1705 nm, and width = 21 µm. b) $F_0 = 0.47$ J /cm^2, max height = 1302 nm, and width = 15 µm.

absorbed at the substrate film interface, with little modification to the oxide film, or the laser pulse during its propagation through the film. The mechanics of fs laser induced film buckling is discussed in Chapter 5.2.5 where the role of the laser ablation event at the substrate/film interface on film buckling is identified. The following section presents ablation morphologies produced at laser fluences less than 0.3 J/cm^2 where film buckling is not observed, laser fluences near 0.6-0.7 J/cm^2 where film buckling transitions to film removal, and high laser fluences ($F_0 > 2$ J/cm^2)

5.2.3 Additional fs laser ablation morphologies on Si(100) with oxide thin films

Other distinct morphologies were observed for fs laser ablation of Si(100) with thermally grown and PECVD oxide films. For incident laser fluence less than that required for film buckling ($F_0 <$ ~0.3 J/cm^2), OM images of fs laser induced

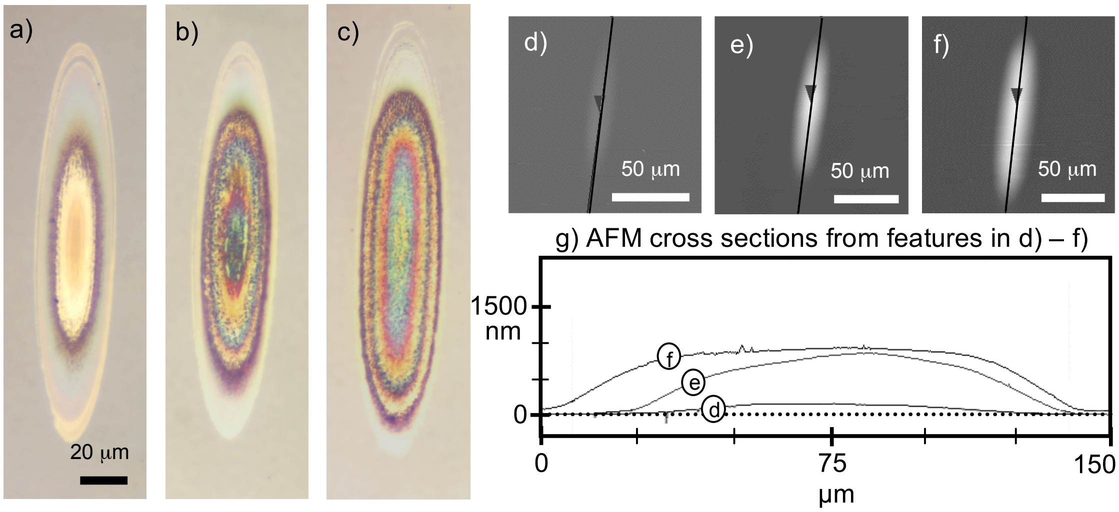

Figure 5.2.9 OM images a) – c) and AFM d) – g) of blister features produced on Si (100) with 1200 nm of thermal oxide with multiple fs laser pulses at grazing incidence (77.4° to sample normal) with a laser fluence = 0.47 J/cm^2. The laser was p-polarized with respect to the sample surface. Blister features were produced with a) 3 laser pulses b) 5 laser pulses and c) 10 laser pulses. d) – f) are AFM images of blisters in a) – c) respectively. g) AFM cross sections of features in d) – f).

damage features showed the presence of a ring-like modification presumably confined to the substrate/film interface (no change to the surface of the oxide film was observed via AFM). An example of this damage morphology produced on Si(100) substrates with 1200 nm thermal oxide is shown in Figure 5.2.10 a). This feature is similar to the ring of pitted ablation features observed with multiple pulse fs laser ablation of Si(100) with a native oxide (see Chapter 5.1). In the case of the thicker thermal oxide, however, no such pitted features were observed. Furthermore, the ring features were observed after single pulse

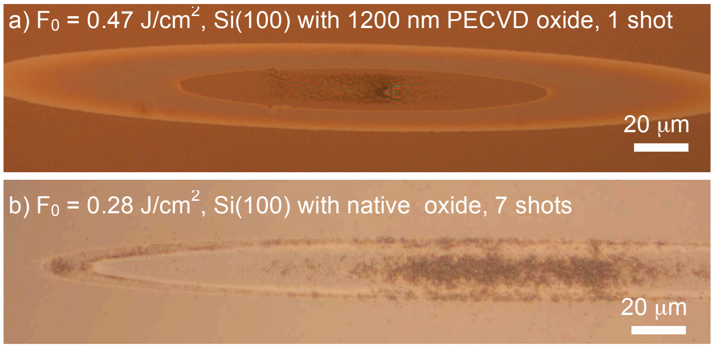

Figure 5.2.10 OM images of fs laser ablation ring features produced on: a) Si(100) with a 1200 nm PECVD oxide film with 1 laser pulse at a peak laser fluence of 0.47 J/cm^2 b) Si(100) with native oxide with 7 laser pulses at a peak laser fluence of 0.28 J/cm^2.

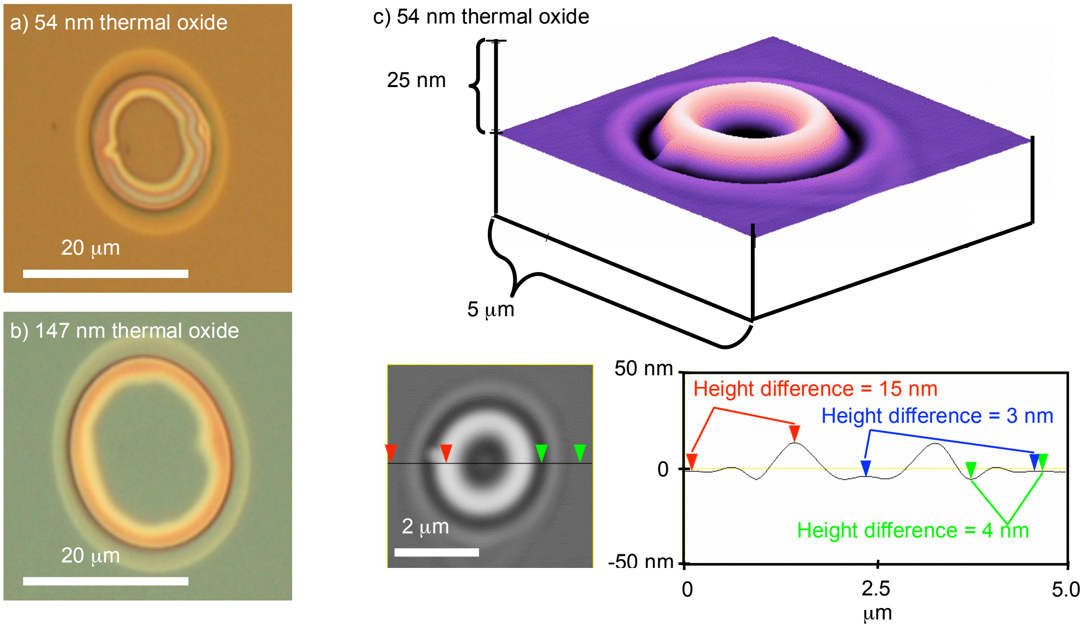

Figure 5.2.11 OM images and AFM of collapsed blister features produced in thermally grown oxide films with single femtosecond laser pulses at normal incidence. a) 54 nm thermal oxide, $F_0 = 0.34$ J/cm^2 b) 147nm thermal oxide, $F_0 = 0.44$ J/cm^2 c) AFM surface image and section scan of collapsed blister produced in 54 nm thermal oxide film at normal incidence with laser fluence approximately 0.3 J/cm^2.

exposures. The well defined ring surrounds a region with only slight damage or ablation apparent via OM. As in Chapter 5.1.2, the presence of the relatively undamaged region within the ring feature attributed to a laser fluence dependent modification of the oxide film. The mechanism associated with this modification is proposed to remove energy from the incident laser pulse at the center of the feature thereby eliminating ablation of the substrate in that region [73]. In this case, it is thought that the ring of ablation is not accompanied by pitted features as the oxide films was simply too thick (20 nm or greater) to allow for the localized ablation at the substrate to explode up through the film.

For oxide films of thickness ≤ 147 nm, partial blister features were observed in which a ring of buckled film surrounded a region of oxide in contact with the silicon substrate. Partial blister features were observed throughout the range of laser fluences associated with film buckling (0.3 – 0.7 J/cm^2). Examples of partial blisters are shown Figure 5.2.11 a) and b) where OM images show that the color interior and exterior to the feature are the same, indicating the oxide film is still present at the center of the feature and is in contact with the substrate. The AFM

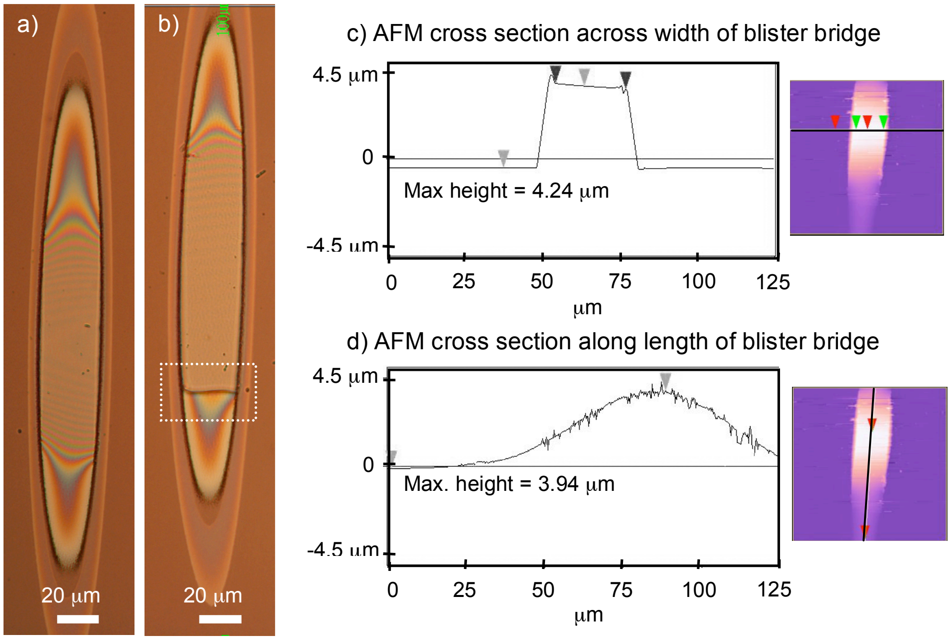

Figure 5.2.12 OM images of single pulse fs laser ablation features produced with s-polarized light at grazing laser incidence (83.4° to sample normal) on Si(100) with a 1200 nm PECVD oxide film. a) Blister bridge feature, laser fluence = 0.56 J/cm^2. b) Partially fractured blister bridge feature (indicated by dotted square), laser fluence = 0.56 J/cm^2. c) AFM image and cross section laterally across width of blister bridge. d) AFM image and cross section along length of blister bridge.

analysis of a similar feature produced in the 54 nm thermal oxide film (Figure 5.2.11 c)) indicates that the height of the material at the interior is only 3 nm less than that exterior to the feature. Partial blisters were the common mode of film buckling for thermal oxide film thicknesses less than or equal to 147 nm for both normal and grazing laser incidence. In several cases, partial and non-partial blisters were produced with virtually identical laser conditions on the same sample, making it difficult to identify the mechanism responsible for partial blister formation. Similar partial blister features have been observed to result from ns pulsed laser ablation of Si with thin thermal oxide films (< 100 nm), where partial blisters were attributed to film buckling over a visco-elastic substrate [153]. Future work employing front-view pump-probe imaging techniques similar to those discussed in Chapter 6.1 may provide insight into the real-time events associated with partial blister formation.

At grazing laser incidence, a blister-like morphology was produced on the 1200 nm PECVD oxide film on silicon for laser fluences between that required for

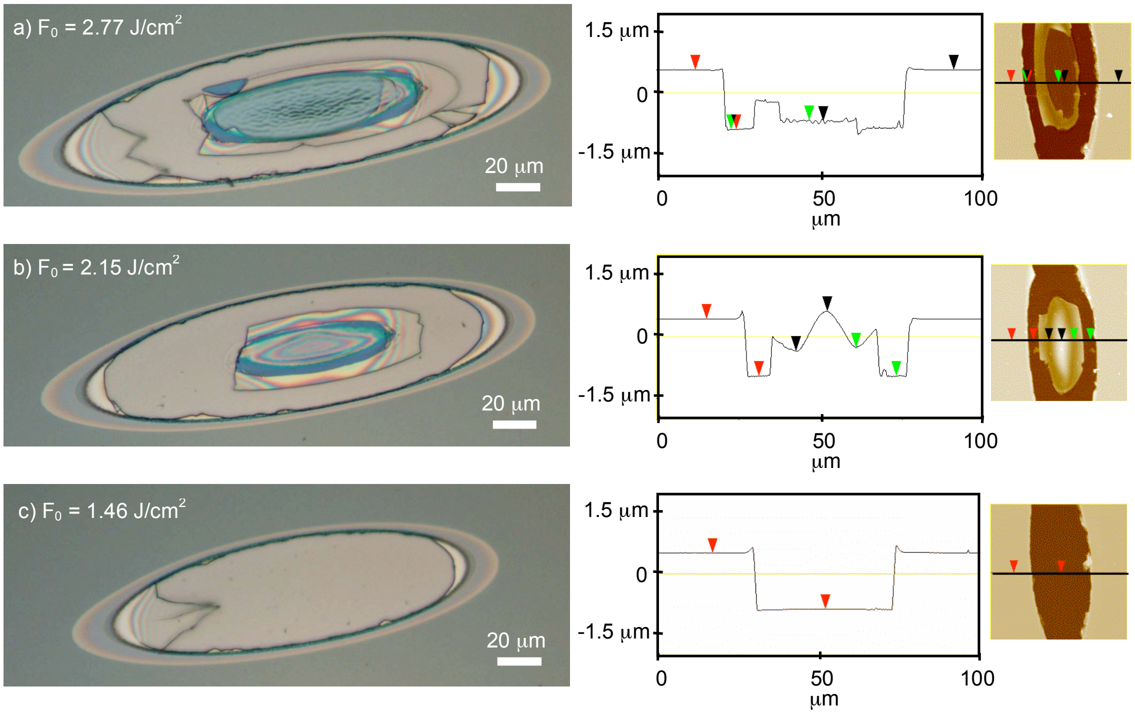

Figure 5.2.13 OM images and AFM cross sections of single pulse fs laser ablation morphology produced at grazing laser incidence (71.4° to sample normal) with s-polarized radiation at laser fluences of a) 2.77 J/cm^2 b) 2.15 J/cm^2 and c) 1.46 J/cm^2. A thin section of the thermal oxide film appears to remain in the center of the features in a) and b) that is absent once the fluence is lowered as in c).

laser induced film buckling and laser induced film removal ($F_0 \approx 0.6$ J/cm^2). The oxide film at the ends of these elliptical blister-like features was attached to the surrounding film, while along the side of feature the glass film was fractured from the surrounding film, producing what may best be described as a “blister bridge.” An example of the blister bridge is provided in Figure 5.2.12. Observation of such blister bridge features via AFM revealed that the “bridge” region of the blister possessed a dramatic height increase with respect to the ends of the blister, presumably due to aggressive relaxation of compressive stress once the delaminated oxide was locally fractured from the surrounding film [149]. It is thought that similar blister bridge features were not observed for samples with thinner oxide films because the thinner films may not have tolerated the high local strain thought to be present near the ends of the blister bridge (where it connects to the surrounding film). In many cases the 1200 nm PECVD was observed to fracture at this location providing evidence for the high strain (see Figure 5.2.12 b))

For higher laser fluence (exceeding ~2.15 J/cm^2 at grazing incidence), a final ablation morphology was observed for single fs pulse laser irradiation of samples with 1200 nm of PECVD and thermally grown oxide. In the center of the ablation crater, a region of film appears to have remained on the substrate. As shown in Figure 5.2.13, AFM indicates that the film remaining in the center of the ablation crater has a reduced thickness with respect to the surrounding, undamaged film. The mechanism responsible for the formation of this high fluence ablation morphology is not understood at this time. At higher laser fluences, the glass film may absorb sufficient energy from the incident laser pulse to melt, changing the properties of the interface between the film and the underlying substrate (the ablation threshold for fused silica is around 1.5 J/cm^2 [12]). The heat generated by ablation of the substrate may also result in sufficient melting of the oxide film prior to its explosive removal [61], such that the interface between the film and substrate becomes diffuse enhancing the adhesion of the oxide to the substrate. A greater understanding of the precise mechanism may be obtained in the future by pump-probe imaging experiments (as in Chapter 6.1) at the high pump laser fluences for which these ablation morphologies are produced.

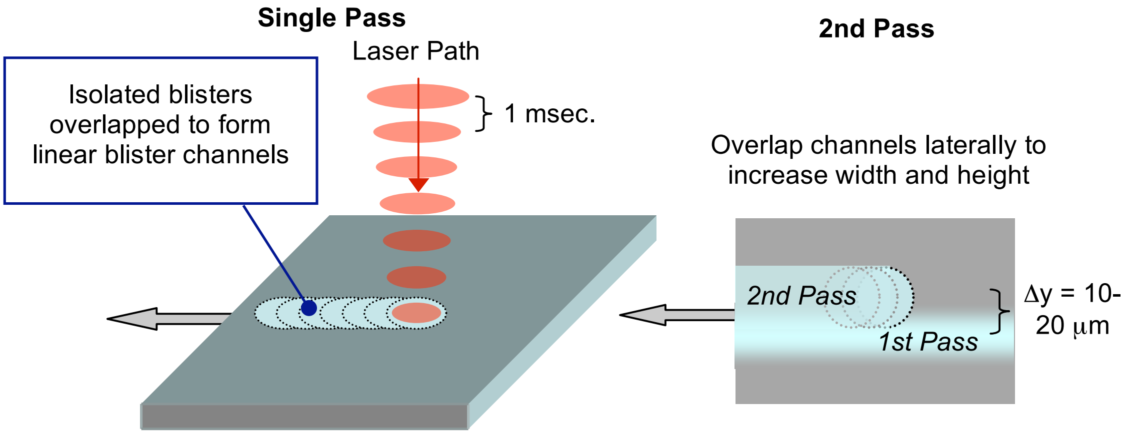

Figure 5.2.14 Schematic of linear blistering writing technique. For a single pass channel the sample is translation once through the focused laser beam at a speed of 5 – 10 mm/s. For a multiple pass channel, single pass channels were overlapped with a typical spacing of 10 – 20 μm.